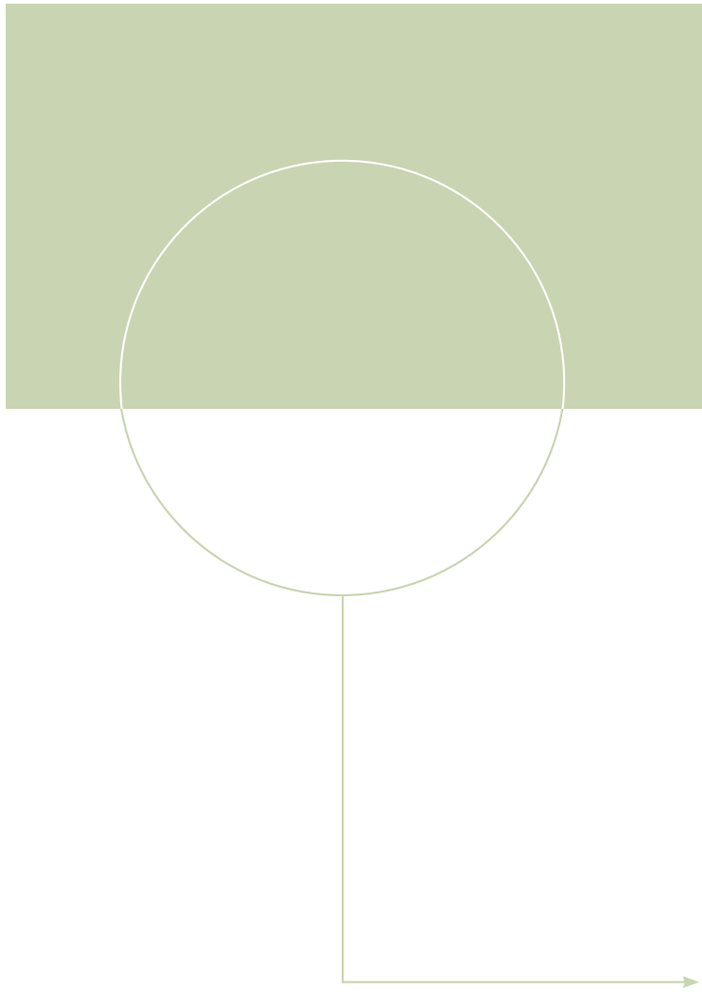

Master's thesis

2022

Sanam Nisar Mangi

NTNU
Norwegian University of Science and Technology
Faculty of Information Technology and Electrical Engineering
Department of Computer Science

Sanam Nisar Mangi

Measurement pipeline for accurate in-situ measurements of museum artwork using hyperspectral imaging

September 2022

NTNU
Norwegian University of Science and Technology

NTNU
Norwegian University of Science and Technology

NTNU
Norwegian University of
Science and Technology

Measurement pipeline for accurate in-situ measurements of museum artwork using hyperspectral imaging

Sanam Nisar Mangi

Computational Colour and Spectral Imaging (COSI)
Submission date: September 2022
Supervisor: Prof. Kevin Smet
Co-supervisor: Dr. Hilda Deborah

Norwegian University of Science and Technology
Department of Computer Science

Master in Computational Colour and Spectral Imaging (COSI)

Measurement pipeline for accurate in-situ measurements of museum artwork using hyperspectral imaging

Master Thesis Report

Presented by

Sanam Nisar Mangi

and defended at the

Norwegian University of Science and Technology

September 2022

Academic Supervisor(s): Dr. Hilda Deborah (NTNU)
Host Supervisor(s):
Prof. Kevin Smet, Prof. Frédéric Leloup & Ching-wei Lin (KU Leuven)
Jury Committee:

1. Asst. Prof. Miguel Angel Martínez, University of Granada, Spain
2. Assoc. Prof. Pichayada Katemake, Chulalongkorn University, Thailand

Submission of the thesis: 10th August 2022
Day of the oral defense: 2nd September 2022

Abstract

Conservators and researchers recognized the need to study and digitally document the colored artwork that makes up our cultural heritage. These digital documents are then utilised for various applications of preservations, such as, recording changes in appearance and conditions of paintings; pigment identification; investigating materials (such as varnish) present on the artworks; revealing hidden information in paintings; art conservation and art restoration. One of the important aspects of an artwork is its colour, as the artist uses colour to interact with the viewer. Hence, the digital documentation needs an accurate information of the coloured artwork. Hyperspectral imaging, a non-invasive imaging technique has been applied by several studies in a museum setup to acquire the spectral reflectance of a colored artwork. Hyperspectral imaging technique captures both spectral and spatial information of an object. Spectral reflectance is considered as an accurate reproduction. However, for the same object, the acquired information may vary depending on the method of data acquisition, systems used in the acquisition, and overall acquisition setup. However, to the best of our knowledge, there are no procedures or workflows established that assure data reproducibility. In this study, we applied a hyperspectral imaging technique in a museum settings in order to propose measurement pipeline to capture the spectral reflectance of whole surface of the artwork so that it ensures high quality data reproduction.

We have utilised the X-Rite Macbeth Color Checker as a test object to assess the accuracy of the line scanner hyperspectral camera Specim IQ under various experimental studies. To provide ground truth data for comparison, spot measurements are acquired with a JETI specbos 1211 spectroradiometer at each of the 24 patches of Macbeth ColourChecker. A series of experimental tests were conducted to investigate the impact of several aspects impacting the measurements, for-example, use of different light sources in a measurement setup, method of estimation of the illumination of the scene, the measurement geometry, etc. We provide the radiometric, photometric and colorimetric assessment of each of the experimental tests. Radiometric assessments are performed by means of the spectral reflectance curves and for the colorimetric assessment CIELAB and u'v' Chromaticity diagram (CIE 1976 UCS) units were computed for both CIE illuminant E and CIE D65 for the CIE 1931 2° standard observer.

Our experimental tests revealed that data is indeed influenced by the acquisition parameters. We also identified the colours which results in relatively high inaccuracy. The results of experimental tests are analysed thoroughly to propose the measurement pipeline to be used in museums. We also provide the suggestions and guidelines that can be useful for the researchers and conservators to carry out in-situ acquisitions in the museums.

Acknowledgment

This work has been carried out at the Light & Lighting laboratory, KU Leuven Technologiecampus, Gent, Belgium. I would like to express my gratitude to many people for their consistent support and guidance throughout this work.

I'd like to start by thanking my supervisors at my host institution, Prof. Kevin Smet, for his continued guidance and detailed feedback throughout the process, and Prof. Frédéric Leloup for generously taking the time out to participate in my research and providing his help and guidance throughout the project. Many thanks to Ching-wei Lin, a PhD student at the Light & Lighting laboratory who was assigned to provide me with direct supervision, for all of his teaching, encouragement, and endless support.

I am extremely thankful to my academic supervisor, Dr. Hilda Deborah, at NTNU, Norway, for her valuable input and guidance throughout the project, as well as for her continuous encouragement and inspiration as I sped along the way.

My friends and colleagues in the Light & Lighting laboratory deserve a special thanks for always willing to help with this project by offering advice, direction, training, and suggestions. Lastly, I want to thank my family, COSI colleagues, and all of my friends in Gent for being there for me physically and/or emotionally and for experiencing both joyful and sad moments with me.

Acronyms

AM	application mode
ASM	automatic screening mode
CCT	correlated colour temperature
CFL	Compact fluoresecent light
CH	cultural heritage
CIE	commission internationale de l'Éclairage
COSCH	color and space in cultural heritage
CRI	colour rendering index
DRM	default recording mode
EM	electromagnetic spectrum
ER	electromagnetic radiation
FTIS	fourier transform imaging spectrometry
GFC	goodness of fit coefficient
HDR	high dynamic range
HID	high intensity discharge
HSI	hyperspectral imaging
IFAC-CNR	institute of applied physics of the national research council
IP-UEF	institute of photonics - university of eastern finland
IR	infrared
ISCC	Inter-Society Color Council
LDR	low dynamic range
LED	light emitting diode
MacbethCC	X-rite macbeth colorchecker® classic
MH	metal halide
NBS	National Bureau of Standards

NIR	near infrared spectrum
RGB	red green blue
RMSE	root mean square Error
RRT	round robin test
SPD	spectral power distribution
SWIR	shortwave infrared
UV	ultra violet
VIS	visible spectrum
VNIR	visible near infrared

Contents

1 Introduction

In order to investigate materials, optically characterise them or identify their optical properties, spectroscopy may be used. Spectroscopy is the study of electromagnetic radiation (ER) and material interaction. When ER strikes the surface of the material, it reflects, absorbs or transmits the energy depending on its spectral properties. The reflectance or transmittance of a material with respect to wavelength is called spectral signature [4]. Spectroscopy uses spectral signatures to identify the objects because materials have unique spectral signatures. The range of different frequencies (ranging from 1 hetrz to 10^{25} hertz) with respect to wavelength is represented by electromagnetic spectrum (EM) [63]. The range of frequency is divided into separate bands. The electromagnetic radiations within each frequency band are given specific names. For example, ER at the low frequencies are called radio waves, and at the high frequencies are called gamma rays [63]. Different regions of ER are shown in Figure 1.1. The optical characteristics of ER are different across frequency bands. They interact differently with different materials, resulting in each material's unique spectral signature. That is why the spectral signature is also called the fingerprint of the material. Spectral signature is used to identify a material specifically. For example, the green grass reflects significantly more light in the near infrared spectrum (NIR) than it does in the visible spectrum (VIS). On the other hand, water absorbs more infrared (IR) and has a high reflectance in the VIS. Base ground (i.e. soil) has high reflection in the mid of the IR, and it reflects more green and blue light [35]. Hence green grass can be differentiated from the soil and water based on each of their unique interaction with light.

The EM is represented by a graph on a scale of intensity versus wavelength. The study of measuring ER in any region of the EM is known as radiometry. This measurement can be performed using an instrument called a spectrometer which splits the incoming light into an EM [8]. Reflection is the process by which a radiant flux incident on a surface of material leaves that surface without changing the wavelength [56]. Spectral reflectance is a reflection as a function of wavelength. Measuring spectral reflectance is the most typical approach to hyperspectral imaging (HSI) [37].

1.1 Hyperspectral Imaging

HSI is a spectroscopy based non-invasive analytical technique [15]. It can capture multiple bands (ranging from 10 to 100, 1000, and so on) of the EM at different wavelengths for the same spatial area. While a conventional RGB camera is limited to capturing three bands, i.e., red, green, and blue of the EM, it is also unable to identify tiny details outside these bands. Figure 1.1 shows EM.

In HSI, every pixel has multiple consecutive bands depending on the sensor used. Many sensors can measure the visible region of the EM (400–700 nm, VIS) as well as the near-infrared wavelength (700–1000 nm), they are called visible near infrared (VNIR) sensors. For some applications, the shortwave infrared (SWIR) (1000–2500 nm) part of the EM is also significant. However, a single sensor cannot capture all spectral regions [10]. HSI can provide reflectance characteristics of objects on various range of EM.

The acquired data of the reflected light of the target is a three-dimensional data cube with two spatial dimensions (of x rows and y columns) and one spectral dimension (of *lambda* wavelengths) [21]. A hyperspectral image, denoted by $I(x, y, lambda)$, can be seen as a single spatial image $I(x, y)$ at each individual wavelength *lambda* or as a spectrum $I(lambda)$ at each individual pixel (x, y) [21] (see Figure 1.2). An HSI system is capable of recording spectral characteristics and spatial information at the same time [76]. Spectral characteristics as well as spatial information can be simultaneously recorded with an HSI system.

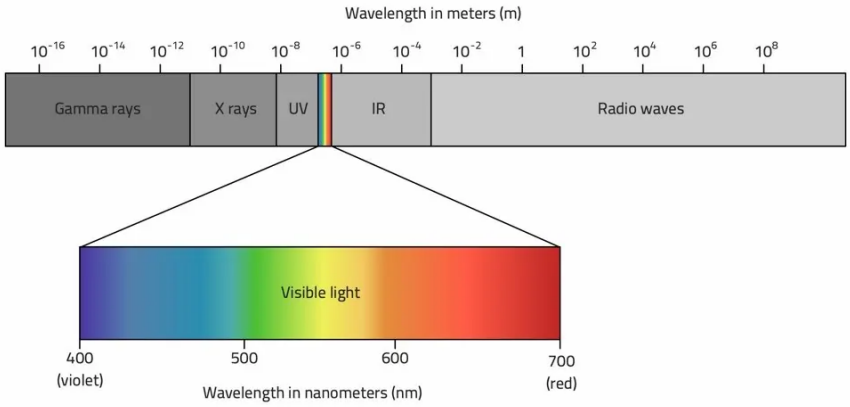

Figure 1.1: *Electromagnetic spectrum divided into range of frequencies of ER. The ER at the low frequencies are radio waves, microwaves, infrared, visible light, ultraviolet, X-rays, while the gamma rays lies at the highest frequency [68].*

1.1.1 Radiometric, Photometric, Colorimetric Quantities

HSI is concerned with spectral radiometric quantities, i.e., the measurement of ER in certain regions of the electromagnetic spectrum. Photometry and colorimetry, on the contrary, focus on the human visual response to the intensity of light [46]. Radiometry investigates the overall energy content of radiation, whereas photometry and colorimetry just investigate the radiation that humans can see [46]. The most common quantity in radiometry is 'radiant flux' (i.e. power), it is measured in watt (W) [6]. Photometric quantity related to the radiant flux is called the 'luminous flux' and it is measured in lumen (lm) [6]. The summary of radiometric and photometric quantities which are used in the research is given in Table 1.1. Colorimetry, on the other hand, is concerned with physically describing and quantifying human colour perception based on psychophysical experiments [26].

Table 1.1: *Summary of radiometric and photometric quantities [70]*

Quantity	Unit	Description
Radiant Power	Watt (W)	Also known as Radiant flux, is the amount of radiant energy that is emitted, reflected, transmitted, or received per unit time.
Radiance	$W.m^{-2}.sr^{-1}$	Radiant flux that a specific surface emits, reflects, transmits, or receives per unit solid angle per unit projected area.
Spectral Radiance	$\frac{W.m^{-2}.sr^{-1}}{nm}$	Radiance as a function of wavelength (nm).
Irradiance	$W.m^{-2}$	Radiant flux received by a surface per unit area.
Reflectance	-	Reflection is the process by which a radiant flux incident on a surface of material leaves that surface without changing wavelength.
Spectral reflectance	-	Reflectance as a function of wavelength (nm)
Luminous flux	lumen	Perceived power of the light
Illuminance	lux	Luminous flux incident on a surface per unit area

1.1.2 HSI Systems

HSI can be classified by the method of acquiring the data cube as : (a) Pushbroom (b) Staring (c) Fourier transform Imaging Spectrometry (d) Whisk-broom (e) Snapshot Imaging [53]. These are briefly overviewed as follows:

Pushbroom

The pushbroom, also known as the line-scanning method, records the spectra of pixels on a single spatial line at each point in time. As a result, for each spatial line, a two-dimensional array of measurements is formed, displaying spatial information in one axis and wavelength information along the other axis [7]. A pushbroom scanner can capture more light since it remains in the same location for a longer period of time, providing the detector a longer exposure and higher spectral resolution.

Staring

The staring (also known as the band sequential method) is a data acquisition method that simultaneously acquire a 2-D grayscale single band image $I(x, y)$ with full spatial information [48]. The filter wheel is used in front of the camera to take several images of the same scene, which are then combined to create a dataset at various wavelengths.The system's technical specifications and imaging technique are provided in [48, 23].

Fourier transform imaging spectrometry

fourier transform imaging spectrometry (FTIS) uses a sagnac interferometer as an internal interferometer to capture the scene onto the camera sensor [53]. This type of imaging technology is uncommon, especially in the VNIR range [53]. The system's and imaging procedure's technical details are described in [13, 52].

Whisk-broom

Whisk-broom imaging systems use a linear array of sensors to acquire a single column of the data-cube simultaneously, it scans over two spatial dimentions of the data cube [7]. Whisk-broom imaging systems have better spectrum homogeneity since all pixels are recorded using the same detector linear array, which allows for a bigger detector pixel size in the optical design [16]. The whiskbroom technique is most commonly used in remote sensing. It is based on time-domain spectroscopy of a single pixel [7].

Snap-shot Imaging

Snapshot imaging spectrometers use a single integration time to acquire the whole three-dimensional (3D) data cube without scanning. It captures spectral images in real time (many frames per second), however, these systems offer lower spatial and spectral resolutions [28]. Snapshot's comprehensive description may be found in [28].

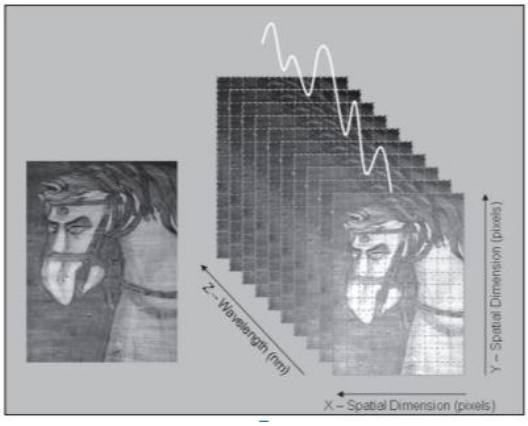

Figure 1.2: *Schematic representation of a spectral image cube displaying both spectral and spatial information [30].*

The ability to obtain full spectral resolution images of scenes is extremely useful in imaging, graphics, and vision research because it allows researchers to investigate the benefits of various colour-representations of scenes as well as to quantify the errors introduced in the traditional (red green blue (RGB)) imaging process. With the introduction of increasingly compact hyperspectral cameras and real time hyperspectral imaging, a range of new applications emerges in the fields of agriculture [27, 75], mineralogy [38], medicine [42], forensics [20], and remote sensing [19, 18], art and heritage [20, 30] etc.

1.2 Applications of HSI

Following are a few examples of HSI:

Agriculture

Light-weight hyperspectral cameras are often installed on drones and can detect the slightest differences in crops, plants or solids and can altery farmers and researchers about diseases, droughts and other issues related to agriculture [27, 75].

Mineralogy

HSI has been used in the field of mineralogy to create detailed mineralogical maps of drill cores, and it can assist in the identification and evaluation of minerals [38].

Medicine

Hyperspectral video cameras can assist surgeons by offering them information that's invisible to the naked eye. HSI imaging can be used to inspect living tissues, e.g. in diagnostic instruments or during surgery [42].

Forensics

The ability of hyperspectral imaging to detect spectral fingerprints of materials such as blood or gunpowder. It detects these markers at a crime scene without the use of chemicals that might tamper with the evidence [20].

Remote sensing

An increasing number of observational satellites are being launched into space with a hyperspectral sensor aboard. It allows them to distinguish between the spectral signatures of soil, vegetation, minerals, and other substances [19, 18].

Art and cultural heritage (CH)

Historical artefacts have a lot of stories to tell. When it comes to investigating cultural artefacts, the use of invasive techniques is avoided as they involve samples of investigated objects. HSI, being a non-invasive analysis technique, has been utilised since 1990s for applications, related to revealing hidden information in paintings, to art conservation, to art restoration, etc. without damaging the artefact [20, 30].

According to a number of recent conservation and archaeology reviews, HSI is becoming more popular in the fields of art conservation, art history, and archaeology etc [20, 30]. Non-invasive technologies such as infrared reflectography, ultra violet (UV) reflectance, and UV induced visible fluorescence, which are commonly used for the study and conservation of artefacts, have been revolutionised by HSI [30]. Other conventional methodologies, e.g., spot reflectance spectroscopy [45] have found to be effective for non-invasive pigment identification in the VIS and NIR regions [16] of EM. It has been used effectively to differentiate and identify artists' materials on polychrome surfaces [7, 17]. Traditional reflectance spectroscopy as

well as other non-contact techniques, e.g., fluorescence and Raman spectroscopy [29], can only be used for spot testing. Spot testing is ineffective for artefacts with substantial spatial heterogeneity. "Hyperspectral cameras combine the spectral resolution of a spectrophotometer with the spatial resolution of a camera and have become increasingly popular as an analytical tool" [22].

1.3 HSI of pictorial artworks

HSI has been applied qualitatively in pictorial artwork for band to band comparison to detect natural degradation of material [45], to detect regions with different material composition [59] and quantitatively for improved precision in colour measurement [29]. Recently, some applications linked to pictorial artwork, such as, pigment mapping [82], material identification [59], conservation and restoration of CH [53], are appearing as promising new application areas for the use of spectral imaging systems.

The most critical factor when studying the pictorial artwork is accurate acquisition of spectral information and high spatial resolution. Accuracy and high quality are very important characteristics of the data, especially when working with coloured materials. Coloured materials are prone to change, resulting in changes in the visual appearance of the artwork and, as a result, the objects are interpreted differently than the creator intended [74]. This means that acquired data should have accurate colour reproduction that takes into the colour appearance attributes of the human visual system into consideration in any illumination.

The only way to precisely quantify colour in paintings was to use a spectrophotometer to obtain spot readings of spectra and capture a rough region of the sample [44]. Spectral imaging technology eliminates the limits of conventional area-based point-measurement devices such as spectrophotometers, by allowing pixel by pixel or region based study [45]. Although spectral cameras are considered to have lower colour accuracy than spectrophotometry, they are capable to measure the entire surface, making them an excellent choice for analysing colour distribution on natural objects [22], hence they have been utilised as an in-situ tool for examining and digitising coloured artworks.

When it comes to measuring historical paintings accurately with HSI, it needs much more than just taking images with conventional RGB camera. The aquired image needs to be an accurate reproduction of the painting. Studies related to HSI device assessments suggest that "the accuracy and reliability of the acquired data depends on the device used" (e.g. sensitivity of the detector etc) [43, 74]. However it is not just restricted by the technical specifications and specific acquisition parameter settings of the HSI device but also by characteristics of the illumination (e.g. spectral power distribution) and viewing geometry etc [30]. In this research

study, we focus on identifying the way to measure the spectral reflectance accurately on the paintings, and we investigate the factors that can affect the reliability of the acquired data.

Research question and motivation

The research question addressed in the current study is: what is the most accurate way to measure spectral reflectance of paintings in a museum setting using a portable hyperspectral camera and to determine how different methods of measurement (i.e. acquisition setup, use of different element involve in acquisition setup) affect the accuracy of the image acquired. The principal motivation behind this research is the lack of a standard for measuring the spectral reflectance of the painting, although it has been identified by previous studies that the accuracy of the acquired data is influenced by the acquisition methodologies. There are no established guidelines that must be followed to guarantee that the acquired data is accurate and reliable, in the context of artwork or in museums.
In this research work, we present a measurement pipeline which can be used for in-situ measurement conditions for measuring the spectral reflectance of the artwork. The research is divided into the following:

- We investigate several factors related to the measurement setup that influence the data accuracy.
- We propose a standardised workflow to be followed for all hyperspectral reflectance acquisitions in a museum.

The benefit of the study is that the researchers will follow a standardised methodology for data acquisition, which assures data reproducibility. The long-term goal of this research is to be used in a real-world museum setup to acquire spectral reflectance images from the CH artworks and form a publicly available database. To the best of our knowledge, there are no publicly available HSI databases to be used for research purposes. The following research applications may benefit from the database:

- Study of pigment identification techniques.
- Art degradation or ageing of pigments used in those acquired paintings.
- Investigating material present of the surface of those paintings e.g. varnishes etc.
- Revealing hidden information from the acquired paintings.

- Conservation and restoration of those paintings.

The study is structured in such a way that the next section of chapter 1 discusses the in-situ measurement conditions and concerns that can arise during the acquisitions in an uncontrolled museum environment, a summary of the relevant work being done to accurately archive the artworks in a museum environment is given in chapter 2. The test target and devices used in the study are described in chapter 3, the experimental methodology is covered in chapter 4, and the experimental tests, results and discussion are considered in chapter 5, which is followed by a conclusion and direction for future research.

1.4 Hyperspectral imaging for accurate in-situ measurements in museum settings

Acquiring useful spectral reflectance image data can be a very difficult task in uncontrolled environments such as museums [44]. Collections in museums should only be exposed to certain environmental conditions, such as temperature, light, and humidity. Since unsuitable environmental conditions in museums can damage artworks (e.g. the rate of deterioration of materials increases as the temperature increases), this therefore limits the measurement setups to be used for acquisitions. The following are some of the challenges and limitations that can arise when taking measurements in a museum.

- Uncontrolled illumination

One of the challenges is uncontrolled or non-homogeneous illumination conditions [44]. Artworks in museums may be illuminated in a non-homogeneous manner when outside daylight interferes with the measurement conditions through the ceilings, resulting in highlights for paintings with glossy surfaces, and the surrounding frames around the paintings can cast shadows.

- Lighting conditions

There are some limitations when choosing the lighting conditions for the acquisitions. Selecting the most appropriate lighting conditions is important in ensuring a successful imaging process. However, lighting must satisfy a number of standards when used to illuminate artwork in a museum [24]. Since light is well-known as the damaging cause of museum artefacts, the requirement of standard illuminance

levels and considerations of limiting or excluding UV radiation must be followed [24].

According to the recommendations of The Museum Environment [71], "UV should ideally be eliminated entirely or it should be limited to 75 microwatts per lumen. And visible light should be limited between 50 and 80 lux for light sensitive objects such as water colours paintings, papers, plastics etc. Visible light of 200 to 250 lux is permitted for less light sensitive objects such as oil paintings, wood, and so on" [71].

- Arrangement and orientations

Museum collections are delicate and may be extremely susceptible to damage, making them difficult to capture. Nevertheless, it presents its own challenges. Paintings may be arranged differently from each other; some might be tilted and installed in a certain location, arrangement, or orientation. This can be challenging for estimating spectral reflectance accurately. The intensity of the reflected light from the painting may differ significantly depending on how the paintings are positioned [44].

2 Literature Review

Various spectral image acquisition techniques have been used to research and digitally document CH artworks in the past [43]. CH artworks require accurate data acquisition for them to be documented, and conserved [25], therefore various studies have investigated some of the important aspects of acquiring accurate HSI data.

The color and space in cultural heritage (COSCH) working group defines best practices and standards for digitising and documentation of cultural heritage objects. In one of their recent studies, [43], multiple institutions participated to conduct round robin test (RRT) on one test object (i.e., "a polychrome Russian icon from the late nineteenth-century with stylised sacred images of Christ, the Virgin Mary, and saints"). The objective of their study was to qualitatively or quantitatively evaluate the performance of ten different spectral imaging systems. They performed the study to determine the impact of each device, setup, and workflow on the results obtained. Each participating institution followed their own setup and workflow, which was also device dependent. The test object included a wide range of colours, having matte-finish flat surfaces with medium glossy painted areas. These characteristics made it an appropriate test target for evaluating colorimetric and radiometric accuracy. The spectral data was acquired from ten spectral systems. The data was assessed qualitatively in psychophysical experiments, in which groups of observers were asked to evaluate the quality of ten RGB reconstructed images of the test object based on the parameters such as colour fidelity, sharpness, contrast, visibility of the fine spatial details, geometric distortions, and uniform illumination. The results of the experiment revealed that different imaging systems used by different institutions produced a wide range of visual differences. In order to evaluate the spectral imaging systems quantitatively, spectral analysis was performed.

The reflectance spectrum is reconstructed at selected points from the acquired HSI data, which was then compared with the ground truth data. The ground truth data is a reference data that was acquired with spot measurements taken at six different positions with the X-rite i1Pro spectrophotometer. The difference was calculated between the corresponding points in terms of both RMSE and colour

difference ΔE*ab. The quantitative assessment was reported to have less than 0.02 RMSE errors, and the colour difference (i.e. ΔE*ab) errors were less than 5 units. The study reported that the larger error values occurred for the red, rob roy, and gold colour sample points. The level of noise in the spectra, especially at the extremes of the wavelength range (i.e., 400 nm and 700 nm), was noticed among the HSI dataset acquired by different devices. In this study, each participating institution was asked to comply to its own processes which in turn revealed a range of traits of the image quality. The need for standard procedure was emphasised in the study to document CH artefacts in order to have accurate reproduction of the data.
There are various projects that have contributed to the development of spectral imaging systems for the CH sector and have succeeded in designing hardware and software solutions for spectral image acquisition with good accuracy. The VASARI scanner and the MARC are two imaging systems of those projects[60], developed by the National Gallery of London to produce images of paintings that would have high resolution and high colour accuracy. Each of these two systems is capable of recording images with good colour accuracy. Those images are then used for several CH applications (e.g. study the deterioration and degradation of colour, reconstruction of the images) which require comparisons between the current and future state of the artwork.

The VASARI scanner achieves colour measurement by capturing the image seven times while illuminating that section of the artwork with light of different wavelengths. The different wavelength of light is created by passing white light through one of seven band-pass filters across the visible spectrum. Those seven acquired images are then corrected for radiometric variation, then are combined to create a high-resolution mosaic image and to give accurate measurements of the entire painting. The colour accuracy for the VASARI scanner is ΔE*ab = 1.1 units. Although the Vasari scanner generates high-resolution images with good colour accuracy, it has several flaws. Firstly, the physical dimensions of the scanner limit the size of the painting to 1.0 by 1.0 m. Secondly, the scanner is not portable at all; paintings must be taken to the laboratory, which is not always convenient, because the paintings are too delicate to be removed from museums anytime an acquisition is required. As a result, the VASARI system cannot be used for in-situ measurements.

The Marc scanner project, on the other hand, is a semi-portable imaging device, capable of making a high-resolution image (approximately 20,000 x 20,000 px^2) in a single exposure under photographic lights. The entire image acquisition procedure from a camera is controlled by computer software. Setting up even illumination, avoiding glare, and framing the paintings in the field of view are the trickiest steps. The colour accuracy achieved by the MARC scanner is roughly ΔE*ab = 3 to 3.5

units, which is less than the VASARI scanner but far better than the theoretical best colour photographic system.

Another study [44] proposed a multi-focus HDR VNIR/NIR hyperspectral imaging workflow to capture and process HDR HSI data using hyperspectral visible and near-infrared line scanner cameras (i.e., Pikaal) for in-situ measurements. This research considers the impact of uncontrolled illumination, such as HDR conditions in the scene and the impact of chromatic aberration on image quality. Multiple shots with varied focus positions and exposure times were used to solve both the high dynamic range and the focusing difficulties caused by chromatic aberrations. When compared to the ground truth data, which was acquired from 16 different areas of the painting spectral reflectances of the exact same areas from HSI data, the spectral metrics (i.e. RMSE and goodness of fit coefficient (GFC)) results showed that errors in the HDR spectral cube are 36.96 percent and 66.98 percent better than the LDR spectral data. There was no additional analysis provided.

Until now, the digital archives for art works have been based on the object's surface reflectance information. Tominaga et al.[72] suggested that relying solely on surface-spectral reflectance limits the image acquisitions of artwork to the fixed geometric conditions of illumination and viewing at the time the original image was acquired. Instead, for the digital archives of art works, it is critical to record both (3D) shape and spectral reflectance information, and the artworks should be captured and rendered as three-dimensional (3D) objects. The study suggested a precise estimation approach for surface spectral reflectance estimation, employing a set of reflectance observed at different illumination directions and the generated shape of the object surface at the estimation stage, and then used a 3D light reflection model (BRDF model) to create computer graphics representations during the rendering step. The derived object shape and spectral reflectance were used to create object images under various lighting and viewing conditions. The method's feasibility was determined only through a visual experiment involving a qualitative assessment of the acquired images.

Another study [45] proposed a HSI approach for the colorimetric analysis of real artworks under arbitrary lighting conditions. This is the first study to use commission internationale de l'Éclairage (CIE) proposed light emitting diode (LED) illuminants in the context of art and heritage science and compared them to the three primary CIE illuminants: A, D50, and D65. Images of the test subject (i.e. "the Nasrid period (12th–15th centuries) Moorish epigraphic frieze plasterwork in the museum of the Alhambra (Granada, Spain)") are captured with the hyperspectral image scanner Resonon Pikal. The comparison is carried out by computing

the corresponding colours under D65. The CIEDE2000 colour differences were measured pixel by pixel to see how much the sample's final colour changed when employing the nine CIE LED illuminants versus the conventional CIE illuminants (A, D50, and D65). It was discovered that the best CIE LED illuminant to match standard illuminant A was V1, as it had the smallest average colour difference in CIEDE2000 (1.23 CIEDE2000 units). On the other hand, when it comes to matching D50 or D65, V2 matches well in both cases (1.06 and 1.57 CIEDE2000 units, respectively). The study also identified discrepancies in the most suitable CIE LED illuminant to use based on the colour of the sample, e.g. comparing the illuminant D65 with V2, which is the CIE LED with the smallest average CIEDE2000 colour difference for the entire sample (1.57 CIEDE2000 units), and it only produced the best results for black and plaster for individual colours (1.92 and 1.47 CIEDE2000 units, respectively). However, B3 performed best for blue, green, and white (with 0.94, 1.45, and 1.28 CIEDE2000 units, respectively), and BH1 was the best choice for yellow (with 1.52 CIEDE2000 units). It also indicated that the areas with the greatest colour differences (CIEDE2000 of approximately 10 units) correspond to the sample's yellow areas, i.e., the yellow areas are the ones with the strongest colour difference. This study of colour appearance under various illuminants can help art and heritage experts decide which lighting to use in museums or which conservation or restoration procedures will best retain the original piece's colour appearance under any illuminant.

The COSCH working group carried out RRT [74] on an "X-Rite ColorChecker classic chart" (i.e., a chart constituted of 24 standard coloured patches, used as a colour reference chart in studies [82, 53]) using the two push-broom hyperspectral systems developed by two different groups institute of applied physics of the national research council (IFAC-CNR) and institute of photonics - university of eastern finland (IP-UEF) . The research examined the accuracy of two systems' color reproduction processes to assess the impact of each instrument on the acquired results in order to ensure the data's usability, accuracy, and comparability. Ten colour patches were selected, and the reflectance spectrum was extracted from the centre squares of 35 mm to represent the average of each colour patch. Data is acquired from both systems. Colorimetric CIELAB values were calculated for a standard illuminant (D65) and observer (10°) and were also compared. Results indicated that there is a spectral similarity between the data acquired from both the systems except for the lower and higher wavelengths that show differences in intensity. When comparing the colorimetric values of the two hyperspectral systems, the L* and a* values are similar, but the b* coordinate shows considerable differences for the magenta, blue, and red (ΔE 3.7, 3.8, and 5.1, respectively) colours, which are at both ends of the visible spectrum and reported to have

varying reflectance spectra. On the other hand, green and yellow showed a higher similarity between the values obtained with the different systems, with only 2-3 unit differences in the L*, a*, and b* coordinates (ΔE 3.3 and ΔE 2.5, respectively).

3 Materials & Devices

This chapter provides a general overview of the devices and materials employed in the research. The X-rite macbeth colorchecker® classic (MacbethCC) [1], which is used as a test object, is described in Section 3.1. The test instrument, the Specim IQ hyperspectral camera [34], is described in Section 3.2, along with its technical characteristics and basic methodology. Reference measurements are taken using two devices, the JETI specbos (spectroradiometer) [65] and the HunterLab UltraScan® PRO (spectrophotometer) [55], to assess the accuracy of Specim IQ. Sections 3.3 and 3.4, respectively, provide their general overview and technical specifications. The programming language Python [41] and the LuxPY toolbox [64], which are used in this research for computations, are briefly addressed in 3.6.

3.1 Test Object: X-Rite Macbeth ColorChecker®

The test object for this research is the MacbethCC [1] chart. The MacbethCC is a matte chart with dimensions of 279.4 mm by 215.9 mm [3]. It includes twenty-four coloured square patches, each of a 40-mm size, arranged on a 4 by 6-inch grid. They are attached to a rigid support, and each patch and the entire array are surrounded by a thin black border [3]. It represents four different categories of colour, i.e., natural colours, miscellaneous colours, additive and subtractive (primary & secondary) colours, and different shades of grey [3] (see Figure 3.1). Table 3.1 shows the index, description and ISCC/NBS names of the colour patches. The colour patches in the following study are referred to as index-descriptions (e.g. 1-Dark Skin).

Colour targets like MacbethCC are captured by colour input devices, e.g., cameras, and the output (i.e., resulting images) is compared to the MacbethCC, or to reference measurements, to examine how closely image acquisition reproduction systems and processes resemble human visual systems [3, 51]. MacbethCC has been widely used in research studies to evaluate the accuracy of reproduction systems

[74, 11].The MacbethCC is used as a colour reference in this study to ensure that the data acquired is accurate and shows spectral reflectance of the test object. Because it has a number of different colours, it is a convenient target to evaluate the accuracy of reproduction of various pigments.

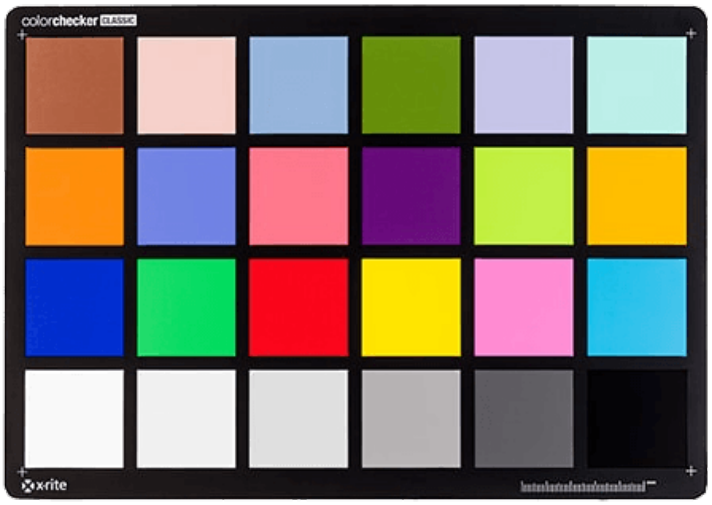

Figure 3.1: *X-Rite Macbeth ColorChecker® [1]*

3.2 Hyperspectral camera: Specim IQ

The Specim IQ [34] (see Figure 3.2) is a line-scan (i.e., push-broom) hyperspectral imager-based portable hyperspectral camera. It is manufactured by Specim in Oulu, Finland. It is a compact portable device, with an additional RGB camera, designed as a stand-alone HSI camera to be used in a variety of indoor and outdoor scenarios [10]. Furthermore, this system functions similarly to a reflex camera, with a touch screen interactive display on the back of the camera that allows full control of the data acquisition and processing activities. The integrated colour camera facilitates the use of the spectral camera by allowing visualisation of the scene and manual focus adjustment. Because the acquisition procedure might take anything from a few seconds to many minutes (depending on the integration time), neither the target nor the camera may move during the data recording. Hence, the camera must be fixed on a tripod. A built-in scanner in the Specim IQ camera rotates the spectral camera within the system during data recording. This implies that Specim IQ works in the same way as digital cameras: point at the target, adjust

Table 3.1: *Summary of the colours in X-Rite Macbeth ColorChecker® [3]*

Index	Description	ISCC/NBS Name
Row 1: Natural colours		
1	Dark skin	Moderate brown
2	Light skin	Light reddish brown
3	Blue sky	Moderate blue
4	Foliage	Moderate olive green
5	Blue flower	Light violet
6	Bluish green	Light bluish green
Row 2: Miscellaneous colours		
7	Orange	Strong orange
8	Purplish blue	Strong purplish blue
9	Moderate red	Moderate red
10	Purple	Deep purple
11	Yellow green	Strong yellowish green
12	Orange yellow	Strong orange yellow
Row 3: Primary and secondary colours		
13	Blue	Vivid purplish blue
14	Green	Strong yellowish green
15	Red	Strong red
16	Yellow	Vivid yellow
17	Magenta	Strong reddish purple
18	Cyan	Strong greenish blue
Row 4: Grey Scale colours		
19	White	White
20	Neutral 8	Light grey
21	Neutral 6.5	Light medium grey
22	Neutral 5	Medium grey
23	Neutral 3.5	Dark grey
24	Black	Black

the parameters, and shoot. The camera is provided with a software "Specim IQ Studio" (Specim Ltd., Oulu, Finland) to analyse the images [10].

In this study, all the hyperspectral images have been captured using SpecimIQ. Due to the portability of the device, it is the most suitable choice for the in-situ measurements, as it can be placed and moved from one place to another easily for acquisitions of different paintings.

Figure 3.2: *SpecimIQ at Light&LightingLab, KU Leuven.*

3.2.1 Technical specification of the SpecimIQ camera

The Specim IQ hyperspectral camera is a handheld device that combines hyperspectral data capture, data processing, and visualisation of the results into a single instrument. The wavelength range of Specim IQ is 400-1000 nm. The recorded data has a spatial resolution of 512x512 pixels. The resulting hyperspectral data is three-dimensional and contains both spectral and spatial information for the user. In addition to the hyperspectral data, Specim IQ also saves a 5 megapixel colour image of resolution 645x645 pixels of the target. Technical specifications of SpecimIQ are provided in Table 3.2.

3.2.2 General workflow of SpecimIQ

Specim IQ is operated uisng a touch screen display and graphical user interface leads the user through the full imaging pipeline [10]. The imaging pipeline is divided into five steps as shown in Figure 3.3.

Table 3.2: *Technical specification of SpecimIQ [34]*

Feature	Value
Spectral camera	VNIR 400-1000 nm (CMOS)
Spectral bands	204
Spectral resolution FWHM	7 nm
Spatial resolution	512x512 px
Pixel size	17.58 µm x 17.58 µm
Operational time	Appx. 100 measurements with one SD card and battery
Viewfinder camera	5 Mpix
F/number	1.7
Size	207 x 91 x 74 mm (depth with lens 125,5 mm)
Weight	1.3 kg
Working distance	150 mm–∞
Peak SNR	>400:1
FOV	31° × 31°
FOV at 1 m distance	0.55 m × 0.55 m
Data output	12 bit
Operating voltage	3.7 V
Battery	5200 mAh Li-Ion (Type 26650)

3.2.2.1 Positioning the device and illuminating the target

The viewfinder camera, which is a RGB camera with the same viewing direction but a small vertical offset, is used to position the HSI camera at the target [10]. A suitable light source with a continuous spectrum across the wavelength range is necessary for any hyperspectral measurement, which can be a natural light source, e.g. sunlight for outdoor measurement conditions, as well as artificial light sources, e.g. halogen or LED light sources for indoor measurement conditions.

3.2.2.2 Selecting the white reference

The white reference is a standard white sheet that is highly reflective (95-99%) across the entire wavelength range. It is used in spectral measurements to capture characteristics of the illumination in a scene. Specim IQ provides three different methods to measure that, i.e., custom white reference, simultaneous white reference, and predefined white reference [66].

- **Custom white reference:** Before taking the actual measurement, the measurement of white reference might be recorded, which is referred to as a custom white reference.

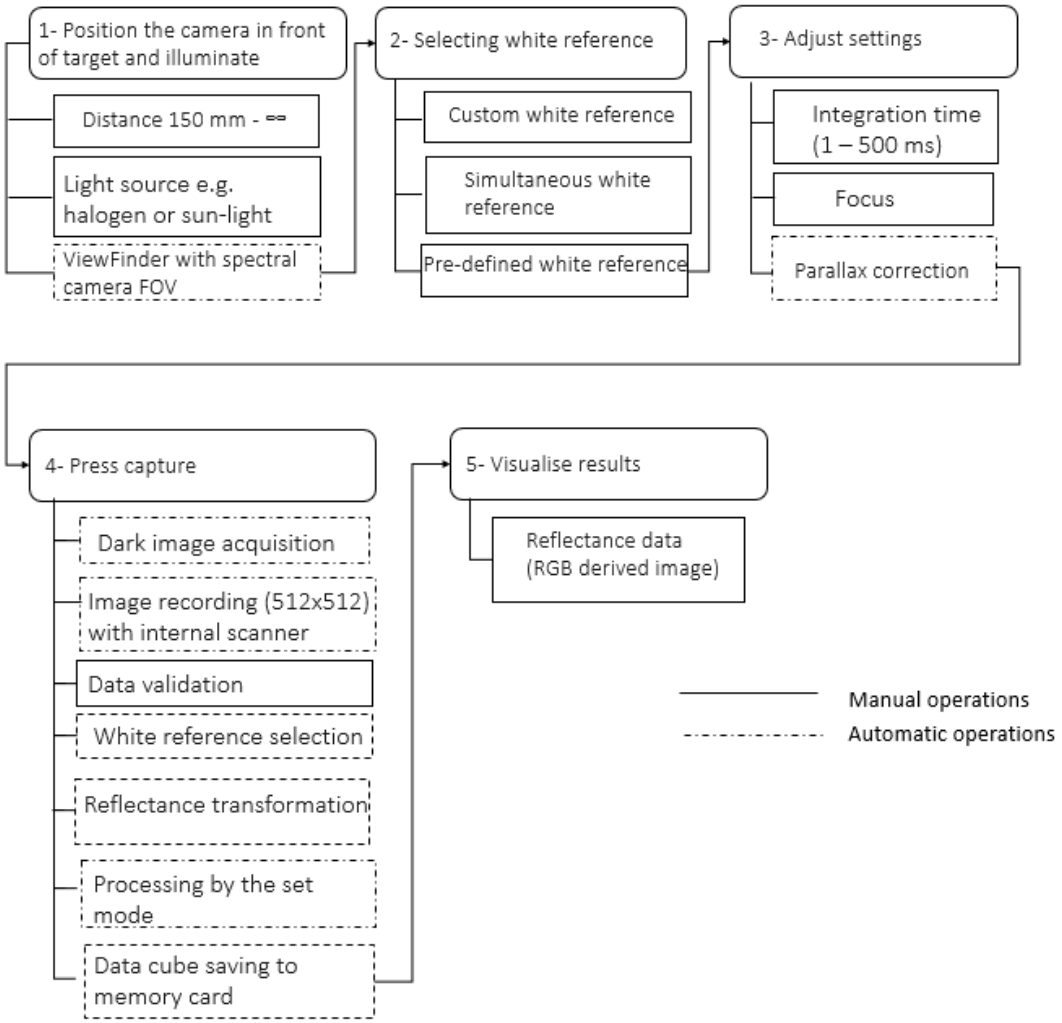

Figure 3.3: *General workflow of SpecimIQ (workflow is inspired by a similar representation provided by [10])*

- **Simultaneous white reference:** The measurement of a white reference can also be taken at the same time as the actual sample,by placing it in a scene, which is called simultaneous white reference.

- **Pre-defined white reference:** A general halogen spectrum from 400 to 1000 nm is provided with a device memory to be used in conditions where white reference recording is not possible. This is called pre-defined white reference.

In the custom and simultaneous white reference methods, The measurement is made over a white reference, and the data reflectance is computed using the average of 100 random spectra [10]. The Pre-defined white reference method immediately converts measured data to reflectance using a pre-defined spectrum [10]. In these cases of white reference, the data undergoes an automated reflectance transformation. Another approach is to capture the white reference and the target as separate images, the raw data of those images be used in the reflectance transformation, this is further explained in data acquisition section 4.2.

3.2.2.3 Adjust settings

Following the steps as given in Figure 3.3, some settings needs to be adjusted such as camera focus and integration time etc. The integration time of the spectral camera is preset by the viewfinder camera image. The user is given a fixed value and a preferred range, although the integration time can be manually adjusted in the range of 1–500 ms.

3.2.2.4 Capturing the Image

After making initial adjustments, image acquisition can be initiated by pressing the capture button. The data acquisition is performed in such a way that the dark reference is recorded at first automatically by a spectral camera. The dark reference is the representation of the sensor noise without any incoming light. After the dark reference acquisition, the actual data acquisition is started by a spectral camera.

3.2.2.5 Visualising and validating results

Once the entire image of 512 x 512 px is scanned, an RGB image is displayed as a validation view along with the intensity histogram. This RGB image is derived from the hyperspectral image and shown to the user, the user can reject the image or kept for further workflow, or it can be selected to save only raw, uncorrected data.

Specim IQ has three separate data processing modes : default recording mode (DRM), automatic screening mode (ASM), and application mode (AM). In DRM, also known as (a.k.a) no-processing mode, which saves the data in two seperate data cubes i.e. raw data and reflectance data[66]. The data set as shown in Figure 3.4 describes the folder structure in which the data is stored. In ASM a.k.a one-classifier, by defining a single identification class, it is possible to identify related items or materials from the recorded training data. AM is a deployed processing model provided by Specim IQ Studio. More information on the processing modes can be

found in [66]. In this research, DRM mode has been utilised. The dataset folder from Specim IQ has been retracted, containing raw datacube, white reference, dark frame, reflectance data cube, and auxiliary metadata. Raw data is the unprocessed data from the image sensor (see Table 3.3)

Table 3.3: *Overview of the files obtained by SpecimIQ [66]*

File	Description
.raw	Unprocessed data from the sensor in a row format
.hdr	Header files
.dat	Spectral reflectance data obtained from the device after default processing
.png	RGB images
.xml	Metadata and manifest

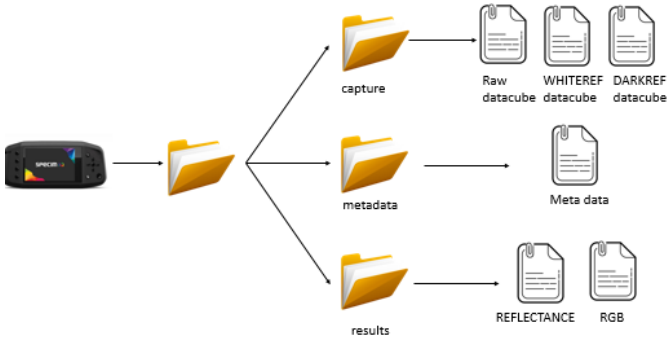

Figure 3.4: *Folder structure of dataset acquired by SpecimIQ [66] (inspired by a similar representation provided in [49])*

3.3 Spectroradiometer: JETI specbos 1211-L

Radiometric and colorimetric measurements can be performed using filter instruments (e.g., colorimeters) or spectrometer-based equipment. Filter-based instruments use three (or more) filters which are rotated one by one in front of the sensor for every acquisition. However, they are unable to capture the detailed spectrum [54]. As a result, only a limited range of measurement values such as luminance and chromaticity are acquired. Spectrometer-based instruments (spectroradiometers) can deliver more information, e.g. luminance, spectral radiance, optical resolution

and colour rendering index (CRI) [54]. Spectroradiometer specbos 1211 L [67] (see Figure 3.5), developed by JETI Technische Instrumente GmbH, provides sufficient measurement accuracy, is small and easy to integrate into the setup and requires minimal maintenance and recalibration. Standard spectroradiometers are calibrated using traceable standard light sources. The measured raw data from the device is transformed into the absolute spectrum using the spectral sensitivity, which is calculated during the calibration procedure at the manufacturer. To ensure measurement accuracy, this calibration must be repeated at least every two years. The resultant spectral radiance can be used to drive radiometric and colorimetric values according to the classical calculation schemes [54], such as:

- Spectral radiance and luminance
- CIE chromaticity coordinates x,y and u'v' (1976 UCS)
- colour rendering index (CRI)
- correlated colour temperature (CCT)

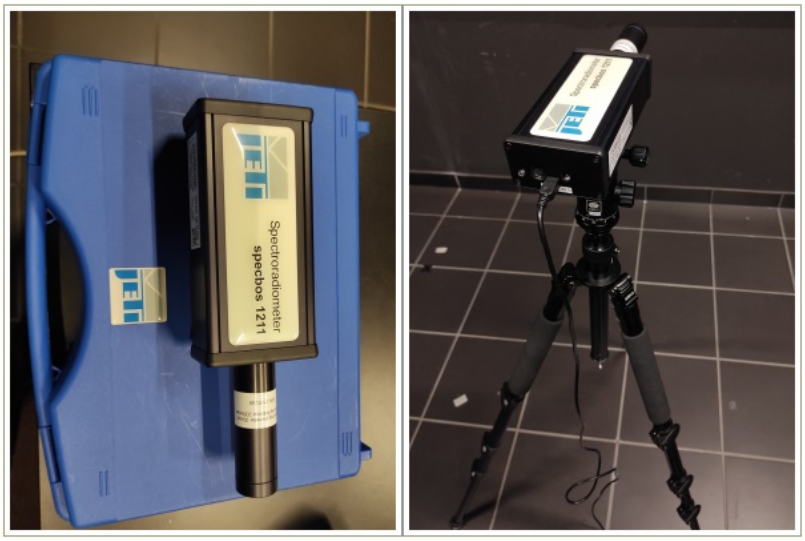

Figure 3.5: *JETI specbos 1211*

The JETI specbos 1211 L comes with PC software that allows you to capture and visualise the entire spectrum. However, we used the LuxPy library to acquire the spectral radiance measurements of wavelength 350 nm–1050 nm from the device and proceed with the calculations. The technical specifications of JETI Specbos 1211 L are given in Table 3.4.

Table 3.4: *Technical specification of JETI Specbos 1211 L [67]*

Feature	Value
Wavelengths range	350 (250) ... 1000 nm
Optical resolution (FWHM)	4.5 nm
Power supply	USB, RS 232, Battery, 9V-power supply
Weight	450 g
Dimensions	180 mm x 82 mm x 53 mm
Dynamic range (luminance)	0.1–2,500 cd/m2
Luminance accuracy	±2%
Luminance reproducibility	±1%
Chromaticity accuracy	±0.002 xy
Chromaticity reproducibility	±0.0005 xy
Operating temperature	10–40 °C
Integration time	20 ...5000 ms

3.4 Spectrophotometer: HunterLab UltraScan® PRO

Apart from spectroradiometers, spectrophotometers are other colour measurement devices that are commonly used in research studies as reference devices [73]. It is a more advanced instrument that measures an object's reflection and transmission over a different wavelength range for colour measurements [73]. The HunterLab UltraScan® PRO (see Figure 3.6) is a standard reference colour measurement spectrophotometer. It uses d:8° geometry with auto inclusion/exclusion of specular components to measure the spectral reflectance of a sample with the band gap of 5 nm in the wavelength range of 350 nm–1050 nm. It has three different reflectance measurement areas. The technical specifications of HunterLab UltraScan® PRO are given in Table 3.5.

The UV region of the illumination source has been calibrated for precise assessment of substances such as whitening agents, UV filters, and fluorescent colours [55]. It is also provided with EasyMatch QC software to facilitate measurements and visualise the measured spectral distribution (see Table 3.5). The general workflow of the device is represented in the Figure 3.7.

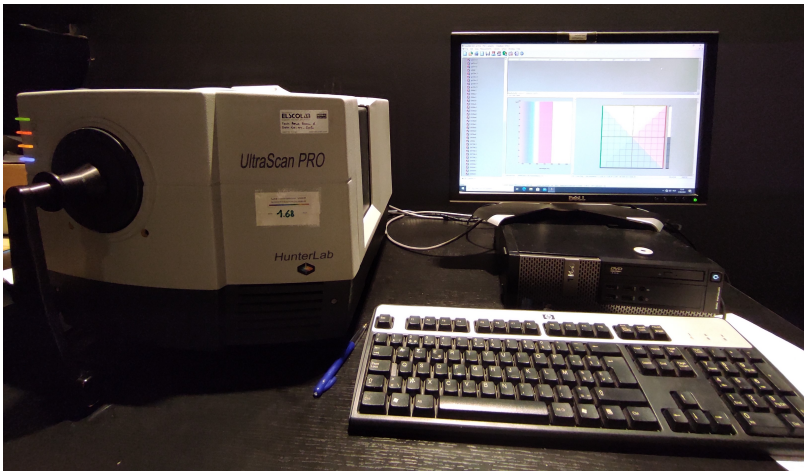

Figure 3.6: *HunterLab UltraScan® PRO*

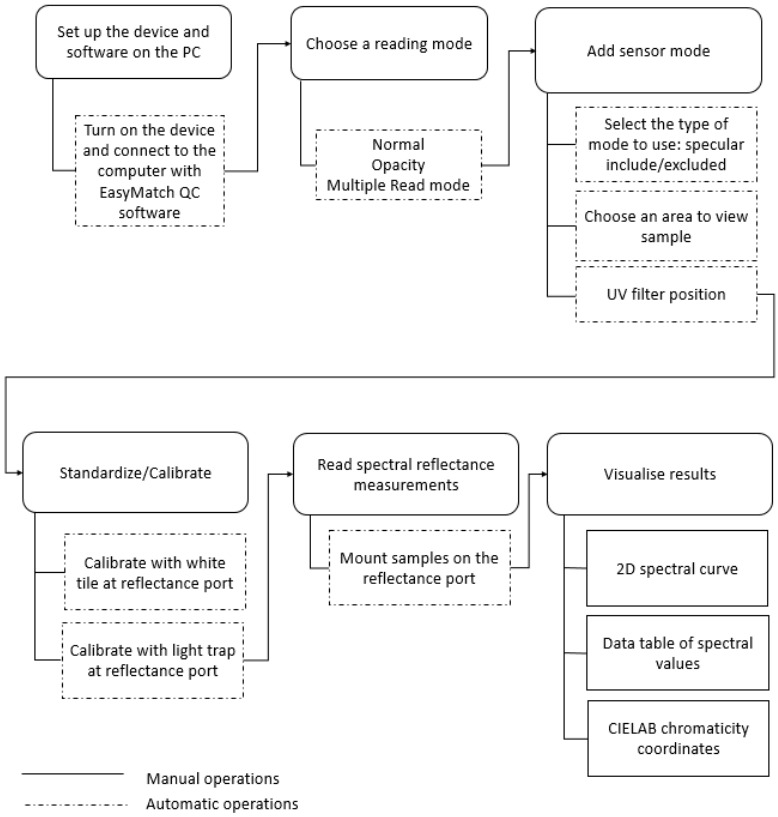

Figure 3.7: *General work flow of the Hunterlab*

Table 3.5: *Technical specifications of HunterLab UltraScan® PRO [32]*

Feature	Value
Wavelengths range	350 - 1000 nm
Optical resolution	5 nm
Geometry	diffuse d/8° reflectance, d/° total transmission, d/0° regular transmission
Sphere diameter	152 mm (6 in.)
Port Diameter/View Diameter	RSIN/RSEX reflectance modes • Large Area View (LAV): 25 mm (1 in) illuminated/19 mm (0.75 in) measured • Medium Area View (MAV): 13 mm (0.5 in) illuminated/9 mm (0.35 in) measured • Small Area View (SAV): 7 mm (0.25 in) illuminated/4 mm (0.16 in) measured
Light source	Pulsed Xenon lamps (3), calibrated and controlled in the UV range
Automatic UV Control	400 nm cutoff filter for UV control and UV exclusion
Weight	25.9 kg (57 lbs)
Dimension	Height: 32.3 cm (12.7 in.), Width: 42.0 cm (16.5 in.) Depth: 49.8 cm (19.6 in.)

3.5 Gloss meter: Rhopoint IQ 20/60/85 Gloss Haze DOI Meter

A gloss meter is a device which is used to measure the shininess of the surface of the object. In this research study, we have used a gloss meter "Rhopoint IQ 20/60/85 Gloss Haze DOI Meter" [33] to measure the glossiness of the samples (discussed in detail in later chapters). There are various geometries available to measure gloss, depending on the type of surface that needs to be studied. This device can measure gloss at specular angles of 20°, 60°, and 85°. We have measured the gloss of the samples at a specular angle of 60°, which is a standard geometry [77]. For the surfaces with high gloss finishes, the measurement of gloss at a specular angle of 20° is used, while surfaces with low gloss, the measurement at a specular angle of 85° is used [77]. Figure 3.8 shows Rhopoint IQ 20°/60°/85° Gloss Haze DOI Meter. Specifications of the instrument is provided in Table 3.6.

3.6 Python: Libraries and toolbox

Python [41] is an open source programming language that has a significant variety of libraries (such as numpy, SciPY, matplotlib, and pandas) that make it ideal for numerical computations, data analysis, and modelling. To assist with lighting and colour science related calculations, the LuxPY toolbox is used. The LuxPY toolbox is written in Python 3. It includes several lighting, colorimetric, color

Figure 3.8: *Rhopoint IQ 20/60/85 Gloss Haze DOI Meter*

Table 3.6: *Technical specifications of Rhopoint IQ 20/60/85 Gloss Haze DOI meter [33]*

Feature	Value
Measurement geometry	20° /60°/85°
Measurement Area	6 mm x 12 mm
Battery Type	Rechargeable lithium ion
Memory	8MB, 2,000 readings
Operating Temperature	15°C - 40°C (60°F - 104°F)
Dimensions	140mm (H) x 50mm (W) x 65mm (D)

appearance, and other colour science calculations that have proven useful in the research. Installation guidelines, basic architecture, operations, as well as various examples of usage are explained in [64].

4 Experimental methodology

The basic imaging pipeline (or measurement pipeline) needs the following fundamental components to acquire data from the scene: These are: scenes (or objects) to be captured, light sources to illuminate the scene, and detectors (i.e., devices to acquire the data). However, in practical terms, the acquired data for the same object can be considerably impacted by the method of data acquisition (including data acquisition geometry), system used (HSI system including different sensors) and other parameters influencing the general experimental setup [74]. For example, light sources provide illumination as a crucial part of spectral imaging. The illuminance of the scene as well as type of light sources have an impact on vision systems. Similarly, the performance of the light sources can significantly impact the quality of acquired data as well as overall efficiency and accuracy of the system [80]. Good illumination can contribute towards the quality of image acquisition as well as processing and analysis by reducing noise, reflection, and improve image contrast [39]. Additionally, when selecting the most appropriate illumination conditions, the type of the light source, colour quality, and the position of the light source in a setup should be taken into consideration. Additional factors that impact the data accuracy can be the method of estimation scene illumination, i.e. with a white reference standard type, etc. Hence, it is important to investigate essential components of the experimental setup in order to identify the factors that can compromise the accuracy and high quality of the data.

The experimental setup is described in section 4.1 of this chapter. Using the described setup, data is collected under various illumination conditions that are described in section 4.1.1. The data collection and processing from both the devices are described in Section 4.2. As for the comparative approach, see section 4.3.

4.1 Experimental setup

The experiment is carried out inside a lab that has dark surroundings. The test object, i.e., the MacbethCC (see section 3.1), is positioned right in the middle of the scene on a table at a height of 1.099 m from the ground, and the whole surroundings

of the object are provided with a sufficient amount of illumination. The illumination is produced by a light source (light sources used in the setups are explained in detail in 4.1.1) placed at a distance of approximately 2 m from the target pointed directly at the test object. To test the uniformity of the colour patches of MacbethCC, we examined the reflectance spectra derived from various locations on the patch. The results indicate that the uniformity within the respective patch is satisfactory.

The measurement device, i.e., the specimIQ camera (explained in section 3.2) or Jeti spectroradiometer (explained in section: 3.3) (a spectroradiometer connected to the computer), is placed on a tripod at a distance of about 0.8 m from the target and at a height of approx. 1.0 m from the ground. The experimental setup is represented in Figure 4.1.

Using the experimental setup, we acquired the data from two devices. SpecimIQ camera and Jeti spectrophotometer. A white uniform sheet (refer to as white_kapa) is used as the white reference standard (explained in section 3.2.2.2). The reflectance of the white_kapa is measured with the HunterLab Ultrascan® PRO device (explained in section: 3.4), and interpolated within in the range of 360–830 nm, as shown in Figure 4.2.

4.1.1 Lighting condition

The illumination is a key element of the measurement setup. The object needs to be properly illuminated in order to be captured by the device. There are various types of light sources that can be used, including fluorescent, incandescent, and

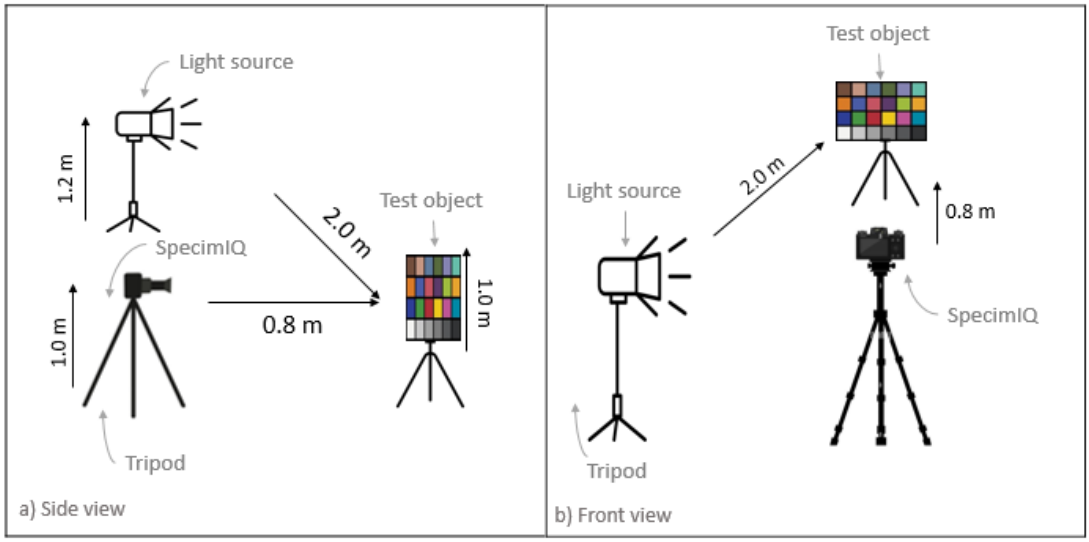

Figure 4.1: *Semantic representation of the acquisition setup*

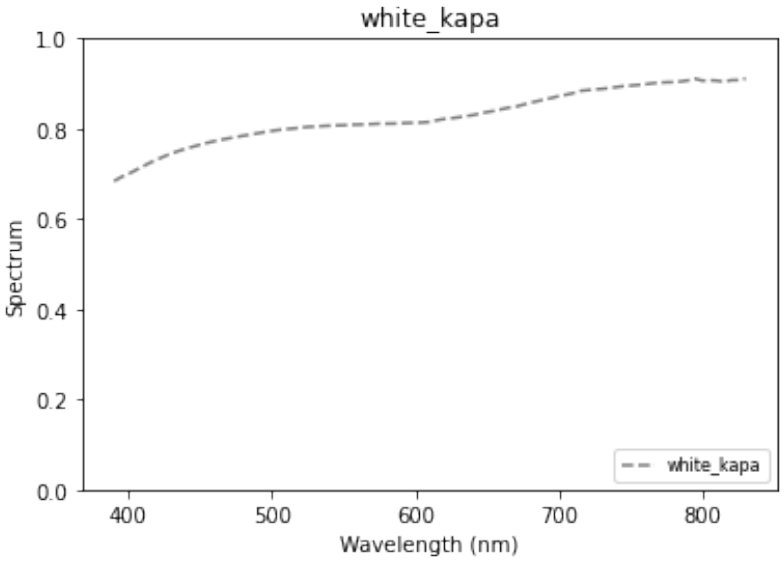

Figure 4.2: *The spectral reflectance of the white reference standard sheet (white_kapa), measured using HunterLab Ultrascan® PRO*

light-emitting diodes (LED) for indoor setups, as well as natural light sources, such as the sun, for outdoor settings. Each type of light source has a different spectral power distribution (SPD) (i.e., power as a function of wavelength).

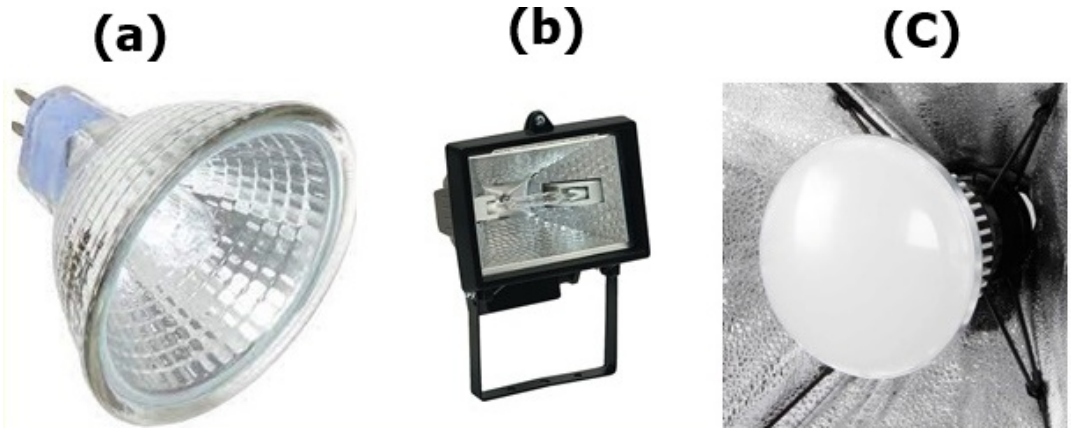

Figure 4.3: *Three different types of light sources used in an experimental setup for acquisition(a)H_50Wattx1 (b)H_400Wattx1 (c)L_50Wattx1. The letters H and L in their names represent halogen and led, respectively,followed by a number that denotes power in watts, while x1 refers to the number of lights used in the setup i.e. 1 in these cases.*

The illuminance at a sample position of the same type of light might vary

depending on the manufacturer and power (watt). The validity of the measured spectral reflectance is significantly influenced by the light source [81].

One of the important requirements of the imaging of art-work in museums is maximum light exposure to minimise light induced ageing of the objects. Typically, when a white light source is used to illuminate objects in museums, UV and thermal radiation are eliminated from them [40]. The recommended illuminance for the artworks is between 150 lux and 200 lux, whereas for the manuscripts and other paper-based artworks, the recommended illuminance is 50 lux [40].

In general, the reciprocity principle holds [40], which says that "light-induced damage is determined by the total energy incident on a material rather than the illuminance of the incident light. To achieve the same signal to noise ratio in an image, the object can either be illuminated with low illumination for a longer period of time or with high illumination for a shorter period of time" [40].

To investigate the effects of various light sources on hyperspectral imaging in terms of radiometric, photometric, and colorimetric differences (explained in section 4.3.1 and 4.3.2 respectively), we carried out experimental studies under various lighting conditions, i.e. incandescent lights (halogen light), LEDs, fluorescent lights and metalhalide lamp in several case studies with varying illuminance. A brief explanation of them is provided below and summarised in Table 4.1

Table 4.1: *Lighting conditions involved in the experimental study*

	1	2	3	4	5	6
Lighting Conditions	H_50Wattx1	H_400Wattx1	G_315Wattx1	G_560lux1	L_50Wattx1	CFL_23Wattx1
Description	Halogen light	Halogen spotlight	Metal Halide grow light	MH light(reduced illuminance)	LED light	Compact fluorescent light
Power (Watt)	50 Watt	400 Watt	315 Watt	315 Watt	50 Watt	23 Watt
Illuminance (lux)	200 lux	793 lux	1600 lux	569 lux	316 lux	148 lux
CCT (K)	3157 K	2968 K	9632 K	9340 K	5442 K	5487 K
Manufacturer	USHIO	as schwabe	iGrowtek	iGrowtek	Unknown	True-Light®

4.1.1.1 Halogen Light Source

The halogen light source is a type of incandescent light that uses a halogen gas to enhance light output and rated life [2]. They are known for their relatively ameliorated efficiency, good light quality, and long-rated lifespan when compared to regular incandescent light sources. [2]. To illuminate museum artefacts such as artworks, tungsten-halogen sources with ultraviolet filters are frequently used [57]. Our experimental study involves two different halogen bulbs. One is a small 50-watt halogen light sources (H_50Wattx1) (see Figure 4.3 (a)) with a filter; it has a correlated colour temperature (CCT) of 3157 K and is mounted in a tiny circular reflector. It emits a warm yellowish light. The other halogen light source is a 400 Watt spot light (H_400Wattx1) (see Figure 4.3 (b)). It produces warm light

Figure 4.4: *Lighting conditions used in the experimental setup during data aquistions d) CFL_23Wattx1 (e) G_315Wattx1. The CFL and G in their names represent for compact fluorescent lamp and MH grow lamp respectively, followed by a number that denotes power in watts and x1 refers to the number of lights used in the setup i.e. 1 in these cases.*

with a CCT of 2968 K. Incandescent light sources have a continuous spectrum. The spectral power distribution (SPD) of H_50Wattx1 and H_400Wattx1 is shown in Figure 4.5

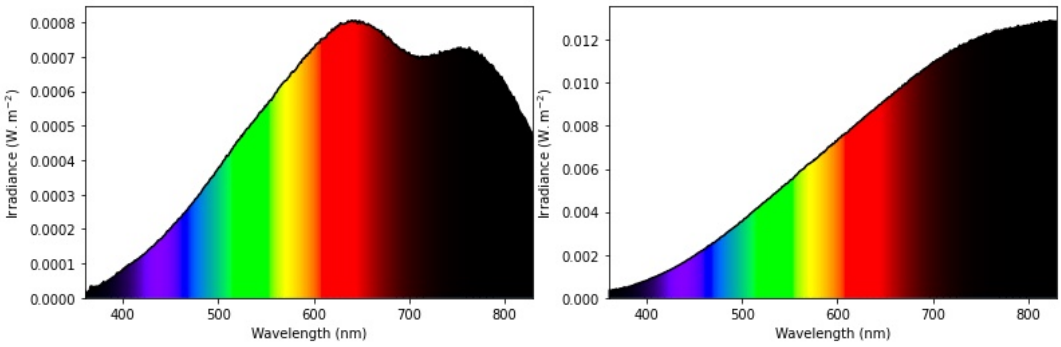

Figure 4.5: *SPD of light sources H_50Wattx1 (left) and H_400Wattx1 (right). Both of these sources are halogens, and power grows linearly with wavelength (nm). They have less energy at the shorter wavelengths of EM (350 nm-450 nm)*

4.1.1.2 HID MH Grow light

High intensity discharge HID light sources are renowned for their high brightness and light output. These light sources produce a remarkable spectrum of light that more closely resembles natural sunlight than any light available today . The metal halide (MH) grow light G_315Wattx1 (see Figure 4.4 (e)) is a type of HID source, with a power of 315 Watt, a lumen of 22000 lm, and a CCT of 10,000 K; it emits a bluish spectrum of light. The spectral power distribution (SPD) of G_315Wattx1 is shown in Figure 3.3 (a). It is an enhanced blue light. It contains high energy in the lower end (i.e., blue region 350 nm-450 nm) of the spectrum.

G_315Wattx1 will be used in the experiment to better understand how accurate image reproduction can be achieved with this type of light because, in general, image sensors have low sensitivity at lower wavelengths. Considering the high luminous flux of the light source,another lighting condition (namely G_560lux1, the letter G in the name represent Grow, followed by the number that denotes illuminace in lux and 1 refers to the number of lights used in the setup) derived from G_315Wattx1 is used.In G_560lux1, the illuminance reaching the target has been decreased from 1600 lux to 560 lux by illuminating the scene indirectly. The light source was facing upward rather than toward the object. Figure 4.6 shows the SPD of G_560lux1.

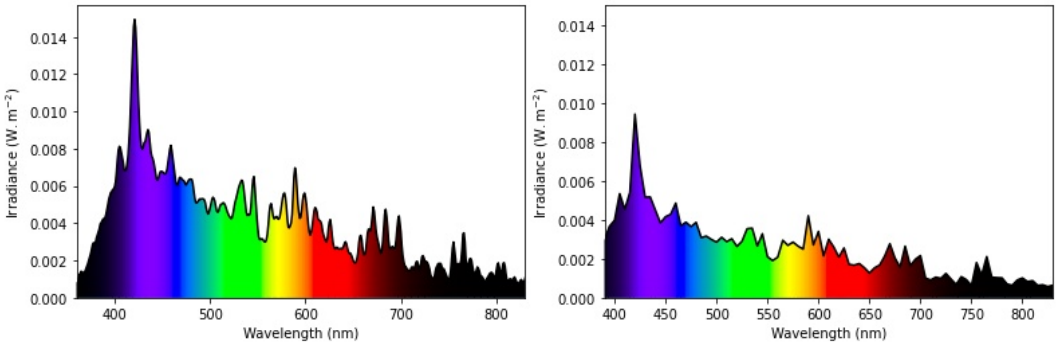

Figure 4.6: *SPD of G_315Wattx1 (left) and G_560lux1(right). They have higher energy at the shorter wavelengths of EM (350 nm-450 nm).G_560lux1 lighting condition is derived from the G_315Wattx1, i.e. illuminance of the G_315Wattx1 is reduced, which is visible in the SPD of G_560lux1.*

4.1.1.3 Light emitting diode (LED)

LEDs are regarded as an efficient illumination source as they are more efficient and more durable than conventional incandescent sources [57]. Nowadays, LEDs are the first choice for applications involving the arts since their spectral properties

enable the visible illumination of works of art and cultural heritage (CH) without exposing them to damaging UV or IR light [72]. We investigated the effects of using LED sources for HSI acquisitions and how they affected image reproduction. The 50 Watt LED light L_50Wattx1 (see Figure 4.3 (c)) has a CCT of 5442 K and emits cool light similar to daylight. The SPD of the L_50Wattx1 is shown in Figure 4.7 It can be seen from the SPD of the light source that there is only a peak at around 450 nm, which indicates that this source emits a significant amount of energy at this wavelength.

4.1.1.4 Compact fluorescent light (CFL)

CFL_23Wattx1 is a Compact fluoresecent light (CFL) (see Figure 4.4 (d)), typically a fluorescent lamp consisting of a low-pressure mixture of mercury and a rare gas like Argon, It's a 23-watt light source and produces 1300 lumen of white light with a CCT of 5480 K. Figure 4.7 shows the SPD of CFL_23Wattx1. As shown from the Figure, the spectrum of the CFL source is full of peaks and depths. It implies that this light source will emit different amounts of energy at various wavelengths of energy over a visible range of the spectrum.

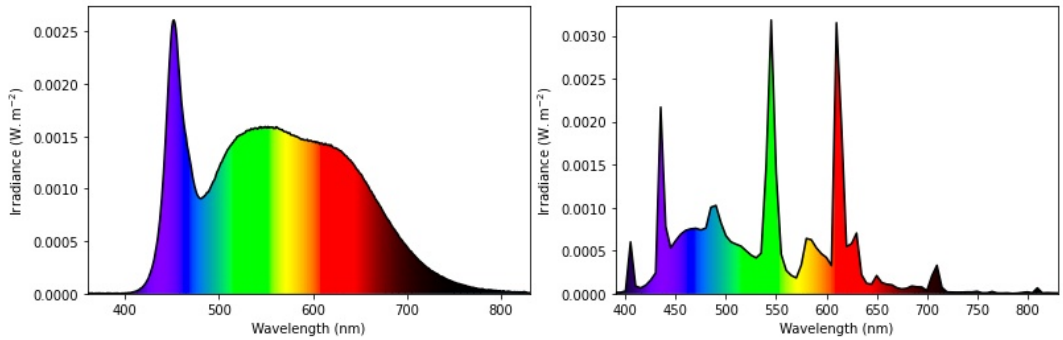

Figure 4.7: *SPD of L_50Wattx1 (left) and CFL_23Wattx1 (right). It can be seen that SPD of L_50Wattx1 has only a peak at around 450 nm, while SPD of the CFL source is full of peaks and depths.*

4.2 Data acquisition procedure

In order to access the radiometric, photometric, and colorimetric accuracy of the acquisition process of the SpecimIQ, ground truth or reference data is required to perform evaluation. This comparison enables us to evaluate the accuracy of data acquired by specimIQ. Ground truth data is the sepctral reflectance calculated

from spot measurements acquired with the JETI Specbos 1211 L. Data acquisition from both the devices is explained as follows.

4.2.1 Acquisition of the ground truth data

Spot measurement devices such as spectroradiometers only allow the acquisition of data at a certain number of points on the object's surface. The JETI Specbos 1211 L spectroradiometer performs acquisitions with precision in the range of 350–1000 nm of the EM; it has been used as a reference instrument in research and development [72].

Ground truth data is provided for reference by taking spot measurements with JETI Specbos 1211 L within the range of 360 nm and 830 nm with a 1 nm interval. The diameter of the measurement spot size is 24 mm, and it is pointed at the middle of the sample. For each sample (i.e., a colour patch n of 24 Macbeth colour checker colours), a spectral radiance $(L_{sample}(n, \lambda))$ measurement was taken. As an estimate of the scene illuminant, the spectral radiance $(L_{white}(n_w,\lambda))$ of a white reference sample is recorded (at the same position as the sample) for each colour patch measurement. JETI Specbos 1211 L is equipped with both automatic integration time adaptation and dark-current subtraction to provide spectral radiance ($Wm^{-2}sr^{-1}/nm$) directly. The workflow of the data acquisition is shown in fig 4.8. The spectral measurements using JETI Specbos 1211 L are taken five times, one imediately following the other for both the colour patch and white reference. The spectral data is interpolated (using luxPy interp1() function which utilises cubic spline interpolation) to a wavelength range of 390 to 830 nm with a 5 nm interval. The data is interpolated to this range as it will be compared to the data of specimIQ (detail are given in section 4.2.2) The reflectance of the sample is calculated as follows:

$$R(n, \lambda)_{\mathrm{gt}} = L_{\mathrm{sample}}(n, \lambda)/L_{\mathrm{white}}(n_{\mathrm{w}}, \lambda).R(\lambda) \tag{4.1}$$

Where n = *1,2,...24*, λ = *390 - 830 nm* & $R(\lambda)$ = spectral reflectance of white_kapa. $R(n,\lambda)gt$ is the spectral reflectance of the sample n. 1 value is acquired for each of 24 colour patches, which serve as the ground truth data for comparison.

4.2.2 Acquisition of the HSI data

With SpecimIQ, 204 bands are captured in the 400-1000 nm wavelength range with a spatial resolution of 512x512 pixels and an interval of approximately 2.9 nm. First, we acquired the image of the test object itself, MacbethCC. Then the uniformly reflecting white reference (described in section 3.2.2.2) of the same size

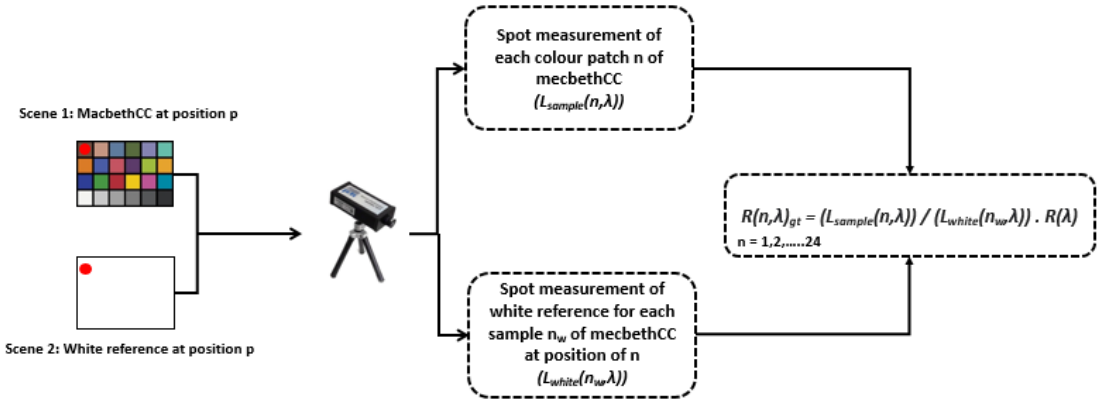

Figure 4.8: *Workflow of the acquisition of ground truth data (R(n,λ)gt) from JETI Specbos 1211 L*

is placed in the scene and a second image is taken. The second image is captured to estimate the illumination of the scene for each pixel of the MacbethCC . Data is acquired with the default mode (explained in section 3.2.2.5).We chose the default mode to capture the data from the camera. Typically, the spectral reflectance can be directly obtained from the SpecimIQ, which is transformed from the camera by means of operations (depending on the settings (explained in section 3.2.2.5]). However, it is recommended to use raw image files rather than processed image files to obtain consistent colour information.The workflow of the acquisition is shown in fig 4.9.

Specim IQ provides a raw spectral file and an hdr data file (see Table 3.3), including detailed information in ENVI format. The provided raw data $I_{raw}.data$ in units *counts* is used to obtain the spectral radiance (L_{scene}) of the captured scenes, i.e., L_{mcc} and L_{white}. Preprocessing is required to obtain spectral radiance (L_{scene}) from the sensor raw data, which requires integration time I_{i_time} correction and subtracting the dark current I_{dark} from the data as follows:

$$\begin{aligned} L_{\text{raw}} &= I_{\text{raw}}.data \\ L &= L_{\text{raw}}/I_{\text{i\_time}} \\ L_{\text{scene}} &= L - I_{\text{dark}}.data \end{aligned} \tag{4.2}$$

The spectral reflectance at each picture location was then calculated by dividing the spectral radiance of each pixel in the first captured image by the spectral radiance of the white reference of the same pixel.

$$R(\lambda)_{\text{target}} = L_{\text{mcc}}(\lambda)/L_{\text{white}}(\lambda).R(\lambda) \tag{4.3}$$

where $R(\lambda)$ = spectral reflectance of *white_kapa*

$R(\lambda)_{target}$ is the spectral reflectance of a target scene of size 512x512x201 and is referred to as a target data.

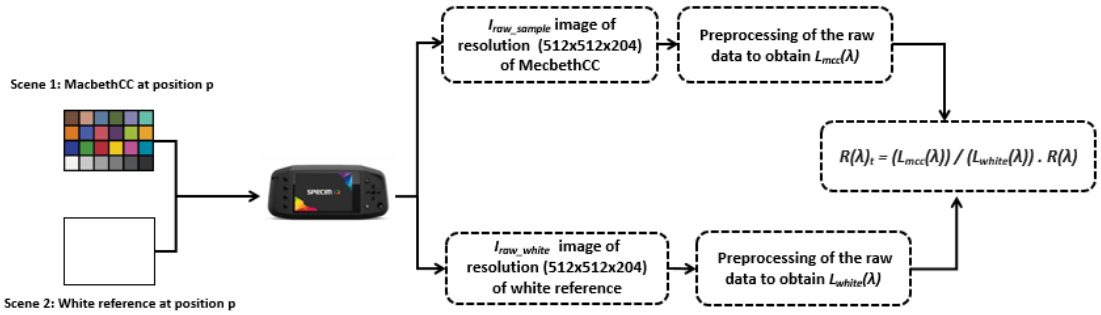

Figure 4.9: *Workflow of the acquisition of target data ($R(\lambda)_{target}$) from SpecimIQ*

4.3 Evaluation method

The ground truth data $R(n,\lambda)_{gt}$ consists of 24 spectral reflectance values calculated within the range of 390 nm-830 nm with a 5 nm spacing for each of the MacbethCC 's 24 colour patches, while the target data is $R(\lambda)_{target}$ is the hyper spectral image of size 512x512x201. Spectral reflectance is derived from the central region of each color patch (as shown in image 4.10) and averaged to represent the patch's spectral reflectance. The spectral reflectance data is interpolated in the similar way to the range of 390 nm - 830 nm to perform the comparison.This data will be referred to as $R(n,\lambda)_{target}$

The retrieved reflectance spectrum from each colour patch was then compared with the ground-truth spectrum of the same colour. The evaluation of the ground truth data and target data from both devices is being done in terms of radiometric [4.3.1] and colorimetric [4.3.2] assessment.

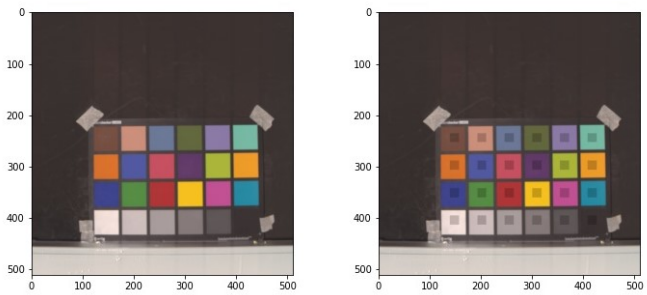

Figure 4.10: *The swatches of the colour patches extracted from the MacbethCC*
.

4.3.1 Radiometric evaluation

Plotting two spectra allows for a better evaluation of how the function curves differ from one another and whether noise exists across a certain wavelength range, etc. However, to quantify those differences, for each colour patch, the root mean square Error (RMSE) is calculated between the two sets of data, namely $R(n,\lambda)_{gt}$ and $R(n,\lambda)_{target}$. RMSE is typically used to compute the error between two curves and is computed as follows:

$$RMSE = \sqrt{\frac{1}{n}\Sigma_{i=1}^{n}(R(n,\lambda)_{\text{gt}} - R(n,\lambda)_{\text{target}})^2} \tag{4.4}$$

4.3.2 Colorimetric evaluation

The colorimetric values for each color patch are calculated using $R(n,\lambda)_{gt}$ and $R(n,\lambda)_{target}$. For the colorimetric difference, we have chosen u'v' (CIE 1976 UCS) chromaticity diagram and CIELAB.

4.3.2.1 u'v' Chromaticity diagram (CIE 1976 UCS)

u'v' is a uniform chromaticity diagram, the perceived difference in colour is approximately proportional to the distance between the points. The u'v' (as shown in equation 4.5) represents the chromaticity coordinates [9].

4.3.2.2 CIELAB Colour space

The CIE $L^*a^*b^*$ (CIELAB) colour space is based directly on the tristimulus values in CIE XYZ. L^* represents the lightness. "The axis a^* represents red to green with positive a^* indicating redness and negative a^* indicating greenness. Similar

to this, the b^* axis shows yellow to blue, with positive values indicating yellowness and negative values indicating blueness" [78, 9]. There is no luminance-level dependency in CIELAB. As a result, it is totally unable to predict luminance dependent impacts. In general, CIELAB values will vary when the illuminant varies. It would be reasonable to suppose that these changes to the CIELAB values would correspond to the apparent change in colour that a human would experience [62].

4.3.2.3 Colour calculation

Through LuxPy (see section 3.6), the colorimetric values are computed. Spectral reflectance (i.e. $R(n,\lambda)_{gt}$ and $R(n,\lambda)_{target}$) are converted into tristimulus values (XYZ), with values $SPD = D65$, *Illuminant E* and 2° standard observer CIE 1931 colour matching function CMF . XYZ tristimulus values are converted into u'v' CIE 1976 UCS chromaticity diagram chromaticity coordinates as follows [79]:

$$\begin{aligned} u' &= \frac{4.0 * X}{X + 15 * Y + 3 * Z} \\ v' &= \frac{9.0 * Y}{X + 15 * Y + 3 * Z} \end{aligned} \tag{4.5}$$

The colour difference between the two $R(n,\lambda)_{gt}$ and $R(n,\lambda)_{target}$ is $\Delta Eu'v'$ and is computed as follows:

$$\Delta Eu'v' = \sqrt{\frac{1}{n}\Sigma_{i=1}^{n}[(u'_{\text{gt}} - u'_{\text{target}})^2 + (v'_{\text{gt}} - v'_{\text{target}})^2]} \tag{4.6}$$

A just noticable colour difference can be estimated as 1 $JND \approx 0.0033$ u'v' [50], denoted as *JNDu'v'* in the study.

For the CIELAB colour space chromaticity coordinates calculations, tristimulus values XYZ are converted into $L^*a^*b^*$ as follows [61]:

$$\begin{aligned} L^* &= 116 * f * (\frac{Y}{Y_n}) - 16 \\ a^* &= 500[f(\frac{X}{X_n}) - f(\frac{Y}{Y_n})] \\ b^* &= 200[f(\frac{Y}{Y_n}) - f(\frac{Z}{Z_n})] \end{aligned} \tag{4.7}$$

where n represents value for the white point. L^* represents lightness of a colour, a^* and b^* represents two opposite chromaticity coordinates. The colour difference between the two $R(n,\lambda)_{gt}$ and $R(n,\lambda)_{target}$ is ΔE^*ab and is computed as follows:

$$\Delta E^* ab = \sqrt{\frac{1}{n} \Sigma_{i=1}^{n} [(a^*{}_{\mathrm{gt}} - a^*{}_{\mathrm{target}})^2 + (b^*{}_{\mathrm{gt}} - b^*{}_{\mathrm{target}})^2]} \tag{4.8}$$

5 Experimental tests, results and discussion (part 1)

This chapter provides an overview of the case studies that have been conducted as part of the research; for each study, the findings and conclusions are provided, along with a discussion.

5.1 Experimental test 1: Effects of the light source on the accuracy of the acquired data

The importance of the light source that illuminates the scene in the experimental setup of the imaging setup has already been emphasised in section 4.1.1. However, in order to conduct the practical study and quantify the effects on data acquisition, we investigated five different light sources. Before performing the acquisition of the data, i.e. $R(n,\lambda)_{gt}$ and $R(n, \lambda)_{target}$, the stability of the light sources was tested.

5.1.1 Stability of the light source

A stable light source is important to obtain meaningful measurement data and to guarantee measurement repeatability. Stable results require stable light sources. Any type of light may experience changes in its spectral power distribution over time. Both long-term and short-term changes can be included in this. For instance, some light sources typically change their SPD and emit a significant quantity of energy as they heat throughout their warmup period [5]. During the warmup period, an increasing amount of energy causes changes in SPD, and results may vary when measurements are acquired during this time. Hence, to find the time by which each lamp stabilises, we tested the stability of each light source [5].

To test the stability, point measurements were taken with JETI Specbos 1211 L on *white_kapa*. First the lamp was switched on and spot measurement was recorded (i.e. spectral radiance $L(\lambda)$), measurement were recorded from 1 minute of time (t) upto 20 minutes with 1 minute (in some cases 2 minutes) interval. To comprare this, one measurement is taken after one hour t_{60} (one hour from the first measurement). The spectral irradiance $E_e(\lambda)$ is computed from the measured spectral radiance $L(\lambda)$ at each time (t) as follows:

$$E_e(\lambda) = L_t(\lambda)/R(\lambda) \tag{5.1}$$

where $R(\lambda)$ is the spectral reflectance of white_kapa and $L_t(\lambda)$ is the spectral radiance of white_kapa captured at time (t).

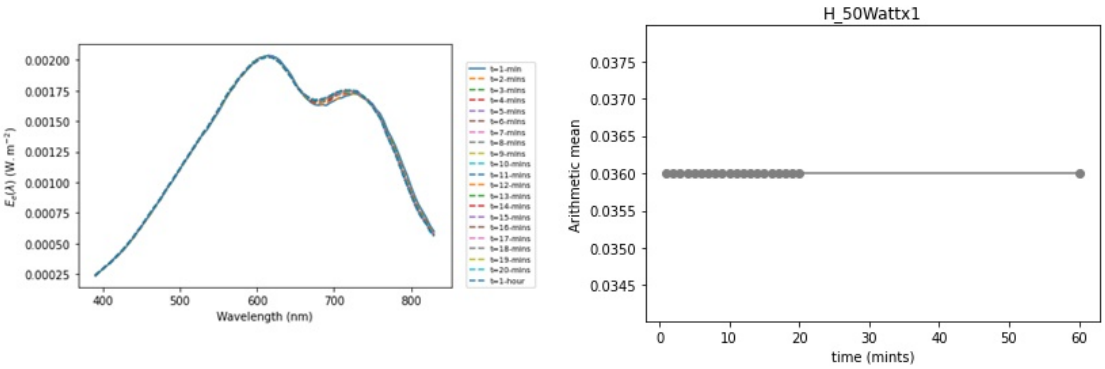

Figure 5.1: *a) The $E_e(\lambda)$ recorded over time (t) of H_50Wattx1 is shown at the left & b) $E_e(\lambda)_{average}$ (i.e. arithmetic mean) is plotted as a function of time (t) of H_50Wattx1 is shown at the right. $E_e(\lambda)_{average}$ is appear to be stable over time t_{60}.*

The $E_e(\lambda)$ for time (t) is plotted in Figure 5.1 (a). The arithmetic mean of $E_e(\lambda)$ recorded over time is calculated (rounded up to three decimal points) (called as $E_e(\lambda)_{average}$) and is plotted as a function of time (t). For the case of H_50wattx1 in Figure 5.1 (b), it can be seen from the Figure that the $E_e(\lambda)_{average}$ is at time t_1 as high as at time t_{60}. It does not require time to heat up and reach its maximum value. Furthermore, Figure 5.1 indicates that it remained stable throughout time (t). In the case of H_400wattx1, as seen in Figure 5.2 (a), spectra experience negligible shifts over time. Figure 5.2 (b) shows that the stability of the lamp does experience some changes over time. The $E_e(\lambda)_{average}$ is high as the light is turned on. After a few minutes, the $E_e(\lambda)_{average}$ goes up and down for a few minutes, and then it becomes stable again until t_6. Because the recorded $E_e(\lambda)$ of H_400wattx1 is high from the start, it does not take time to obtain maximum intensity. However, it appears that it requires some time to stabilise.

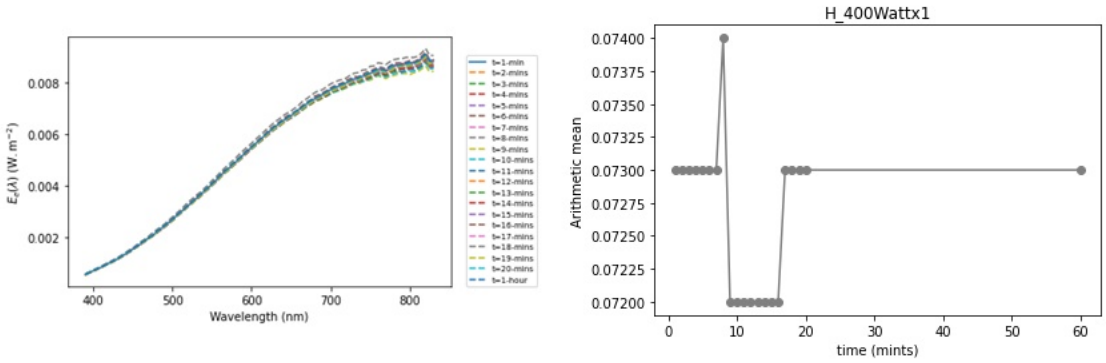

Figure 5.2: *a) The $E_e(\lambda)$ recorded over time (t) of H_400Wattx1 is shown at the left & b) $E_e(\lambda)_{average}$ (i.e. arithmetic mean) plotted as a function of time (t) of H_400Wattx1 is shown at the right. $E_e(\lambda)_{average}$ is appear to go up and down for few minutes until it stabilise over time (t).*

The intensity of the G_315Wattx1 (also applies to the G_560lux1) is quite low when the light is turned on (i.e. t_1), but it gradually rises within a few seconds and can be seen in the scene. Figure 5.3 (a) shows that the spectral distribution acquired at t_1 is relatively low but rises within the minute. Similarly, Figure 5.3 (b) shows that when the light is turned on, the $E_e(\lambda)_{average}$ is very low, and it reaches its maximum value after a few minutes.

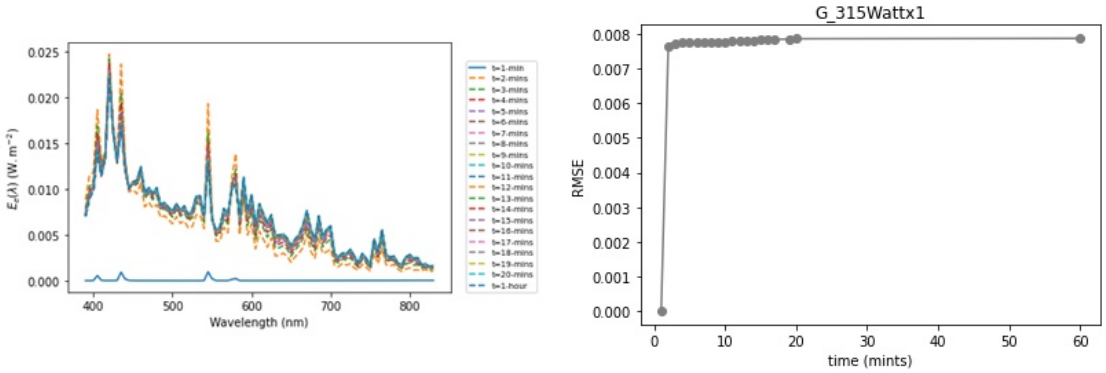

Figure 5.3: *a) The $E_e(\lambda)$ recorded over time (t) of G_315Wattx1 is shown at the left & b) $E_e(\lambda)_{average}$ (i.e. arithmetic mean) plotted as a function of time (t) of G_315Wattx1 is shown at the right. It appears that $E_e(\lambda)_{average}$ is very low at time t_1, and it reaches its maximum value after a few minutes.*

Similar behaviour has been observed in the case of CFL_23Wattx1, which appears to have a very low $E_e(\lambda)$ that increases over time. As a result, it can be said that it takes some time to reach its maximum light intensity value (see Figure

5.4).

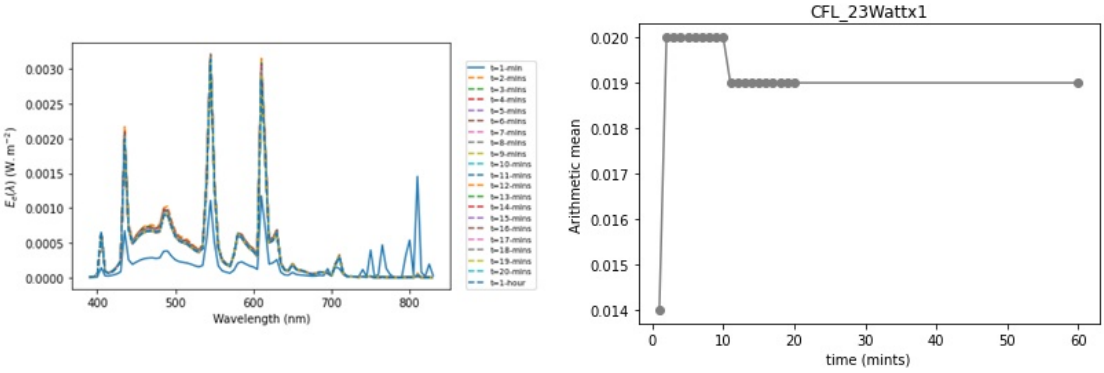

Figure 5.4: *a) The $E_e(\lambda)$ recorded over time (t) of CFL_23Wattx1 is shown at the left & b) $E_e(\lambda)_{average}$ is plotted as a function of time (t) of CFL_23Wattx1 is shown at the right. It appears that, similar to G_315Wattx1, $E_e(\lambda)_{average}$ is very low at t_1, and it reaches its maximum value after a few minutes.*

In the case of L_50Wattx1, Figure 5.5 (a), shows that the intensity of the light source is high as it turns on. However, the spectra appear to vary over time in the mid part of the spectrum. It does undergo some changes over time (t) (see Figure 5.5 (b)).

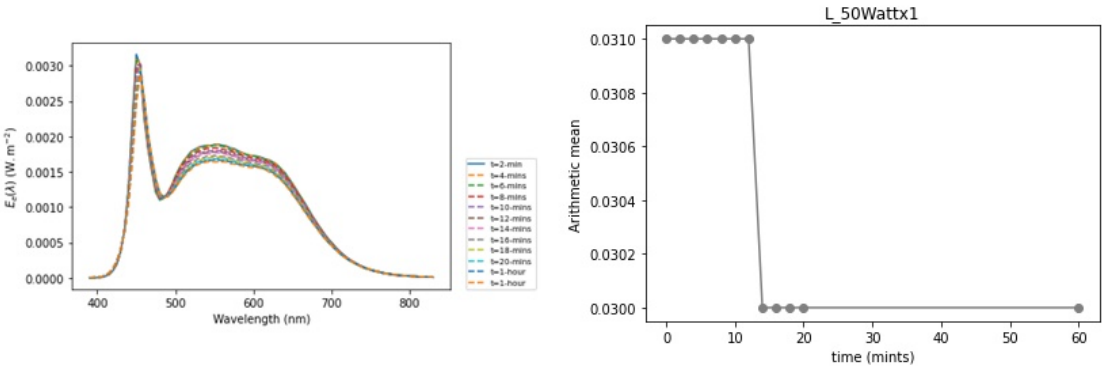

Figure 5.5: *a) The $E_e(\lambda)$ recorded over time (t) of L_50Wattx1 is shown at the left & b) $E_e(\lambda)_{average}$ (i.e. arithmetic mean) is plotted as a function of time (t) of L_50Wattx1 is shown at the right. It appears that, $E_e(\lambda)$ experience some changes over time (t).*

Based on the above evaluation, it appears that each light source behaves differently; some are stable as soon as they switch on, while others need some time to attain their maximum light intensity. After some time, all five of them achieve stability. Aside from the reputability of results, another essential purpose

to examine light stability is to determine how long it takes a specific light source to stabilise. It is necessary to understand this in order to estimate the time of acquisitions in the museum.

5.1.2 Data acquisitions

After stabilising the light sources, the data $R(n,\lambda)_{gt}$ and $R(n, \lambda)_{target}$ is acquired. The exposure time and illuminance for each of the lighting conditions is shown in table 5.1. Illuminance for the acquisition of the hyperspectral image $R(n, \lambda)_{target}$ is recorded using a luxmeter, the detector of the device is positioned at the middle of the test object to record the intensity *(lux)* reaching to the object. The Table 5.1 data shows that there is an inverse relationship between exposure time and illuminance. Object needs to be illuminated with either a low intensity of light for a long period of time or with a high intensity of light for a shorter period of time to achieve the image with a good signal-to-noise ratio. The obtained results are discussed in the following sections.

Table 5.1: *Illuminanace and exposure time of image acquisition for different lighting conditions.*

Lighting Condition	Illuminance	Exposure time
H_50Wattx1	200 lux	2 minutes and 56 sec
H_400Wattx1	793 lux	1 minute and some sec
G_315Wattx1	1600 lux	1 minute and 06 sec
G_560lux1	569 lux	1 minute and 59 sec
L_50Wattx1	316 lux	2 minutes and 58 sec
CFL_23Wattx1	148 lux	2 minutes and 12 sec

5.1.3 Results & discussion

The results are analysed in terms of radiometric, photometric and colorimetric evaluations. They are as follows:

5.1.3.1 Radiometric evaluation

The average RMSE and standard deviation between $R(n,\lambda)_{gt}$ and $R(n,\lambda)_{target}$ of 24 colour patches under all lighting conditions is displayed in Table 5.2. The highest

Table 5.2: *RMSE and standard deviation calculated between spectra* $R(n,\lambda)_{gt}$ *and* $R(n,\lambda)_{target}$ *for different light conditions.*

Lighting Condition	RMSE	Standard Deviation
H_50Wattx1	0.023	0.012
H_400Wattx1	0.022	0.010
G_315Wattx1	0.032	0.020
G_560lux1	0.023	0.012
L_50Wattx1	0.121	0.064
CFL_23Wattx1	0.176	0.083

radiometric inaccuracy is found in the data recorded under CFL_23Wattx1 and L_50Wattx1, with RMSE values of 0.176 and 0.121, and standard deviation of 0.083 and 0.064 respectively.

CFL_23Wattx1 and L_50Wattx1 are the two lighting conditions with the highest spectral inaccuracy and standard deviation. A high standard deviation implies that the data is less reliable. To look into this further, $R(n,\lambda)_{gt}$ and $R(n,\lambda)_{target}$ were plotted for all colour patches under the conditions CFL_23Wattx1 and L_50Wattx1. Consider the example of 21-Neutral 6.5 patch, as neutral patch reflects almost same energy in all range of EM, as shown in Figure 5.6.

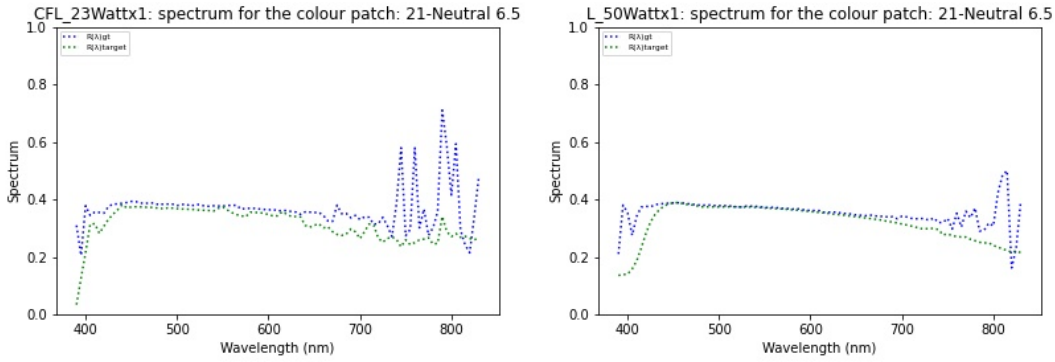

Figure 5.6: *The* $R(n,\lambda)_{gt}$ *(blue dotted line) and* $R(n,\lambda)_{target}$ *(green dotted line) acquired for 21-Neutral 6.5 under L_50Wattx1 and CFL_23Wattx1. The acquisition is performed under the same conditions but with two different light sources, demonstrating the effects of light source on the spectral reflectance of the patch. The noise in the ground truth data is considerably higher than* $R(n,\lambda)_{target}$*, which led us to conduct experimental study (explained in details in section 5.3).*

The 21-Neutral color patch is captured in the same conditions (acquisition

setup, position, etc.), by the same devices, but under different lighting conditions, i.e. CFL_23Wattx1 and L_50Wattx1. The two spectra in both plots of the image are different at the higher and bottom ends of the EM, as seen in the image. The two spectra obtained for each of these lighting circumstances contain noise or considerable spectral fluctuation, which can be caused by the light source's spectral power distribution. If the SPD of CFL_23Wattx1 and L_50Wattx1 is to be considered (see fig 4.7), CFL_23Wattx1 has a power distribution between the range of approx. 410 nm - 750 nm, there is no power before 400 nm and after 800 nm. Additionally, SPD of L_50Wattx1 has only one peak around 450 nm. On the other hand, SPD of CFL_23Wattx1 multiple peaks, however this light source has the power distribution between the range of 400 nm - 750 nm, it also has very less to no power outside this range. Since the signal to noise ratio is low in some regions of EM, the resultant spectrum contains noise. It demonstrates the importance of using a light source with sufficient power throughout the range of EM. Similar results are observed in the cases of other color patches. Because the presence of noise may have compromised the accuracy of the individual colour patches, the data from these two light sources are excluded from the following results analysis.

For the case of H_50Wattx1, H_400Wattx1, G_315Wattx1 and G_560lux1, consider the example of the same colour patch i.e. 21-Neutral 6.5, as shown in Figure 5.7. Figure 5.7 shows that the two spectras $R(n,\lambda)_{gt}$ and $R(n,\lambda)_{target}$ captured for each lighting condition are smoother and have no noise. They are also very well aligned. Taking the SPD of the light source into consideration, the halogen light sources i.e. H_50Wattx1, H_400Wattx1 have significantly less power in the lower end of the EM (see Figure 4.5), as compared to the HID MH light sources, (see Figure 4.6). It can be seen in the Figure 5.7 that the two spectra ($R(n,\lambda)_{gt}$ and $R(n,\lambda)_{target}$) differ slightly in the lower end of the EM, as compared to the two spectra captured under the lighting conditions of HID MH, in which the spectral distributions align perfectly. In comparison to the halogen light sources (i.e. H_50Wattx1 and H_400Wattx1), the G_315Wattx1 and G_560lux1 have greater radiometric differences.

The RMSE of individual colour patches is referred to as rmse_individual ($rmse_i$) Figure 5.8 shows the $rmse_i$ values for all the colour patches for all lighting conditions. Additionally, the colour patches with the highest and lowest RMSE values for these conditions are given in Table 5.3. The colour patch 19-white appears to have the highest $rmse_i$ value for the three light conditions, i.e., H_50Wattx1, H_400Wattx1, and G_315Wattx1, but for the case of G_560lux1, the RMSE decreases. The reason could be because the white patch in MacbethCC is located on the last row and first column, which is on the left side of the scene. The position of the light sources in the scene is also on the left side, and in these three light conditions, the light is pointing directly at the object. However, in the case of

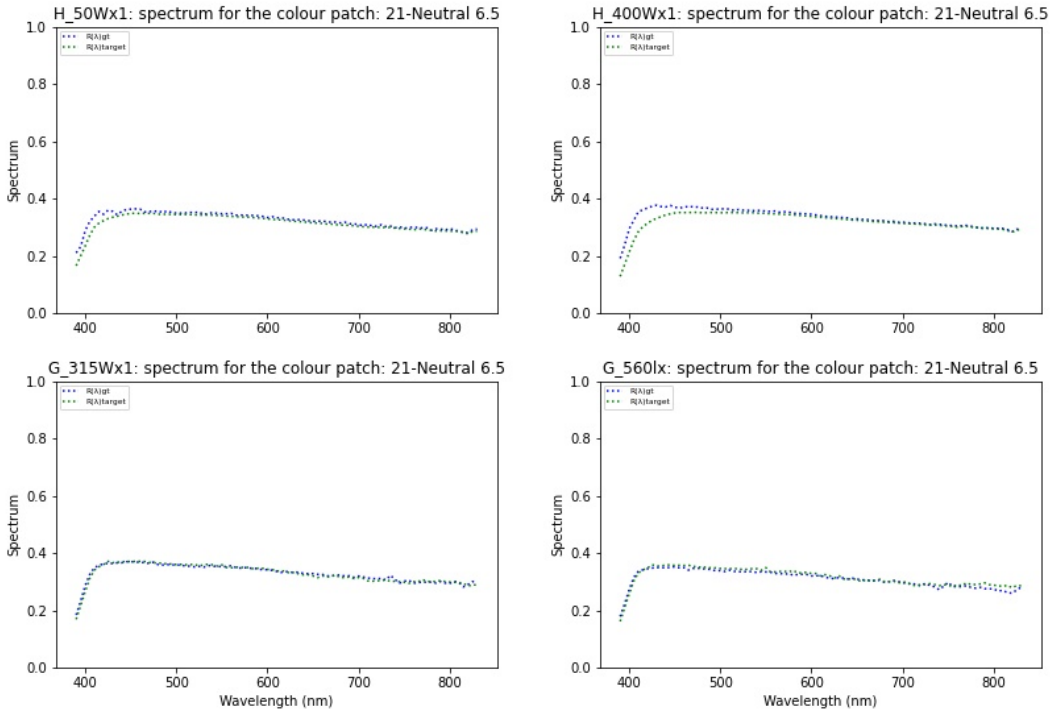

Figure 5.7: *The $R(n,\lambda)_{gt}$ and $R(n,\lambda)_{target}$captured under H_50Wattx1, H_400Wattx1, G_315Wattx1 and G_560lux1. In comparison to the earlier cases of L_50Wattx1 and CFL_23Wattx1, the spectras are smooth and properly aligned. It can be seen the $R(n,\lambda)_{gt}$ and $R(n,\lambda)_{target}$ are more accurate in the case of G_315Wattx1 and G_560lux1, as compared to H_50Wattx1, H_400Wattx1.*

Table 5.3: *Colour patches with lowest and highest RMSE values in different lighting conditions*

	H_50Wattx1	H_400Wattx1	G_315Wattx1	G_560lux1
Highest RMSE	19-White (0.069)	19-White (0.043)	19-White (0.079)	12-Orange yellow (0.046)
2nd Highest RMSE	16-Yellow (0.029)	22-Neutral 5 (0.042)	16-Yellow (0.054)	16-Yellow (0.043)
Lower RMSE	22-Neutral 5 (0.005)	23-Neutral (0.002)	4-Foliage (0.004)	4-Foliage (0.003)
2nd lowest RMSE	23-Neutral (0.01)	13-Blue (0.007)	23-Neutral (0.005)	1-Dark skin (0.004)

G_560lux1, the light source is not facing the object directly; instead, the object is illuminated by the means of indirect ambient illumination, which may reduce errors caused by the white patch's inter-reflection.

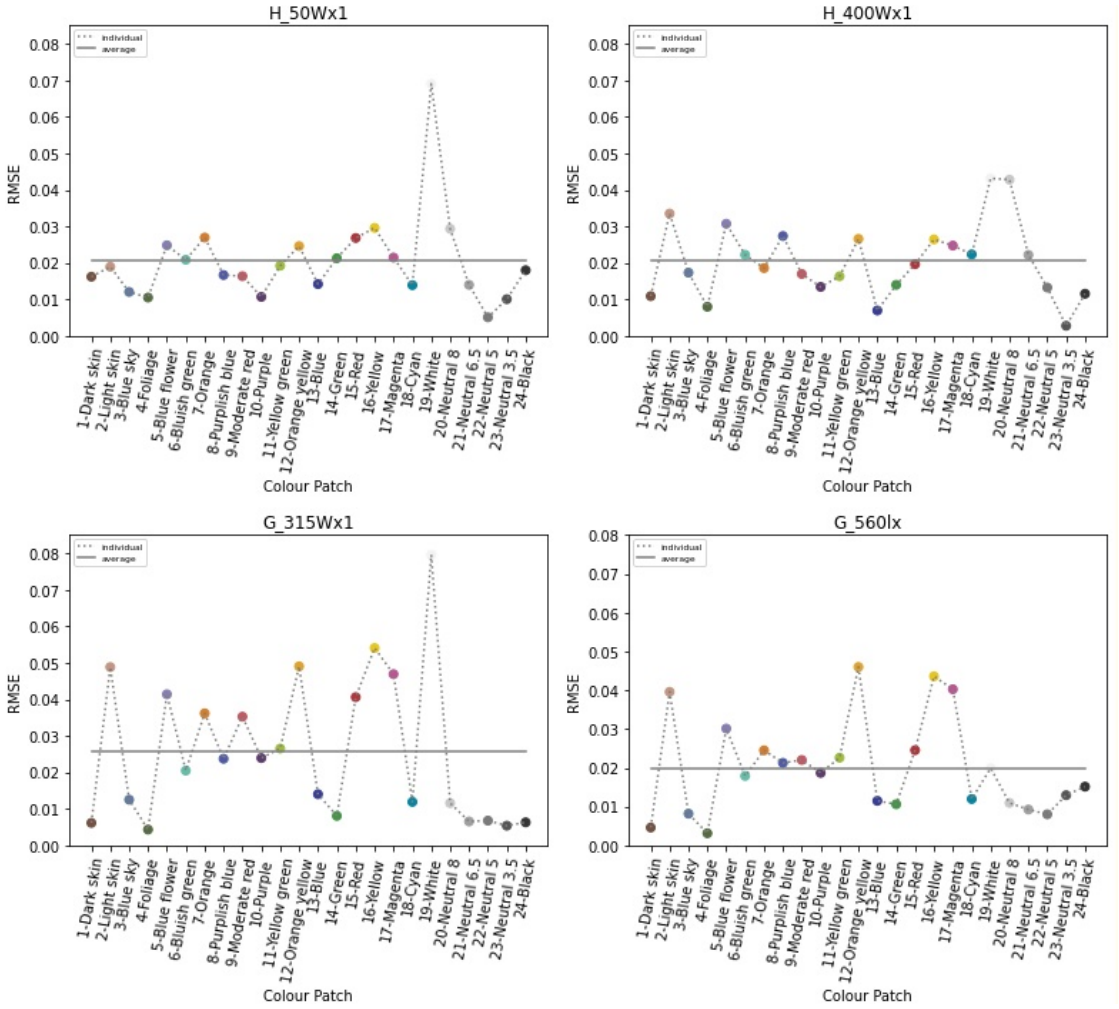

Figure 5.8: *Overall summary of RMSE for each colour patch of MacbethCC under H_50Wattx1, H_400Wattx1, G_315Wattx1 and G_560lux1 lighting conditions*

Besides 19-White, 16-Yellow appears to have a high RMSE value for three light conditions i.e. H_50Wattx1,G_315Wattx1 and G_560lux1. If we compare the overall radiometric accuracy, halogen light sources perform better as compared to the MH grow lights. H_50Wattx1, H_400Wattx1 appear to be more accurate than G_315Wattx1 and G_560lux1 despite the same average RMSE (see Table 5.2). The colours with the neutral tone (for example, 22-Neutral 5, 23-Neutral) demonstrate good radiometric accuracy for the H_50Wattx1, H_400Wattx1. But

when it comes to G_315Wattx1 and G_560lux1, they show good radiometric accuracy for the colours like 3-Blue Sky, 4-Foliage, and 13-Blue. This is caused by the difference in spectral power of the two light sources. G_315Wattx1 and G_560lux1 have the maximum energy in the lower region of the spectrum. Hence, the colours in those regions show good accuracy.

5.1.3.2 Colorimetric accuracy

Colorimetric accuracy calculated between $R(n,\lambda)_{gt}$ and $R(n,\lambda)_{target}$ for different light conditions is shown in Table 5.4. The average *JNDu'v'* for H_50Wattx1, H_400Wattx1,G_315Wattx1, G_560lux1 is 1.969, 2.133,1.158 and 1.297 respectively for illuminant E (Figure 5.9) and 1.986, 2.147,1.157 and 1.271 respectively for illuminant D65 (Since the Chromaticity uncertainty of a Jeti device is given up to 3 decimal points, values are taken up to 3 decimal points). While the ΔE^*ab units for illuminant E are 3.308, 3.728, 1.628, and 1.547, respectively, the ΔE^*ab units for illuminant D65 are 3.211, 3.622, 1.618, and 1.541. The mean JNDu'v' and ΔE^*ab values for both illuminant E and illuminant D65 indicate that that G_315Wattx1, G_560lux1 contains highest colorimetric accuracy as compared to the H_400Wattx1 and H_50Wattx1.

Table 5.4: *Average JNDu'v' and* ΔE*ab *under illuminant E and D65 for H_50Wattx1, H_400Wattx1, G_315Wattx1 and G_560lux1*

	JNDu'v' (illuminant E)	JNDu'v' (illuminant D65)	ΔE^*ab (illuminant E)	ΔE^*ab (illuminant D65)
H_50Wattx1	1.969	1.986	3.308	3.211
H_400Wattx1	2.133	2.147	3.728	3.622
G_315Wattx1	1.158	1.157	1.628	1.618
G_560lux1	1.297	1.271	1.547	1.541

As a reference, previous studies [31][74] suggested that when two uniform samples are viewed side by side, CIELAB ΔE^*ab of 1 unit corresponds to a just noticeable difference. However, in the complex images, the error of up to 6 ΔE^*ab units is not detected [47]. Therefore, it can be said that by considering the average mean, it is possible to attain reasonably good colour repeatability in any of these four illumination conditions. The average mean, on the other hand, does not indicate the individual colour differences. In various types of light, it's possible that some colours will have a comparatively large degree of colour inaccuracy. The overall summary of the ΔE^*ab and *JNDu'v'* for all the lighting conditions is shown

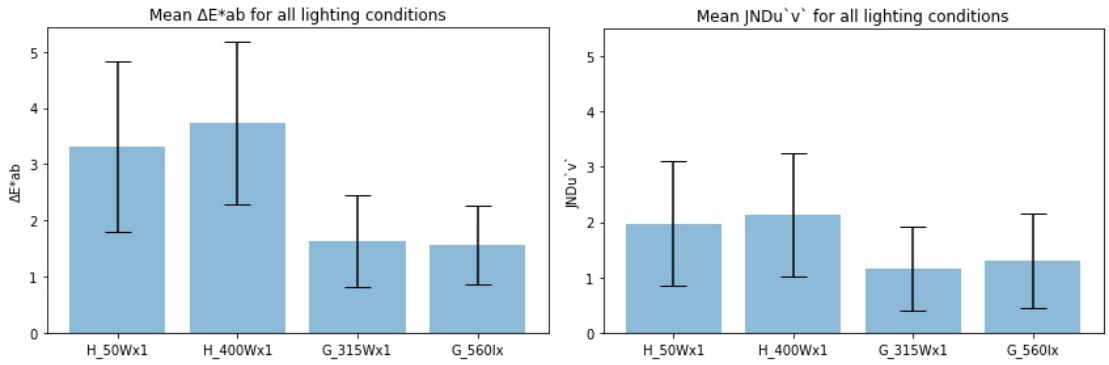

Figure 5.9: *Average mean and standard deviation* ΔE*ab *and JNDu'v' under illuminant E.*

in Figure 5.10 visualised using box plot. The ΔE^*ab and *JNDu'v'* for individual colours is shown in Figure 5.11.

Colour patches with the highest ΔE^*ab and *JNDu'v'*

In order to identify colours with the highest ΔE^*ab and *JNDu'v'*, heatmaps are plotted for both ΔE^*ab and *JNDu'v'* for CIE illuminant E and D65. The heat maps in Figure 5.12 indicate colour patches that exhibit higher, lower and intermediate ΔE^*ab and *JNDu'v'* values. Colour patches 13-Blue and 15-Red have high *JNDu'v'* values for all the lighting conditions. However, 24-black is having high *JNDu'v'* under illumination H_50Wattx1, H_400Wattx1, and G_560lux1. On the other hand, in the case of ΔE^*ab, 7-Orange and 15-Red show the highest colour differences in all lighting conditions. Summarized, that same colour patches (i.e. 24-black, 13-Blue, 15-Red and 7-Orange) are exhibiting the highest ΔE^*ab and *JNDu'v'* under all lighting conditions. Their numerical values, however, vary depending on the illumination condition. For instance colour patch 15-Red is considered as having high colour difference in all lighting conditions, yet the *JNDu'v'* value varies between 3.484 for H_50Wattx1, 4.301 for H_400Wattx1, 2.235 for G_315Wattx1 and 2.504 for G_560lux1. Table 5.5 contains the ΔE^*ab and *JNDu'v'* values for 24-black, 13-Blue, 15-Red and 7-Orange colour patches.

The colours 13-Blue and 15-Red are found at lower and higher wavelengths of the electromagnetic spectrum, respectively. The highest colour differences identified for such colours may be because of the low sensitivity of the sensor in the lower and higher wavelengths or the resultant of the stray light interference. The effect of stray light is investigated in the next experimental study.

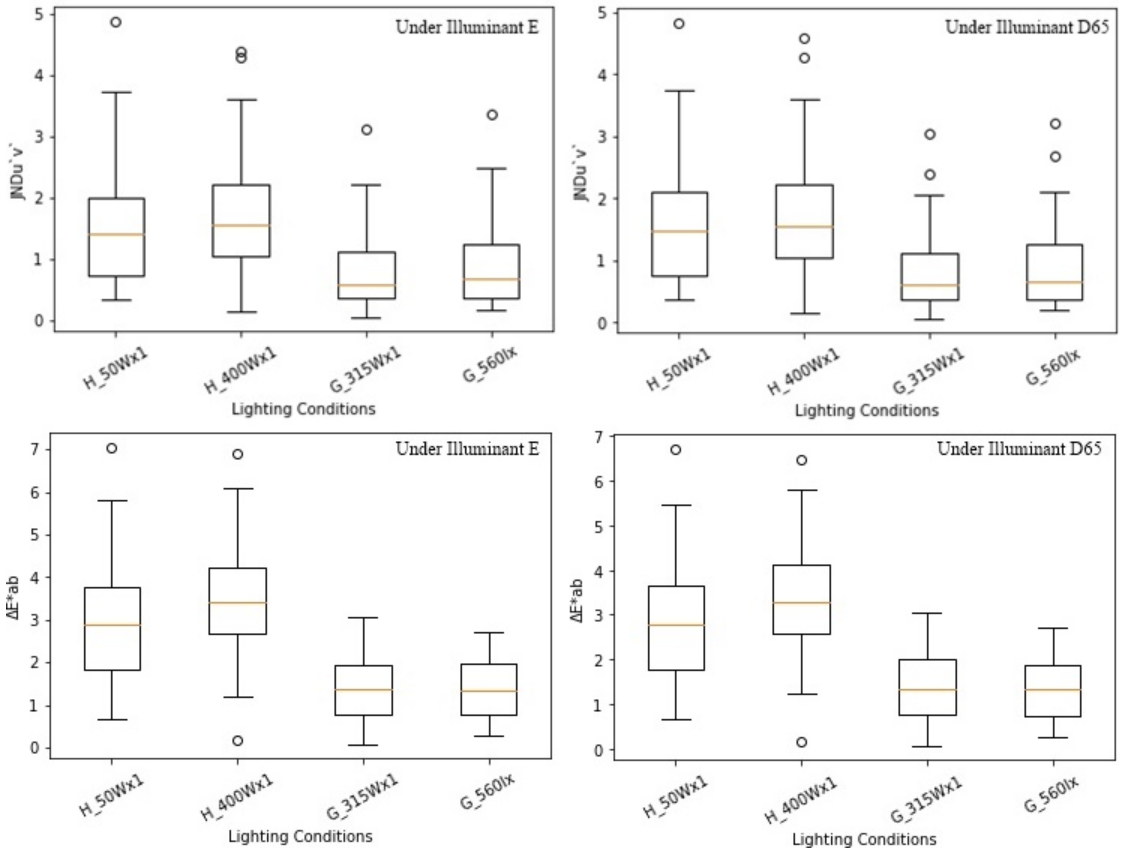

Figure 5.10: *The distribution of* ΔE*ab *and JNDu'v' under illuminant E and illuminant D65 for H_50Wattx1, H_400Wattx1, G_315Wattx1 and G_560lux1. It is shown that G_315Wattx1 and G_560lux1 are relatively more colorimetric accurate as compared to the H_400Wattx1 and H_50Wattx1.*

5.2 Experimental test 2: Analysing the effect of stray light on colorimetric accuracy

In light-surface interaction, surface scattering properties may cause some portion of the light entering the imaging system to be directed to the different locations. This mis-directed light is called stray light [14]. Stray light has many disadvantages. It can reduce the contrast and details of an image while also affecting colorimetric and photometric accuracy [12] [36] . For example, in a scenario with objects with bright colours surrounded by a vast background of a different colour, background can cause the measured colour of the object to be substantially different than its original colour [12]. Each colour in our test object, MacbethCC, is surrounded by a group of different colours; assuming that the stray light falling upon the picture

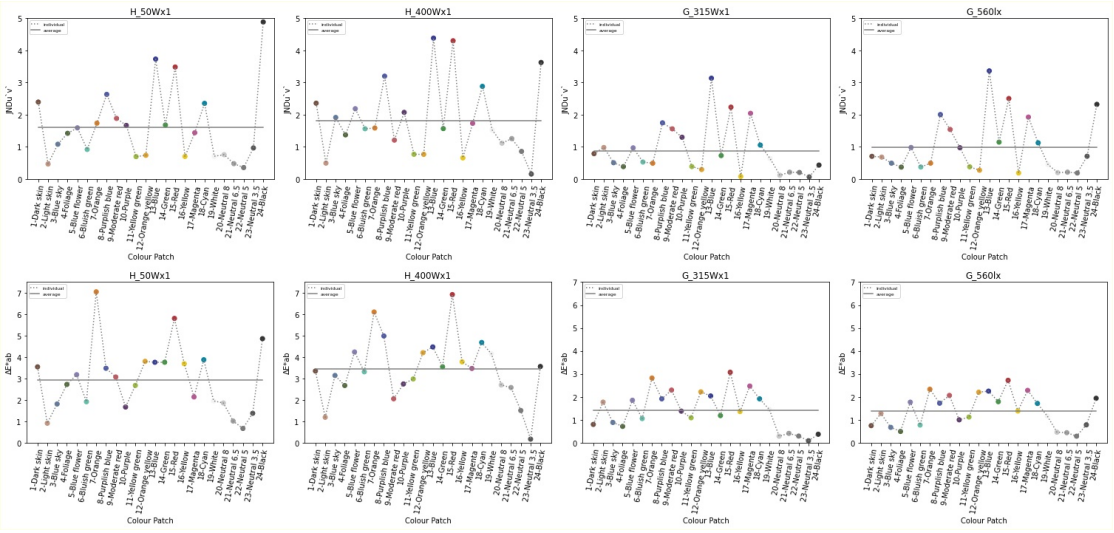

Figure 5.11: *JNDu'v' (top) and ΔE*ab (bottom) for all colour patches under illuminant E for* H_50Wattx1*, H_400Wattx1, G_315Wattx1 and G_560lux1.*

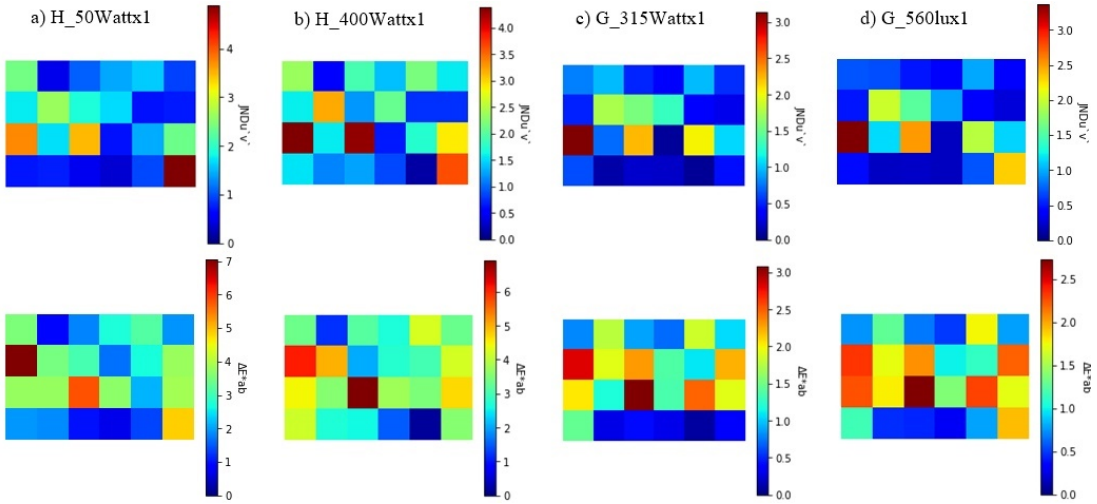

Figure 5.12: *Highest and lowest JNDu'v' and* ΔE*ab *and for all colour patches under illuminant E*

plane originated from the test target, it could be contributing to the colorimetric accuracy of the colour patches to some extent.

Another possible source of stray light is lateral diffusion. Lateral diffusion causes stray light in the sample to go to areas not visible to the instrument detectors [36]. This can be a problem with the SpecimIQ because it is a line scanner, which means it scans the data one line at a time, which may produce lateral diffusion error due

Table 5.5: *Colorimetric differences JNDuv and ΔEab between $R(n,\lambda)_{gt}$ and $R(n,\lambda)$ target under illuminant E.*

Lighting condition		7-Orange	13-Blue	15-Red	24-Black
H_50Wattx1	*JNDu'v'*	1.737	3.732	3.484	4.886
H_400Wattx1		1.586	4.38	4.301	3.626
G_315Wattx1		0.490	3.137	2.235	0.433
G_560lux1		0.492	3.364	2.504	2.322
H_50Wattx1	*ΔE*ab*	7.045	3.756	5.805	4.858
H_400Wattx1		6.103	4.473	6.916	3.560
G_315Wattx1		2.819	2.039	3.071	0.371
G_560lux1		2.412	2.202	2.543	2.120

to scattering.

Nonetheless, we conducted experimental tests employing lighting condition G_560lux1 using the same experimental setup to investigate the accuracy of the colours affected by the surrounding colours. We picked G_560lux1 lighting conditions for the experiment because it demonstrated comparatively better colorimetric accuracy than the halogen light sources, H_50Wattx1, and H_400Wattx1. It is also a better option than G_315Wattx1, which provides illumination of 1600 lx and is less practical under museum conditions.We acquired the ground truth data $R(n,\lambda)_{gt}$ and target data $R(n,\lambda)_{target}$ of the test object in 6 different cases defined below. The summary of the test cases are given in Table 5.6.

Table 5.6: *A description of the test cases investigated in the study*

S.No	Test Case	Description
1.	G_560lux1	A test object is in its original position. (See Figure 5.13 |1|)
2.	G_560lux1_90°left	A test object is rotated 90° to the left of its original position. (See Figure 5.13 |2|)
3.	G_560lux1_90°right	A test object is rotated 90° to the right of its original position. (See Figure 5.13 |3|)
4.	G_560lux1_3rows	The test object is in its original position, and the fourth row of the test object, which contains neutral colours, is hidden from view. (See Figure 5.13 4)
5.	G_560lux1_90°left_3rows	The test object has been rotated 90° to the left of its original position, and the top three rows have been hidden from the view. (See Figure 5.13 |5|)
6.	G_560lux1_90°right_3rows	The test object has been rotated 90° to the right of its original position, and the top three rows have been hidden from the view. (See Figure 5.13 |6|)
7.	G_560lux1_3col_left	The test object is in its original position, and the three columns to the right are hidden from the view (See Figure 5.13 |7|)
8.	G_560lux1_3col_right	The test object is in its original position, and the three columns to the left are hidden from the view (See Figure 5.13 |8|)

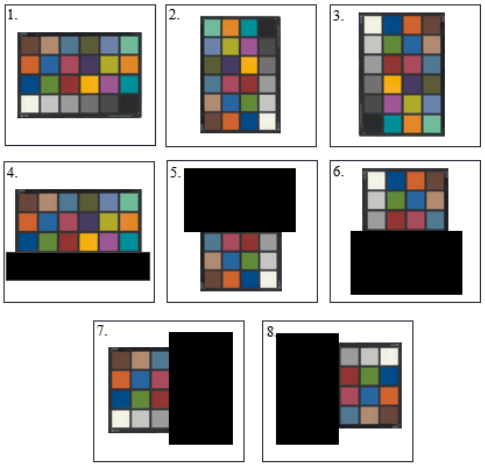

Figure 5.13: *A visual representations of the test cases investigated in the experimental study involving stray light. 1) G_560lux1: MacbethCC is at its normal position, 2) G_560lux1_90°left: MacbethCC is rotated 90° to the left of its normal position, 3) G_560lux1_90°right: MacbethCC is rotated 90° to the right of its normal position, 4) G_560lux1_3rows: Last row of MacbethCC is hidden, 5) G_560lux1_90°left_3rows 6) G_560lux1_90°right_3rows 7) G_560lux1_3col_left and 8) G_560lux1_3col_right*

5.2.1 Selection of test cases

- G_560lux1

When the SpecmIQ captures a test object, it scans it from right to left, which means the line must read four colours at once in a 4 square fixed arrangement. For example, 13-Blue will always have 1-Dark skin, 7-Orange on top, and 24-white on the bottom (see Figure 5.13 (1)) . To study the effect of neighbouring colours on colorimetric accuracy, we formulated the following cases by changing the input to the line scanner.

- G_560lux1_90°left & G_560lux1_90°right

This refers to the test case in which the test object is rotated 90° to the left (see Figure 5.13 (2)) and 90° to the right (see figure 5.13 (3)) of its original position, respectively, such that line scans read six colour patches at once, and the colour arrangement is also changed. For example, 13-Blue in the case of G_560lux1_90°left is on the bottom and 5 distinct colours on top and the color

patches scanned together with it are 14-Green, 15-Red, 16-Yellow, 17-Magenta and 18-Cyan.

- G_560lux1_3rows

This refers to the case when the test object is in its original position and the fourth row of the test object, which comprises neutral colours, is hidden from view using a black card sheet (see Figure 5.13 (4)).

- G_560lux1_90°left_3rows & G_560lux1_90°right_3rows

This refers to the case in which the test object has been rotated 90 degrees to the left (see Figure 5.13 (5)) and 90 degrees to the right (see Figure 5.13 (6)) from its original position, and the top three rows have been concealed from view using the black card sheet. The benefit of doing this is that, in these two test cases, 15-Red (which is identified as one of the in-accurate one in previous study, section 5.1.3.2) does not have bright yellow as a surrounding colour.

- G_560lux1_3col_left & G_560lux1_3col_right

The test object is in its original position, and the three columns to the right (see Figure 5.13 (7)) and left (see Figure 5.13 (8)) are covered using black card sheet and are concealed from view. However the colour arrangement as read by the scanner has been changed.

5.2.2 Results & Discussion

For each test case, the values of *JNDu'v'* and ΔE^*ab values are calculated between $R(n,\lambda)_{gt}$ and $R(n,\lambda)_{target}$. Results are presented using heat maps which gives the direct overview of the colour patches with highest colorimetric differences (i.e. highest *JNDu'v'* and ΔE^*ab values). In our previous experimental studies (see section 5.1.3.2), it was found that the colour patches 13-Blue, 15-red and 24-black had the highest *JNDu'v'*, and 7-orange, 15-red had the highest ΔE^*ab for both illuminant E and illuminant D65.

In order to discuss the colorimetric results of the test cases discussed above, in terms of JNDu'v' and E*ab, we will use the examples of 13-Blue, 15-Red and 7-Orange respectively, as they appear to be problematic in terms of colorimetric accuracy when compared to other colour patches of MacbethCC. Table 5.7 contains the JNDu'v' values of 13-Blue and 15-Red.

A 13-Blue colour patch, In the case of G_560lux1, has a JNDu 'v' of 3.364, which is reduced to JNDu'v' of 3.179 in the case G_560lux1_90°left, which further

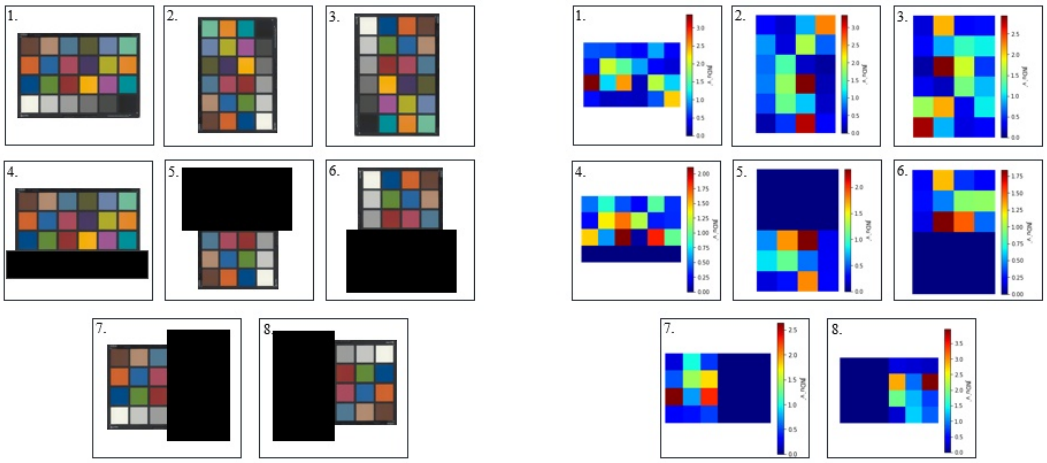

Figure 5.14: *On the right, heatmaps are plotted that show the highest and lowest JNDu'v' for all color patches of the different conditions shown on the left.*

Table 5.7: *JNDu'v' values of 13-Blue and 15-Red, and* ΔE*ab *values of 12-Orange calculated for different test cases*

S.No	Test Case	JNDu'v' (13-Blue)	JNDu'v' (15-Red)	ΔE^*ab (7-Orange)
1.	G_560lux1	3.364	2.504	3.397
2.	G_560lux1_90°left	3.179	3.349	2.831
3.	G_560lux1_90°right	2.101	2.938	2.387
4.	G_560lux1_3rows	1.460	2.113	1.820
5.	G_560lux1_90°left_3rows	1.787	2.346	2.060
6.	G_560lux1_90°right_3rows	1.305	1.840	2.069
7.	G_560lux1_3col_left	2.642	2.301	2.671
8.	G_560lux1_3col_right	3.959	2.882	3.397

reduces to JNDu'v' of 1.787 for the case of G_560lux1_90°left_3rows. According to our analysis, 13-Blue has 19-White at its bottom in G_560lux1 (see Figure 5.14(1)). 13-blue, on the other hand, does not have 19-White in G_560lux1 90°left (see Figure 5.14(2)); instead, it is positioned in the last row with various colored patches on top. Eliminating the 19-White from the view (i.e. input to the line scanner) might have reduced some extra flux which might be introducing some errors. However, having five colours on top, might have introduced some amount of flux, which is reduced further in the case of G_560lux1_90°left_3rows, which eliminates some

colours from the view (see Figure 5.14(5)). Similar trends in results are found in the case of G_560lux1_90°right and G_560lux1_90°right_3rows where *JNDu'v'* of 2.101 has reduced to 1.305. Comparing test case G_560lux1 (see Figure 5.14(1)) and G_560lux1_3rows (see Figure 5.14(4)) reveals that the JNDu 'v' of 13-blue has dropped to JNDu 'v' of 1.460, which suggests that 19-white may have been responsible for the stray light. Additionally, *JNDu'v'* of 2.642 and 3.959 in the case of G_560lux1_3col_left (see Figure 5.14(7)) and G_560lux1_3col_right (see Figure 5.14(8)) demonstrate the impact of having colours in various arrangements. The impact of the arrangement is probably caused by the position of color patches which is studied in experimental study 4 (Section 6.1).

The presence of 16-Yellow in the case of 15-Red has a similar effect to how 19-White affects 13-Blue. The *JNDu'v'* of 2.504 in the case of G_560lux1, in which 15-red is not in the same column as 16-yellow, (see Figure 5.14(1)) is increased to JNDu'v of 3.349 in the case of G_560lux1_90°left, where 16-Yellow is located at the top of 15-red (see Figure 5.14(2)). The value decreases to *JNDu'v'* of 2.346 in the case of G_560lux1_90°left_3rows, in which the 16-Yellow along with other colours are hidden from the scene (see Figure 5.14(5)). Similarly, JNDu'v' of 2.938 is reported for the case of G_560lux1_90°right (see Figure 5.14(3)), while for the case of G_560lux1_90°right_3rows (see Figure 5.14(6)), *JNDu'v'* of 1.840 is reported.

When computing the ΔE^*ab for all the cases, the colour patch 7-Orange (See Table 5.7) reached similar conclusions. The Figure 5.15 gives an overall summary of the results .

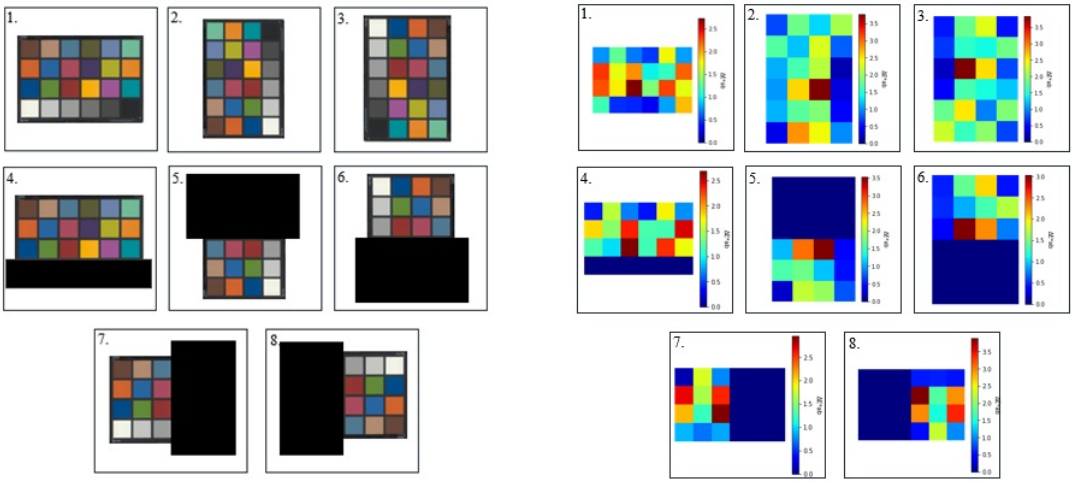

Figure 5.15: *On the right, heatmaps are plotted that show the highest and lowest* ΔE*ab *for all color patches of the different conditions listed on the left*

5.3 Experimental test 3: Characterization of JETI - specbos 1211 L using HunterLab Ultrascan® PRO

In this research investigation, a JETI- specbos 1211 L spectroradiometer is used to collect ground truth data $R(n,\lambda)_{gt}$. It was noticed that noise was captured in the acquired data($R(n,\lambda)_{gt}$) in two of the lighting condition cases, namely L_50Wattx1 and CFL_23Wattx1, particularly in the lower and upper wavelengths of the electromagnetic spectrum (See Figure 5.6). The noise in the ground truth data is significantly higher than $R(n,\lambda)_{target}$ (i.e. the data specimIQ data), which led us to conduct this experimental study to evaluate the difference in ground truth data acquired under different lighting conditions. For this investigation, we employed HunterLab UltaScan® Pro as a reference instrument (details of the device are given in section 3.4). The Spectral reflectance of colour patch $R(n,\lambda)_{hl}$ is measured within the spectral range of 350 nm - 1050 nm using the device's 0.5 inch diameter port and the mode "specular excluded, uv-included.

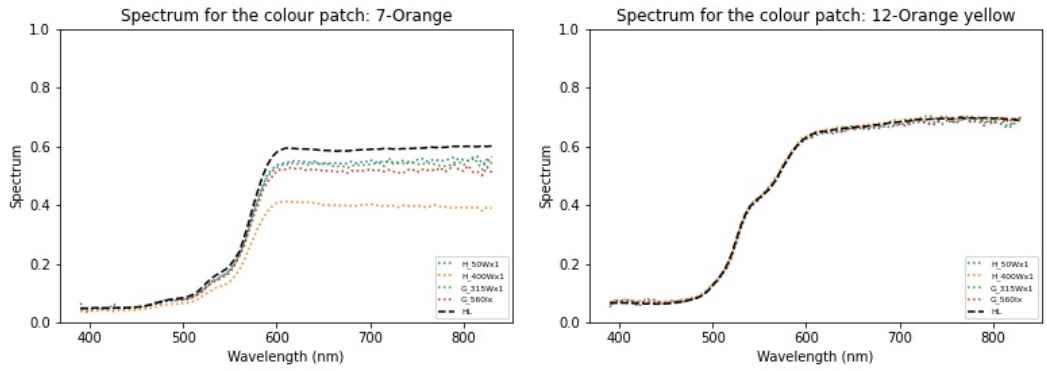

Figure 5.16: *The shown plots are the* $\mathrm{R(n,\lambda)_{gt}}$ *acquired for four different lighting conditions and* $R(n,\lambda)_{hl}$ *for 7-Orange and 12-Orange.*

When we compared $R(n,\lambda)_{hl}$ to the spectral reflectance recorded for the four lighting situations (i.e. $R(n,\lambda)_{gt}$), we discovered that the spectral reflectance colour patches on the right hand side columns of the view contain greater radiometric differences than the spectral reflectances on the left side columns (see Figure A.2 in appendix). When the data was visualised, two of the colour patches that attracted the most attention were 7-Orange and 12-Orange-Yellow (See Figure 5.16).

The Figure shows that, regardless of the fact that both colour patches are different shades of the same colour (orange) and have relatively similar spectral reflectance, they behave differently in both positions.The colour patch on the left

side (7-Orange) has clear visual radiometric differences as compared to the colour patch on the right side (12-Orange-Yellow).

To investigate this further, two orange colour paper samples (named as 7_Org and 12_Org) are used. These samples are made of the same material as the MacbethCC colour patches, and their hues are similar to those in the MacbethCC. The benefit of using these samples instead of entire MacbethCC is that any additional flux that may have entered the imaging optics due to the impact of neighbouring colours is now eliminated. During our earlier comparison of $R(n,\lambda)_{gt}$ (i.e. $R(n,\lambda)_{gt}$ under different lighting conditions) with $R(n,\lambda)_{hl}$, it was discovered that the H_400Wattx1 had the highest radiometric inaccuracy of the two spectral reflectance values.So we conducted the experiment under H_400Wattx1 on two different cases, namely case1 and case2.

In case1, spot measurements $(L_{sample}(n, \lambda))$ utilising JETI - specbos 1211 L are taken at location 7 (exactly the position of the 7th sample of the MacbethCC). Data is collected in such a way that there is just one sample present in a scene at a time. Data for both the samples and the white reference (white_kapa) is acquired (see section 4.2.2 for use of white reference in data conversion). Case2 is similar to case1, except that the data is acquired at location 12 (exactly the position of the 12th sample of the MacbethCC.

One difference between the two devices, JETI - specbos 1211 L and HunterLab Ultrascan® PRO, is that HunterLab Ultrascan acquires spectral reflectance directly from the sample, whereas JETI acquires spectral radiance of sample, which is then converted to spectral reflectance using the irradiance measured with the white reference sheet. We incorporate two extra white references in the study, in addition to the kapa_white reference, to see the role of white reference in measurements. We measured 5 samples in total (2 colour samples with orange hues and 3 white references). Table 5.8 summarises the names of the samples.

Table 5.8: *Description of the samples used in this experimental study*

S.No	Sample	Description
1.	7_Org	Paper sample in the colour orange, similar to MacbethCC's colour 7-orange.
2.	12_Org	Paper sample in the colour orange, similar to MacbethCC's colour 7-orange
3.	white_kapa	Same white sheet used in all previous experiments
4.	white_card	A sheet of white card paper having slightly rough matt surface (see Figure 5.17)
5.	white_mcc	A white paper sheet with the same surface type as MacbethCC (see Figure 5.17)

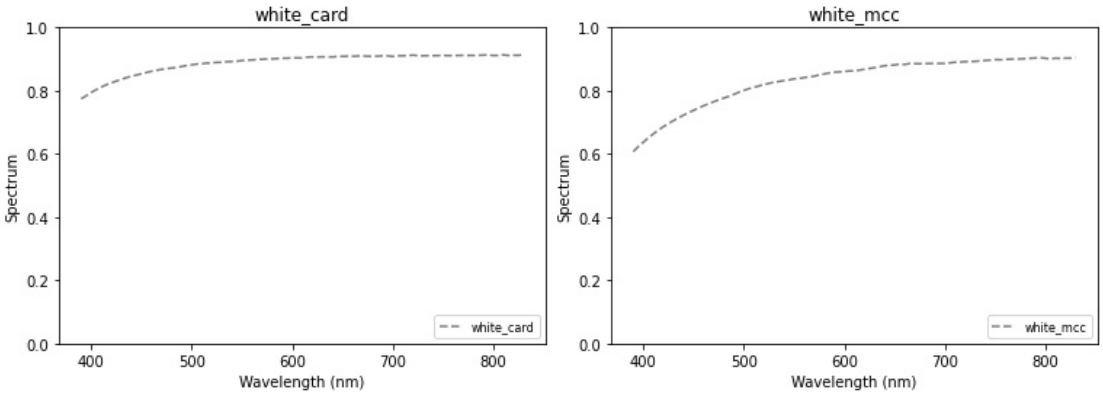

Figure 5.17: *Spectral reflectance R(λ) of the reference white_card and white_mcc*

5.3.1 Results & Discussion

Figure 5.18 illustrates the results of case1 and case2. The Figure shows that the radiometric differences are lower in case2 as compared to case1. Table 5.9 displays the RMSE values obtained between $R(n,\lambda)_{gt}$ and $R(n,\lambda)_{hl}$ for both cases 1 and 2. To discuss the results, consider the example of 7_Org, RMSE is reduced from 0.099 to 0.019 in combination with white_kapa as reference sample. white_kapa. The only difference between these two is the position of the samples. A similar trend is seen in the cases of white_card and white_mcc. Overall, the RMSE value is decreased when samples are placed at position-12 as compared to position-7. When the difference in RMSE values is studied in relation to the difference in white reference, it can be seen that the RMSE is lowest (0.030 and 0.006) when white_mcc is used as a white reference for both the case1 and case2 respectively. Furthermore, when white_card is used as a white reference, there is no significant improvement from case1 (0.04) to case2 (0.03). A similar pattern of results was observed for the sample 12-Org.

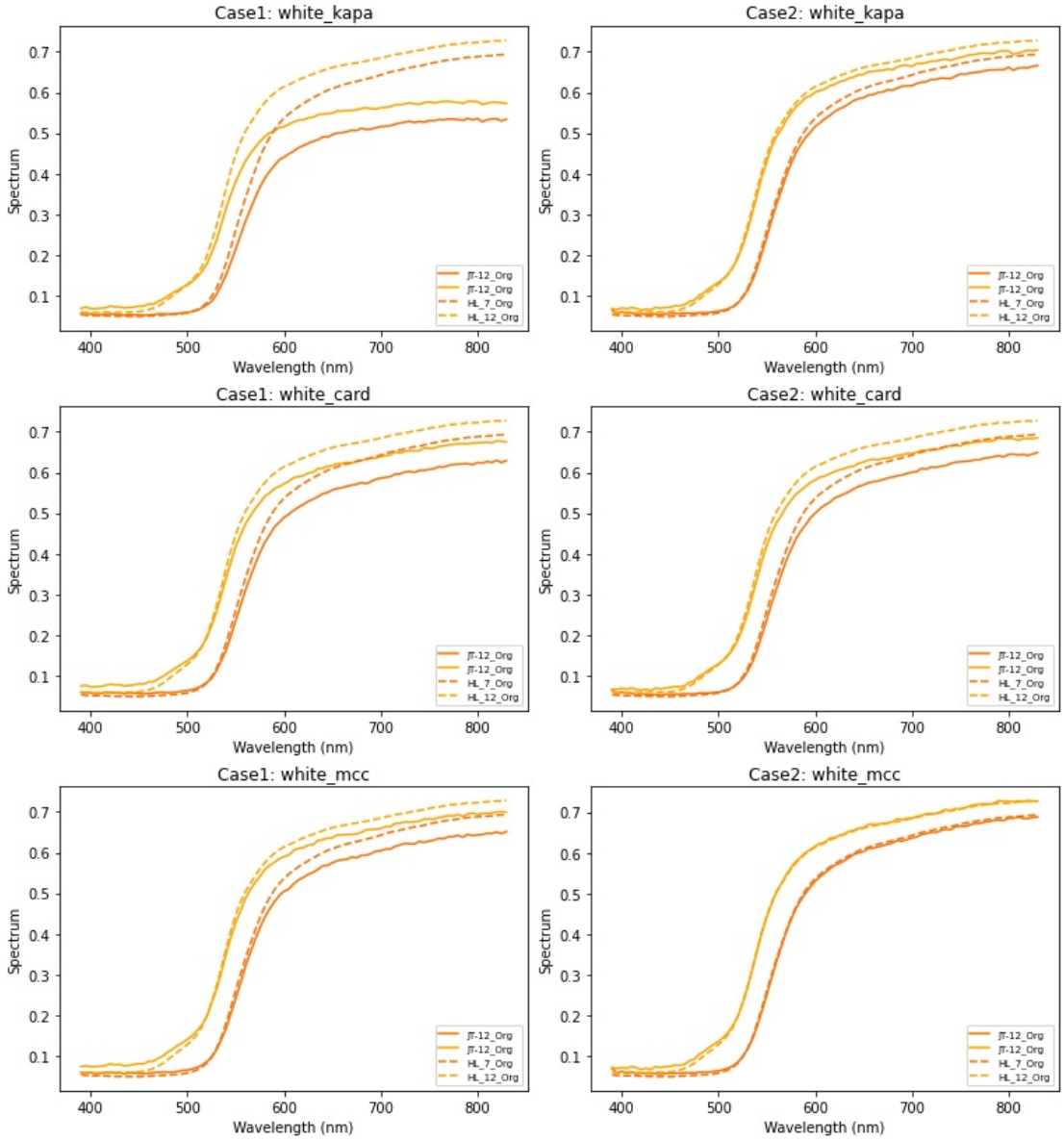

Figure 5.18: *Spectral reflectance $R(n,\lambda)_{gt}$ and $R(n,\lambda)_{hl}$ for two different cases*

Table 5.9: *RMSE between* $R(n,\lambda)_{gt}$ *and* $R(n,\lambda)_{hl}$ *for both the case1 and case2*

	Case1		Case2	
	7_Org	12_Org	7_Org	12_Org
white_kapa	0.099	0.097	0.019	0.015
white_card	0.044	0.037	0.033	0.030
white_mcc	0.030	0.021	0.006	0.006

6 Experimental tests, results and discussion (part 2)

In a prior experiment, we found that the same samples have varying radiometric accuracy when placed in different locations in the scene. When samples from case1 are compared to samples from case2, the differences are apparent. As previously stated, case1 is in the 7-position, which is on the left side. Our experimental setup has always had the light source on the left side. It indicates that light illuminating the samples in the scene, interacting with the samples, and reaching the imaging optics may differ in both cases, leading to radiometric errors.

All the samples that have been investigated so far have a matt surface. When light strikes the matt surface, it reflects in all directions. If the device fails to collect all of the light reflected off the samples (for example, due to the illumination geometry of the acquisition setup or light propagation through the sample) , the measured reflectance will be inaccurate [69].

Another crucial difference between the two devices JETI - specbos 1211 L and HunterLab Ultrascan® PRO is the adopted illumination geometry. The HunterLab Ultrascan® PRO acquires data using diffuse d/8° geometry, and the light source installed within it to measure reflectance is a pulsed Xenon lamp that is calibrated and controlled in the UV region. Our measurement setup works on a different illumination geometry. To minimise this difference between the two devices's acquisitions setups, we modified our measurement setup to 45/0° geometry.

Experimental setup

The test object, i.e., the MacbethCC is placed in the centre of the table at a distance of approx. 1 m from the ground, and the whole surroundings of the object are provided with a sufficient amount of illumination. The illumination is provided by a light source located 1.2 m from the target and aimed straight at the test object. The measurement device (i.e. the specimIQ camera and Jeti spectroradiometer) is mounted on a tripod 1.0 m from the test object and 1.0 m above the ground.

Figure 6.1 represents the experimental set-up. In summary, the setup's objects are 1.2 m apart from each other and approx 1 m above the ground.

6.1 Experimental study 4: Effects of different illumination geometry on data accuracy

In the same approach as in the previous study, we performed the data acquisitions ($R(n,\lambda)_{gt}$) on the samples 7-Org, 12-Org, and the white references white kapa, white card, and white mcc in the current experimental setup. The results are shown in Figure 6.2 while RMSE values are given in Table 6.1.

When the RMSE values of both examples are compared to the RMSE values calculated in the previous case (shown in Table 5.9), they are much lower. The significant improvement in findings highlights the importance of proper geometry in measurement acquisition procedures.

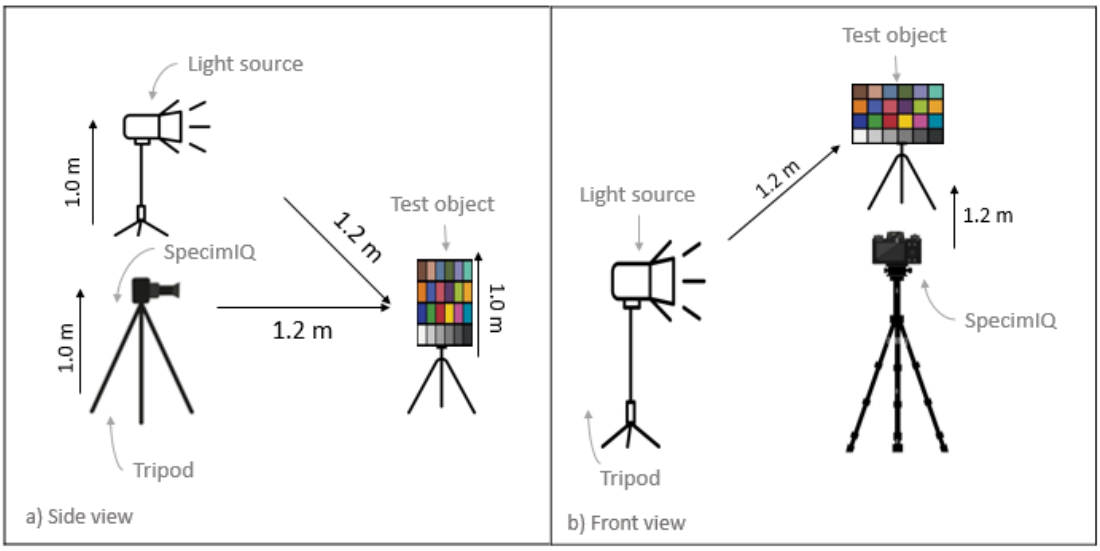

Figure 6.1: *Semantic representation of the acquisition setup with 45/0° viewing geometry*

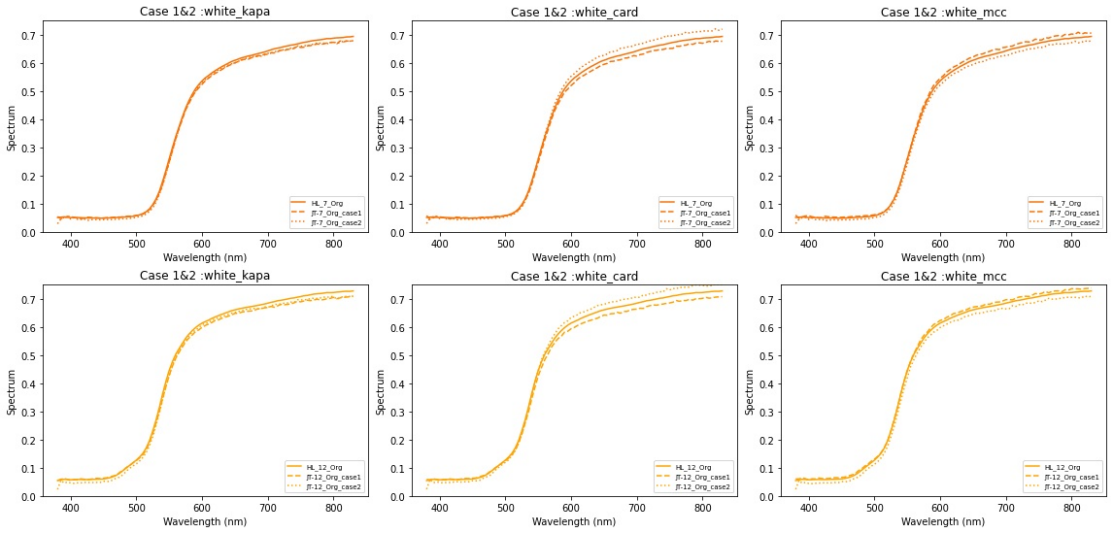

Figure 6.2: *Spectral reflectance $R(n,\lambda)_{gt}$ and $\mathrm{R(n,\lambda)_{hl}}$ for two different cases with different white reference i.e. white_kapa,white_card and white_mcc*

Table 6.1: *RMSE between $R(n,\lambda)_{gt}$ and $\mathrm{R(n,\lambda)_{hl}}$ for both the case1 and case2*

	Case1		Case2	
	7_Org	12_Org	7_Org	12_Org
white_kapa	0.010	0.014	0.009	0.013
white_card	0.012	0.017	0.017	0.018
white_mcc	0.010	0.008	0.013	0.017

6.2 Experimental study 5: Effects of different white reference and test sample materials on data accuracy

The standard white reference is a white sheet with maximum reflectance value. It is used in the data acquisitions, to estimate the illuminance of the scene, which in turn is used to calculate the reflectance of the acquired scene. It holds a significant importance as the acquired data may be altered by the type of white reference used. Hence, it is important to select the appropriate type in order to have an accurate representation of the acquired data. In our previous experimental study

(experimental study 4, described in 6.1), we have seen that the accuracy of the samples were affected by the white reference used. Both samples 7_Org and 12_Org were found to be most accurate when white_mcc is used as a white reference. The material of the white_mcc is of the same type as that of the samples, which implies that when the white reference of the same kind as the sample is employed, the data accuracy may be improved.

To evaluate how much the white reference contributes to the accuracy of the data and whether it is necessary to use the same material for white reference, we employed NCS gloss scale as test and reference samples of the study.

NCS gloss scale

The NCS gloss scale [58] is a collection of various grayscale colours (i.e. white, light gray, mid-gray, and black colour samples) combined with various gloss levels. The collection contains seven even gloss levels (from full matt to full gloss) for every of the 4 grayscale colours. The gloss level includes "full matt (gloss level 2), matt (gloss level 6), semi-matt (gloss level 12), Satin (gloss level 30), Semi-glossy (gloss level 50), Glossy (gloss level 75) and Full gloss (gloss level 95) [58]". We utilized five gray samples with varying gloss levels and five white samples as white references. Table 6.2 contains a summary of the samples.

The gloss values of the sample were measured using a gloss meter (see Figure 3.8).The gloss value is determined in 60° geometry, which is a standard geometry for measuring glossiness. To compare the results, $R(n,\lambda)_{gt}$ are acquired using the same approach and for the same positions (i.e. case1 & case2) under lighting condition H_400Wattx1. In total, ten samples (five gray and five white) are captured for each case.

The radiometric differences are computed using RMSE between $R(n,\lambda)_{hl}$ and $R(n,\lambda)_{gt}$.

6.2.1 Results and discussions

Figure 6.3 illustrates the results. For both cases 1 and 2 (defined in section 5.3), the RMSE values between $R(n,\lambda)_{hl}$ and $R(n,\lambda)_{gt}$ are plotted. Each gray sample is combined with one white reference sample. The RMSE for each gray patch is plotted against each white reference in the Figure. Overall, the samples with a high level of glossiness appear to have good radiometric accuracy with all levels of white reference. However, one important concern is that overall, RMSE in case2 is higher than in case1.

Because the acquisitions are done in such a manner that all samples are acquired first in position 1 (i.e. case1), and then all samples are acquired in position 2. The

Table 6.2: *Description of the NCS samples used in this experimental study. The gray samples are named in such a way that NCS refers to the NCS gloss scale, separated by -, and GV refers to the words "Gloss Value," followed by a number indicating the level of gloss scale. Similarly, white samples are named in such a way that NCS refers to the NCS gloss scale, separated by -, followed by the number indicating the level of gloss scale, separated by -, followed by the letter W, indicating that this sample is used as a white reference.*

S.No		Sample	Description	Measured gloss value (60°)
1.	Gray	NCS-GV2	Full-matt sample	3.1
2.		NCS-GV6	Matt sample	10.0
3.		NCS-GV12	Semi-matt sample	12.0
4.		NCS-GV50	Semi-glossy sample	47.3
5.		NCS-GV95	Full-glossy sample	93.3
1.	White	NCS-2-W	Full-matt sample	3.4
2.		NCS-6-W	Matt sample	6.6
3.		NCS-12-W	Semi-matt sample	12.9
4.		NCS-50-W	Semi-glossy sample	41.4
5.		NCS-95-W	Full-glossy sample	95.3

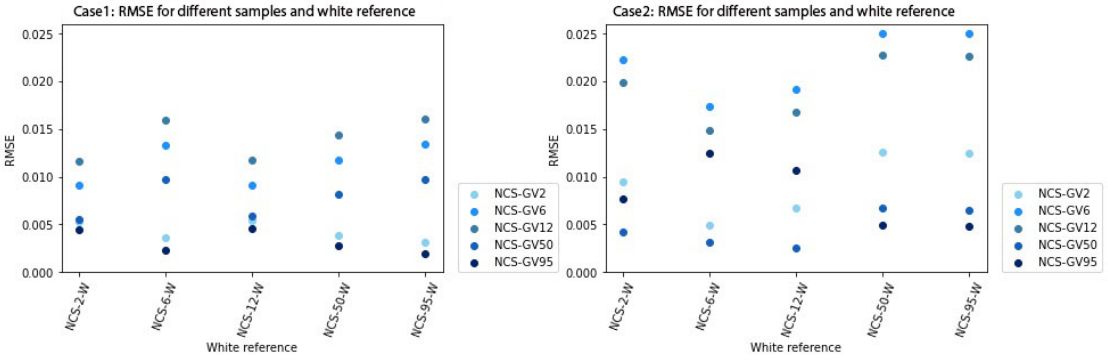

Figure 6.3: *RMSE values recorded for the case1 and case2 of NCS gray samples (denoted with different shades of blue dots) in combination with white reference samples (plotted on x-axis). It can be noticed that the RMSE values are higher in case2 as compare to case1.*

overall illuminance of the scene is most probably shifting, which means that the illuminance of the scene while acquiring data for case1 varies when acquiring data for case2.

To test this, we repeated the experiment (referred as the reproducibility case) under the same illumination condition (H_400wattx1). During this case, data for case2 was acquired first, followed by data for case1. To ensure the stability of the scene, we placed a luxmetre near the sample to monitor the illuminance value in the scene during the acquisitions. The results of the reproducibility case is shown in Figure 6.4.

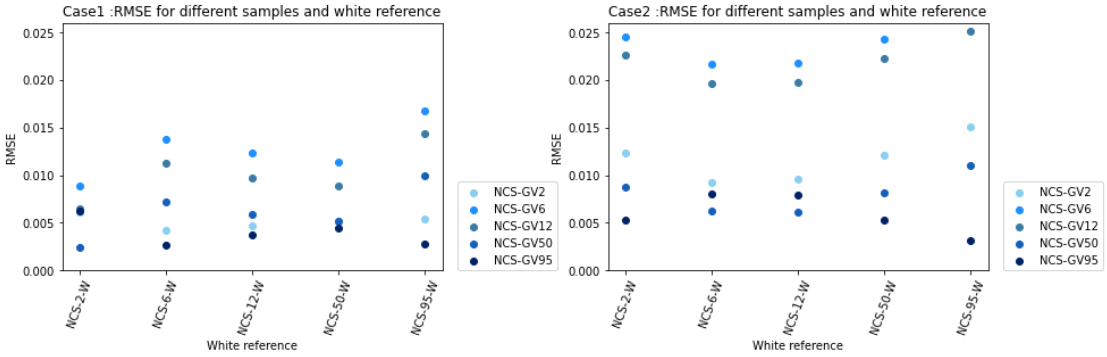

Figure 6.4: *Reproducibility case: RMSE values recorded for the case1 (left) and case2 (right) of NCS gray samples (denoted with different shades of blue dots) in combination with white reference samples (plotted on x-axis). It can be noticed that the RMSE values are higher in case2 as compare to case1.*

When the results of the reproducibility case were compared to the prior case, no substantial inaccuracies were found. However, when the recorded illuminance value is plotted as function of time as shown in Figure 6.5. Figure 6.5 is plotted in such a way that the samples are plotted on the x-axis and they are arranged in the order in which they were measured. It can be seen that when the measurement began for the case1, the illumination value was 779 lux and it varied in between measurements and the last sample were measured when illumination was 787 lux. Similarly, the lux values appear to change throughout measurements in case2.

We did a similar experiment for the same samples in different lighting conditions i.e. H_50Wattx1 and G_315Wattx1, to examine how the other lights behaved and what the radiometric differences were, as well as if the trends observed for samples are also evident in other lighting conditions. It was found that illumination of H_50Wattx1 was stable at 262 lux throughout the acquisition.

From the Figure 6.6, it is seen that the RMSE values for the case1 are lower as compared to case2 for all the three lighting conditions, especially for the matt and semi-matt samples (i.e. NCS-GV6 and NCS-GV12). Because the H_50Wattx1

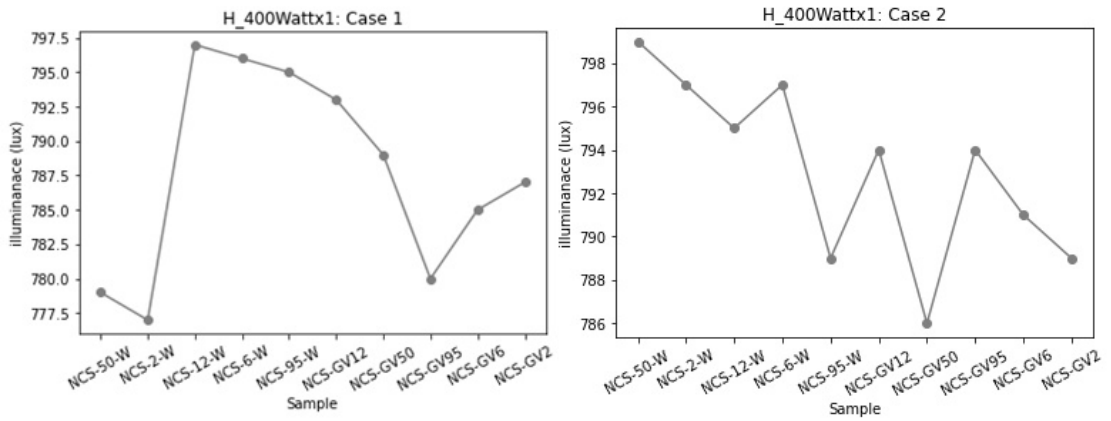

Figure 6.5: *The samples on the x-axis are shown in the order in which they were measured in the graph*

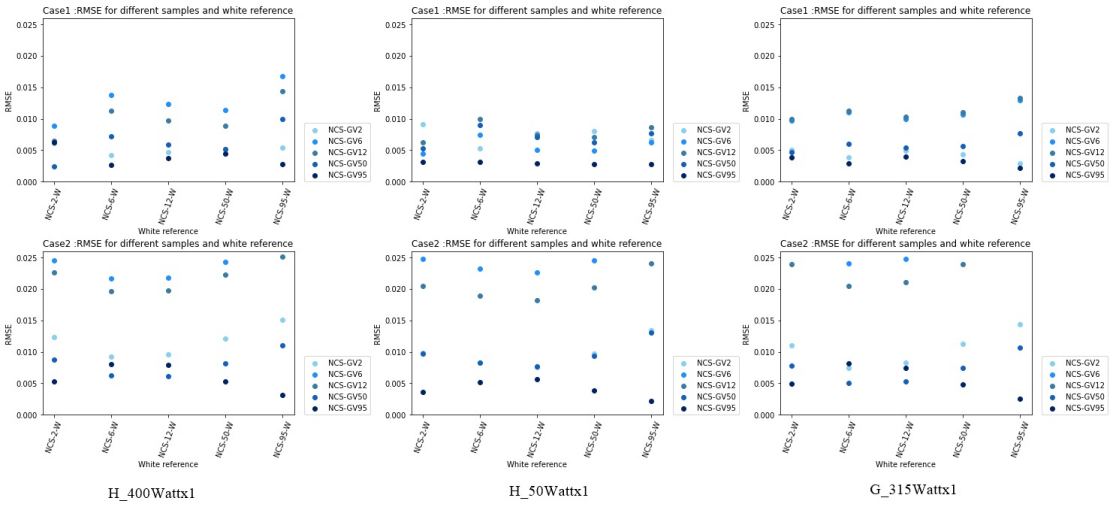

Figure 6.6: *RMSE values recorded for the case1 (displayed in upper row) and case2 (displayed in lower row) of NCS gray samples in combination with white reference samples for H_400Wattx1, H_50Wattx1 and G_315Wattx1.*

has relatively better accuracy in case1, we added another light source to the experimental setup (i.e. 45/0x2) to reduce the errors in case2. For this experimental setup, a similar experiment is done using two light sources from opposite sides (H_50Wattx2). The results are shown in Figure 6.7.

When the radiometric accuracy of the samples is compared with respect to the white reference, it can be seen that the samples that are fully matt and fully glossy, i.e. (approximately 3% and 95% Gloss values, respectively) have the lowest RMSE values in both cases 1 and 2 for all three lighting conditions. This demonstrates

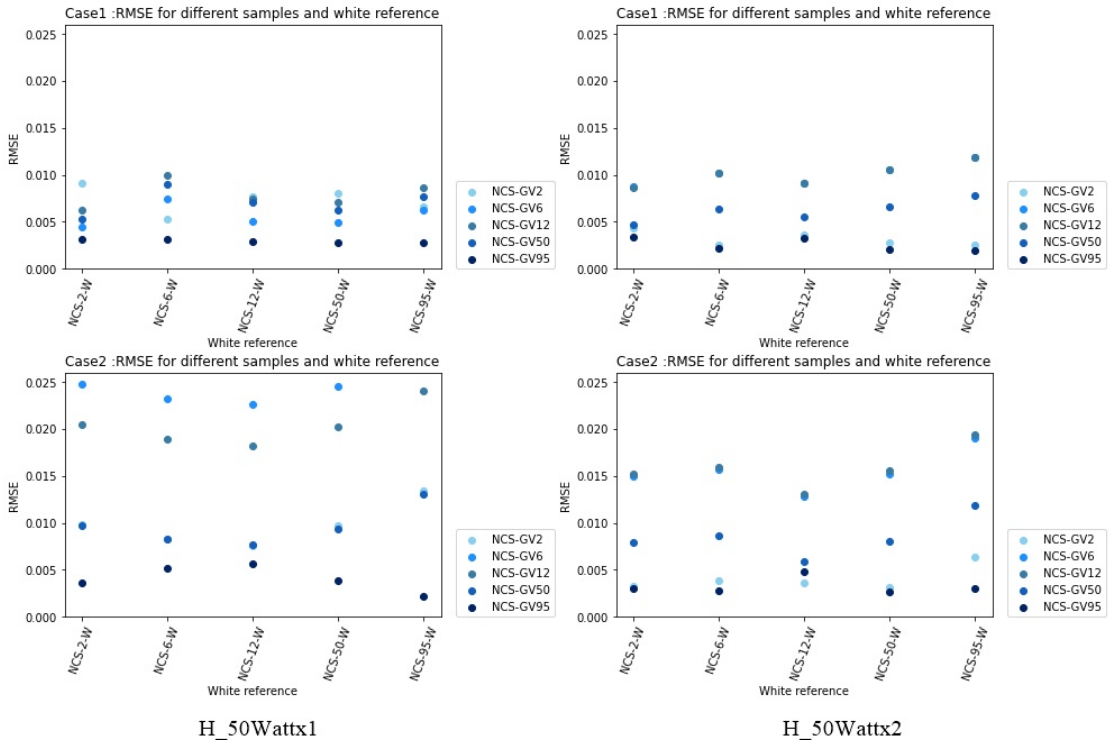

Figure 6.7: *RMSE values recorded for the case1 and case2 of NCS gray samples in combination with white reference samples under H_ 50Wattx1 and H_ 50Wattx2 lighting conditions.*

that the type of white reference used influences the accuracy of the acquired data.

6.3 Proposed pipeline for in-situ measurement conditions

The research study presented in this report is based on many experimental tests that are carried out to characterise each element used in the acquisition setup in order to identify sources of errors and estimate how much those elements can influence the obtained data. We will present the measurement pipeline to be used in the museum and emphasise the importance of each piece based on the findings of each experimental test. In the first experimental study, we investigated the influence of light sources involved in an experiment setup.

In the first experiment, we evaluated the effect of light sources in an experiment setup. Varied results under different lighting conditions have highlighted the significance of the light source based on its SPD and stability. Selecting the

appropriate light source with enough energy in the visible region of the spectrum is essential for getting accurate data from the scene. Among all the lights, we recommend using the halogen light source (H_50Watt) specifically because it is a stable light source, with enough energy in the visible region of EM, It also does not take a long time to stabilise itself, making it a practical option for in-situ acquisitions. MH grow light sources, on the other hand, demonstrated good colorimetric accuracy. They do, however, have a very high illuminance, which is not appreciated in museum conditions. It also has more energy in shorter wavelengths (i.e. UV light), which is harmful to the museum's artworks.

In the second experimental investigation, we looked at the stray light introduced by the surrounding colours and the order of those colours in the scene. It is to quantify the errors that can arise from object to object. The results from the study revealed that the surrounding color has an effect on the accuracy of the color patch.

The third experimental research emphasises the importance of using a reference device to evaluate ground truth data. Since artworks cannot be mounted in a device like HunterLab Ultrascan® PRO, it cannot be utilised to obtain ground truth data. Instead, it is suitable for validating the data obtained with the JETI-specbos 1211 L. The results of this study suggested investigating the accuracy of the same sample being influenced by the position of the same sample in the scene.

The fourth study, which demonstrated the impact of geometry employed in acquisition, emphasises the need of adopting standard geometry rather than arbitrary arrangement of light sources in the acquisition setup. Some of the artworks in the museum do not always have a large room or area surrounding them, which necessitates random lighting configurations; however, all of the discussed considerations must be kept in mind when selecting the arbitrary geometry.

In the fifth experimental study, we showed the significance of white reference since it is shown to influence the acquired data. Additionally, in the study's results section, we addressed which kind of white references perform best with specific types of samples. However, in the museum, the surface material of the paintings changes; some have a matt surface, others have oil paints, and some are varnished, all of which contribute to the change in surface reflection properties.

Because having a distinct type of white reference for each type of painting isn't always practical. As a result, we advise using the white reference NCS-12-W (12% glossy). The reason of that is, as shown in 6.7, NCS-12-W has relatively less RMSE, as compared to other white references i.e. NCS-2-W, NCS-6-W, NCS-50-W and NCS-95-W. Consequently, NCS-12-W works well for all types of samples.

Proposed measurement setup

The measurement setup consists of a test object, 2 halogen light sources, a SpecimIQ spectral camera as a measuring device, JETI-specbos 1211 L spectroradiometer as a ground truth acquisition device, and a big white reference sheet (about 12% glossy). We advice to have the light sources, target (i.e. object to be acquired) and acquisition device at 45°/0° geometry. In our acquisition setup, the test object is positioned in the centre of the scene, 1.09 m above the ground. The data acquisition device and light sources (referred to as H_50Wattx2) are positioned in a 45°/0° geometry, facing the test target and 1.09 m above the ground. They all are spaced 1.2 m apart from one another. (see Figure 6.8), that represents experimental setup)

Results and discussions

To provide the assessment of the new lighting setup, the radiometeric and colorimetric accuracy is calculated between $R(n,\lambda)_{gt}$ and $R(n,\lambda)_{target}$. The results obtained are RMSE of 0.023, the colorimetric accuracy of JND u'v'= 1.706 and ΔE^*ab = 2.871 . The overall distribution of *JNDu'v'* and ΔE^*ab values of individual colour patches are given in Figure 6.9.

The results obtained in the case of H_50Wattx2 are better than the results

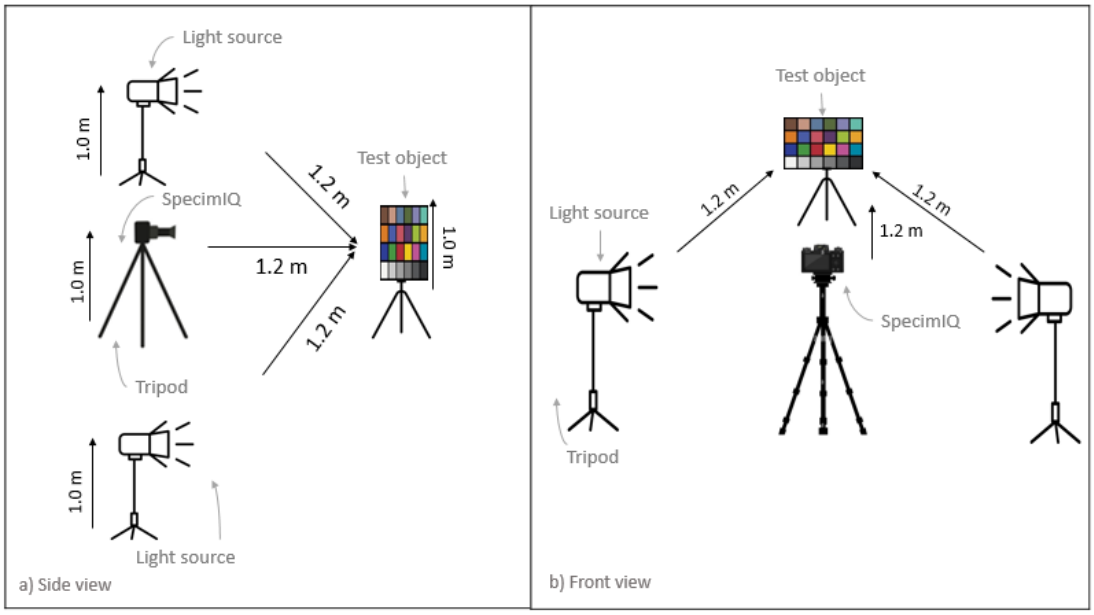

Figure 6.8: *Semantic representation of the acquisition setup with* 45/0°x2 *viewing geometry*

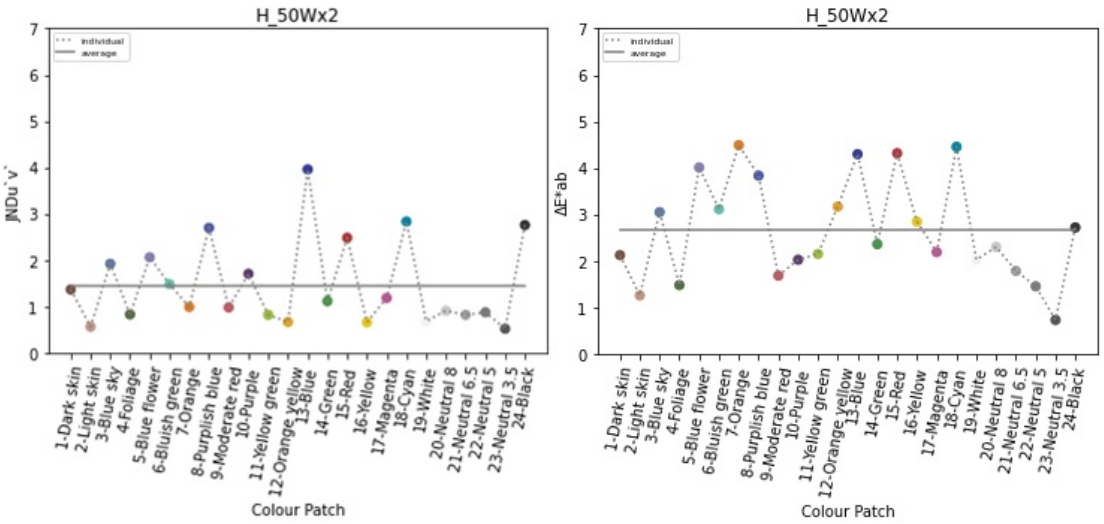

Figure 6.9: *The overall distribution of* JNDu'v' *and* ΔE*ab *values of individual colour patches.*

acquired in the case of H_50Wattx1, in which the maximum *JNDu'v'* and ΔE^*ab value were 4.886 and 7.045 respectively, which has been reduced in the case of H_50Wattx2 (see Figure 6.10). In terms of spectral and colorimetric accuracy, the obtained results are satisfactory, as ΔE^*ab less than 6 is normally considered acceptable.

When these colorimetric data are compared to the other two lighting conditions, G_315Wattx1 and G_560lx1, *JNDu'v'* and ΔE^*ab are significantly lower than the recommended condition, H_50Wattx1. The reason for not recommending those light sources is that their illuminance is very high and they include a lot of UV light (see SPD in Figure 4.6), which is not suited for museum environment because those light sources may cause possible harm to the artworks (see section 1.4).

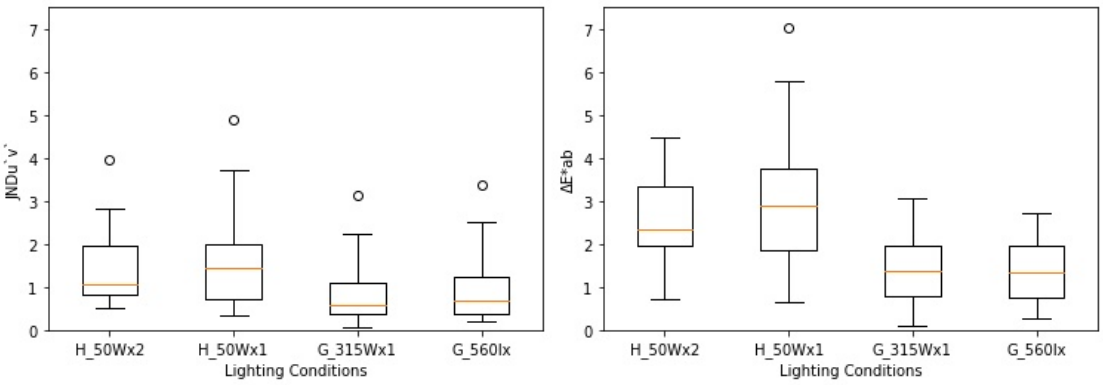

Figure 6.10: *Colorimetric accuracy comparisons among all lighting conditions*

7 | Conclusion and future work

Coloured artwork that is part of our cultural heritage and holds great value must be documented in order to be saved, preserved or to be used for other art-related purposes. One of the important aspects of an artwork is its colour which needs to be documented as accurately as possible. HSI, a non-invasive imaging technique has been utilised in the past to be used in museums to document the artwork. However, no procedures or standards have been established to ensure data reproducibility or accuracy, especially in a museum environment. Given that the artefacts are so delicate and potentially vulnerable to damage in a museum environemnt, there must be some standards that needs to be followed.

This study proposes the measurement pipeline to utilise the hyperspectral camera i.e. SpecimIQ, to capture the spectral reflectance of the entire surface of the painting in a museum to ensure high quality data reproduction in terms of radiometric and colorimetric accuracy.

The quality of data reproduction is determined not only by the acquisition instrument, but also by the acquisition setup and the elements involved. The study is divided into five different experimental setups, each to investigate different aspects of the acquisition setup. The first experimental setup investigated how the light sources used to illuminate the scene can contribute to the possible errors in the data. We explored the possibility of stray light introduced by the device optics and quantified the inaccuracy. We also used HunterLab UltraScan® PRO to characterise the output of our reference device (JETI-specbos 1211 L) in order to determine the likely source of problems. Previous studies have employed a random selection of white reference in hyperspectral imaging acquisitions to estimate the illuminance of the scene; we explored the implications of selecting the proper kind of white reference in the data output, and we also explored the standard acquisition geometry. By studying different scenarios of the data acquisition setup, we quanitified the error introduced by the different factors. Lastly, we used the analysis of those studies to propose guidelines. A standard workflow for hyperspectral reflectance acquisitions in a museum is also provided.

The benefit of the standard workflow is that the researchers will follow a standardised methodology for data acquisition, which assures data reproducibility.

In the future, this research will be used in a real-world museum setting to capture spectral reflectance images from CH artworks. The suggested guidelines and procedure will be utilised to acquire the spectral reflectance of the artwork at the museum, and a database of that spectral reflectance will be created and made publicly available for use in a variety of applications involving artwork.

A | Appendix

Colour calculation with LuxPy

using the u'v' Chromaticity diagram and CIELAB Colour space using the CIE illuminants E and D65 and the 2° CIE 1931 standard observer as follows:

$$xyz, xyz\_w = lx.spd\_to\_xyz(spd, rfl = R(\lambda), cieobs = cieobs, out = 2)$$

Where (SPD = $D65$ & $Illuminant\ E$, rfl = spectral reflectance, cieobs = '1931_2',
lx = Luxpy library (see section 3.6)) xyz are tristimulus values and xyz_w is the white point of the illuminant. Converting from xyz to Yuv and Lab is done as follows:

$$Yuv = lx.xyz\_to\_Yuv(xyz)$$
$$Lab = lx.xyz\_to\_lab(xyz, xyzw = xyz\_w)$$

Colour difference between the two $R(n,\lambda)_{gt}$ and $R(n,\lambda)_{target}$ (i.e. Yuv_{gt} & Yuv_{target} and Lab_{gt} & Lab_{target}) is measured as the Euclidean distance between them. They are computed as follows.

$$\Delta Euv = (((Yuv_{gt} - Yuv_{target})[..., 1:]^2).sum(axis = -1)^{0.5}).T$$
$$1unitofJNDu'v' = \Delta Euv/0.0033$$

Yuv_{gt} = CIE 1976 u'v' chromaticity values of $R(n,\lambda)_{gt}$ and Yuv_{target} = CIE 1976 u'v' chromaticity values of $R(n,\lambda)_{target}$.

$$\Delta E*ab = (((Lab_{gt} - Lab_{target})[..., 1:] * *2).sum(axis = -1) * *0.5).T$$

where, Lab_{gt} = CIELAB values of $R(n,\lambda)_{gt}$. Lab_{gt} = CIELAB values of $R(n,\lambda)_{target}$

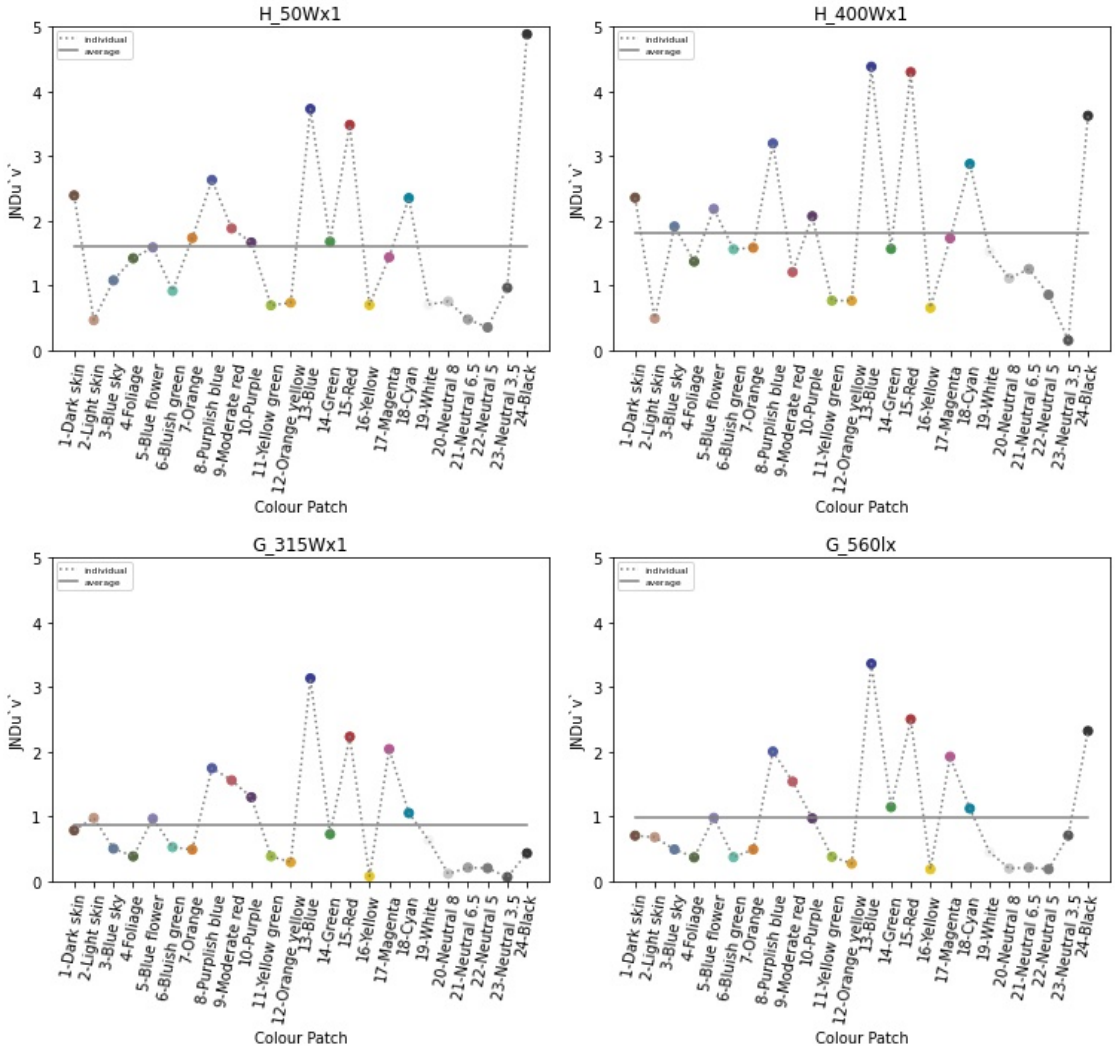

Figure A.1: *Shows the ΔE^*ab and for all colour patches under illuminant E*

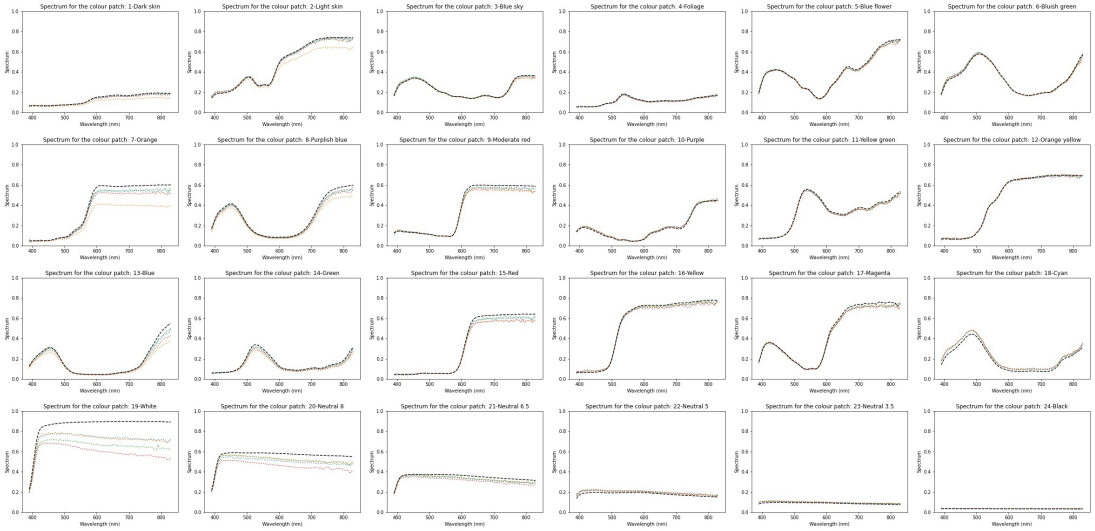

Figure A.2: *The $R(n,\lambda)_{gt}$ acquired for four different lighting conditions and hunterlab data*

Bibliography

[1] https://www.xrite.com/fr-fr/categories/calibration-profiling/colorchecker-classic. (cited on pages 17 and 18)

[2] https://www.bulbs.com/learning/halogen.aspx, Nov 2005. (cited on page 34)

[3] https://en.wikipedia.org/wiki/colorchecker, Jun 2022. (cited on pages 17 and 19)

[4] https://en.wikipedia.org/wiki/electromagnetic_spectrum, Jun 2022. (cited on page 1)

[5] Stable light sources for test and measurement applications, Feb 2022. (cited on page 45)

[6] Ali A Al-Zuk, Salema S Salman, and Ban Sabah. Enhancement for image capture under non–homogenous lightness using retinex techniques. *Al-Nahrain Journal of Science*, 16(1):102–111, 2013. (cited on page 3)

[7] Mauro Bacci and Marcello Picollo. Non-destructive spectroscopic detection of cobalt (ii) in paintings and glass. *Studies in Conservation*, 41(3):136–144, 1996. (cited on pages 4 and 6)

[8] David Warren Ball. *Field guide to spectroscopy*, volume 8. Spie Press Bellingham, Washington, 2006. (cited on page 1)

[9] Rupak Raj Baniya et al. Study of various metrics evaluating color quality of light sources. Master's thesis, 2012. (cited on pages 41 and 42)

[10] Jan Behmann, Kelvin Acebron, Dzhaner Emin, Simon Bennertz, Shizue Matsubara, Stefan Thomas, David Bohnenkamp, Matheus T Kuska, Jouni Jussila, Harri Salo, et al. Specim iq: evaluation of a new, miniaturized handheld hyperspectral camera and its application for plant phenotyping and disease detection. *Sensors*, 18(2):441, 2018. (cited on pages 2, 18, 19, 20, 21, 22, and 23)

[11] Roy S Berns. The science of digitizing paintings for color-accurate image archives: A review. *Journal of imaging science and technology*, 45(4):305–325, 2001. (cited on page 18)

[12] Burak Bitlis, Peter A Jansson, and Jan P Allebach. Parametric point spread function modeling and reduction of stray light effects in digital still cameras. In *Computational Imaging V*, volume 6498, pages 253–260. SPIE, 2007. (cited on page 56)

[13] Andrea Casini, Franco Lotti, Marcello Picollo, Lorenzo Stefani, and Alfredo Aldrovandi. 38 fourier transform interferometric imaging spectrometry: a new tool for the study of reflectance and fluorescence of polychrome surfaces. In *Conservation Science 2002: Papers from the Conference Held in Edinburgh, Scotland, 22-24 May 2002*, page 249. Archetype Publications, 2003. (cited on page 4)

[14] Lionel Clermont, Wilfried Uhring, and Marc Georges. Stray light characterization with ultrafast time-of-flight imaging. *Scientific reports*, 11(1):1–9, 2021. (cited on page 56)

[15] Costanza Cucci, Andrea Casini, Marcello Picollo, Marco Poggesi, and Lorenzo Stefani. A hyper-spectral scanner for high quality image spectroscopy: Digital documentation and spectroscopic characterization of polychrome surfaces. In *ART11-10th International Conference on Non-destructive Investigations and Microanalysis for the Diagnostics and Conservation of Cultural and Environmental Heritage*, 2011. (cited on page 2)

[16] Costanza Cucci, John K Delaney, and Marcello Picollo. Reflectance hyperspectral imaging for investigation of works of art: old master paintings and illuminated manuscripts. *Accounts of chemical research*, 49(10):2070–2079, 2016. (cited on pages 4 and 6)

[17] John K Delaney, Paola Ricciardi, Lisha Deming Glinsman, Michelle Facini, Mathieu Thoury, Michael Palmer, and E René de la Rie. Use of imaging spectroscopy, fiber optic reflectance spectroscopy, and x-ray fluorescence to map and identify pigments in illuminated manuscripts. *Studies in Conservation*, 59(2):91–101, 2014. (cited on page 6)

[18] Yanni Dong, Bo Du, Liangpei Zhang, and Xiangyun Hu. Hyperspectral target detection via adaptive information—theoretic metric learning with local constraints. *Remote sensing*, 10(9):1415, 2018. (cited on pages 5 and 6)

[19] Xinyu Dou, Chenyu Li, Qian Shi, and Mengxi Liu. Super-resolution for hyperspectral remote sensing images based on the 3d attention-srgan network. *Remote Sensing*, 12(7):1204, 2020. (cited on pages 5 and 6)

[20] Gerda J Edelman, Edurne Gaston, Ton G Van Leeuwen, PJ Cullen, and Maurice CG Aalders. Hyperspectral imaging for non-contact analysis of forensic traces. *Forensic science international*, 223(1-3):28–39, 2012. (cited on pages 5 and 6)

[21] Gamal ElMasry, Douglas F Barbin, Da-Wen Sun, and Paul Allen. Meat quality evaluation by hyperspectral imaging technique: an overview. *Critical reviews in food science and nutrition*, 52(8):689–711, 2012. (cited on page 2)

[22] Robert Ennis, Florian Schiller, Matteo Toscani, and Karl R Gegenfurtner. Hyperspectral database of fruits and vegetables. *JOSA A*, 35(4):B256–B266, 2018. (cited on page 7)

[23] David H Foster, Kinjiro Amano, Sérgio MC Nascimento, and Michael J Foster. Frequency of metamerism in natural scenes. *Josa a*, 23(10):2359–2372, 2006. (cited on page 4)

[24] Daniel Garside, Katherine Curran, Capucine Korenberg, Lindsay MacDonald, Kees Teunissen, and Stuart Robson. How is museum lighting selected? an insight into current practice in uk museums. *Journal of the Institute of Conservation*, 40(1):3–14, 2017. (cited on pages 9 and 10)

[25] Andreas Georgopoulos and Elisavet Konstantina Stathopoulou. Data acquisition for 3d geometric recording: state of the art and recent innovations. *Heritage and archaeology in the digital age*, pages 1–26, 2017. (cited on page 11)

[26] A Giannini and L Mercatelli. Colorimetric quantities and laws. In *Sustainable Indoor Lighting*, pages 23–37. Springer, 2015. (cited on page 3)

[27] Megandhren Govender, Kershani Chetty, and Hartley Bulcock. A review of hyperspectral remote sensing and its application in vegetation and water resource studies. *Water Sa*, 33(2):145–151, 2007. (cited on page 5)

[28] Nathan A Hagen, Liang S Gao, Tomasz S Tkaczyk, and Robert T Kester. Snapshot advantage: a review of the light collection improvement for parallel high-dimensional measurement systems. *Optical Engineering*, 51(11):111702, 2012. (cited on page 5)

[29] Hideaki Haneishi, Takayuki Hasegawa, Asako Hosoi, Yasuaki Yokoyama, Norimichi Tsumura, and Yoichi Miyake. System design for accurately estimating the

spectral reflectance of art paintings. *Applied Optics*, 39(35):6621–6632, 2000. (cited on page 7)

[30] Bruce Hapke. *Theory of reflectance and emittance spectroscopy*. Cambridge university press, 2012. (cited on pages 5, 6, and 7)

[31] Steven Hordley, Graham Finalyson, and Peter Morovic. A multi-spectral image database and its application to image rendering across illumination. In *Third International Conference on Image and Graphics (ICIG'04)*, pages 394–397. IEEE, 2004. (cited on page 54)

[32] HunterLab Inc. Specifications ultrascan product specification - hunterlab, 2022. (cited on page 28)

[33] Rhopoint Instruments. Rhopoint iq 20/60/85 gloss haze doi meter, May 2022. (cited on pages 28 and 29)

[34] Specim IQ. https://www.specim.fi/iq/, Jun 2021. (cited on pages 17, 18, and 21)

[35] Spectral signature NA ITProSpt. Based on the following spectral signature., which color vegetation, water and bare soil will be seen..., Oct 2021. (cited on page 1)

[36] Peter A Jansson and Robert P Breault. Correcting color-measurement error caused by stray light in image scanners. In *Color and Imaging Conference*, volume 1998, pages 69–73. Society for Imaging Science and Technology, 1998. (cited on pages 56 and 57)

[37] Marvin E Klein, Bernard J Aalderink, Roberto Padoan, Gerrit De Bruin, and Ted AG Steemers. Quantitative hyperspectral reflectance imaging. *Sensors*, 8(9):5576–5618, 2008. (cited on page 1)

[38] FA Kruse. Identification and mapping of minerals in drill core using hyperspectral image analysis of infrared reflectance spectra. *International journal of remote sensing*, 17(9):1623–1632, 1996. (cited on pages 5 and 6)

[39] Xiaona Li, Ruolan Li, Mengyu Wang, Yaru Liu, Baohua Zhang, and Jun Zhou. Hyperspectral imaging and their applications in the nondestructive quality assessment of fruits and vegetables. *Hyperspectral imaging in agriculture, food and environment*, pages 27–63, 2017. (cited on page 31)

[40] Haida Liang. Advances in multispectral and hyperspectral imaging for archaeology and art conservation. *Applied Physics A*, 106(2):309–323, 2012. (cited on page 34)

[41] Python library. Welcome to python.org, 2022. (cited on pages 17 and 28)

[42] Guolan Lu and Baowei Fei. Medical hyperspectral imaging: a review. *Journal of biomedical optics*, 19(1):010901, 2014. (cited on pages 5 and 6)

[43] Lindsay W MacDonald, Tatiana Vitorino, Marcello Picollo, Ruven Pillay, Michał Obarzanowski, Joanna Sobczyk, Sérgio Nascimento, and João Linhares. Assessment of multispectral and hyperspectral imaging systems for digitisation of a russian icon. *Heritage Science*, 5(1):1–16, 2017. (cited on pages 7 and 11)

[44] Miguel Á Martínez, Eva M Valero, Juan L Nieves, Rosario Blanc, Eloísa Manzano, and José L Vílchez. Multifocus hdr vis/nir hyperspectral imaging and its application to works of art. *Optics Express*, 27(8):11323–11338, 2019. (cited on pages 7, 9, 10, and 13)

[45] Miguel Ángel Martínez-Domingo, Manuel Melgosa, Katsunori Okajima, Víctor Jesús Medina, and Francisco José Collado-Montero. Spectral image processing for museum lighting using cie led illuminants. *Sensors*, 19(24):5400, 2019. (cited on pages 6, 7, and 13)

[46] William Ross McCluney. *Introduction to radiometry and photometry*. Artech House, 2014. (cited on page 3)

[47] Gary W Meyer. Wavelength selection for synthetic image generation. *Computer Vision, Graphics, and Image Processing*, 41(1):57–79, 1988. (cited on page 54)

[48] Cristina Montagner, João MM Linhares, Márcia Vilarigues, Maria João Melo, and Sérgio MC Nascimento. Supporting history of art with colorimetry: The paintings of amadeo de souza-cardoso. *Color Research & Application*, 43(3):304–310, 2018. (cited on page 4)

[49] Arman Nihal. Improvement of photogrammetry by hyperspectral imaging. Master's thesis, Itä-Suomen yliopisto, 2020. (cited on page 24)

[50] Y Ohno and P Blattner. Chromaticity difference specification for light sources. *Int. Commission Illumination, Vienna, Austria, Tech. Rep. CIE TN*, 1:2014, 2014. (cited on page 42)

[51] Henryk Palus and Damian Bereska. Colour reproduction accuracy of vision systems. In *Computer Vision and Graphics*, pages 279–286. Springer, 2006. (cited on page 17)

[52] Antonio Perri, Bárbara E Nogueira de Faria, Danielle C Teles Ferreira, Daniela Comelli, Gianluca Valentini, Dario Polli, Giulio N Cerullo, and Cristian Manzoni. A hyperspectral camera for conservation science, based on a birefringent

ultrastable common path interferometer. In *Optics for Arts, Architecture, and Archaeology VII*, volume 11058, pages 14–23. SPIE, 2019. (cited on page 4)

[53] Marcello Picollo, Costanza Cucci, Andrea Casini, and Lorenzo Stefani. Hyperspectral imaging technique in the cultural heritage field: New possible scenarios. *Sensors*, 20(10):2843, 2020. (cited on pages 4, 7, and 14)

[54] Spectroradiometer JETI product specifications, 2005. (cited on pages 24 and 25)

[55] Ultrascan Pro product specifications. Hunterlab ultrascan®, 2022. (cited on pages 17 and 26)

[56] Standard and Quantities. Nist special publications, May 2006. (cited on page 1)

[57] Mark S Rea and Andrew Bierman. Comparison of a solid-state luminaire to tungsten-halogen lamps for displaying museum objects. *Journal of the American Institute for Conservation*, 53(1):33–43, 2014. (cited on pages 34 and 36)

[58] NCS gloss sample. Ncs gloss scale, Jun 2022. (cited on page 72)

[59] Jakub Sandak, Anna Sandak, Lea Legan, Klara Retko, Maša Kavčič, Janez Kosel, Faksawat Poohphajai, Rene Herrera Diaz, Veerapandian Ponnuchamy, Nežka Sajinčič, et al. Nondestructive evaluation of heritage object coatings with four hyperspectral imaging systems. *Coatings*, 11(2):244, 2021. (cited on page 7)

[60] David Saunders. High-quality imaging at the national gallery: Origins, implementation and applications. *Computers and the Humanities*, 31(3):153–167, 1997. (cited on page 12)

[61] Jim Schwiegerling et al. Field guide to visual and ophthalmic optics. Spie Bellingham, WA, USA, 2004. (cited on page 42)

[62] John Seymour. Color inconstancy in cielab: A red herring? *Color Research & Application*, 2022. (cited on page 42)

[63] spectral spectral signatures signatures. Esa - eduspace en - home - spectral signatures, Nov 2009. (cited on page 1)

[64] Kevin AG Smet. Tutorial: The luxpy python toolbox for lighting and color science. *Leukos*, 16(3):179–201, 2020. (cited on pages 17 and 29)

[65] JETI specbos1211 2. Home, 2022. (cited on page 17)

[66] Specim IQ user manual Spectral Imaging Ltd. https://www.specim.fi/downloads/iq/manual/software/iq/topics/iq-smart-camera-user-manual.html, Feb 2008. (cited on pages 21, 23, and 24)

[67] Spectroradiometer. specbos1211-l, 2005. (cited on pages 25, 26, and 99)

[68] electromagnetic spectrum. Components of electromagnetic spectrum, Dec 2019. (cited on page 2)

[69] David L Spooner. New method for determining lateral diffusion error in color measurements. In *Color Imaging: Device-Independent Color, Color Hard Copy, and Graphic Arts*, volume 2658, pages 151–160. SPIE, 1996. (cited on page 69)

[70] K. Tempfli, N. Kerle, and C. Huurneman. Principles of remote sensing, 2009. (cited on page 3)

[71] Garry Thomson. *The museum environment*. Routledge, 2018. (cited on page 10)

[72] Shoji Tominaga, Norihiro Tanaka, and Toshinori Matsumoto. Recording and rendering for art paintings based on multiband data. In *Color Imaging: Device-Independent Color, Color Hardcopy, and Applications VII*, volume 4663, pages 27–34. SPIE, 2001. (cited on pages 13, 37, and 38)

[73] Alessandro Vichi, Chris Louca, Gabriele Corciolani, and Marco Ferrari. Color related to ceramic and zirconia restorations: a review. *Dental materials*, 27(1):97–108, 2011. (cited on page 26)

[74] Tatiana Vitorino, Andrea Casini, Costanza Cucci, Ana Gebejesje, Jouni Hiltunen, Markku Hauta-Kasari, Marcello Picollo, and Lorenzo Stefani. Accuracy in colour reproduction: using a colorchecker chart to assess the usefulness and comparability of data acquired with two hyper-spectral systems. In *International Workshop on Computational Color Imaging*, pages 225–235. Springer, 2015. (cited on pages 7, 14, 18, 31, and 54)

[75] Chunying Wang, Baohua Liu, Lipeng Liu, Yanjun Zhu, Jialin Hou, Ping Liu, and Xiang Li. A review of deep learning used in the hyperspectral image analysis for agriculture. *Artificial Intelligence Review*, 54(7):5205–5253, 2021. (cited on page 5)

[76] Zhijun Wang, Sara Wilhelmina Erasmus, Xiaotong Liu, and Saskia M Van Ruth. Study on the relations between hyperspectral images of bananas (musa spp.) from different countries, their compositional traits and growing conditions. *Sensors*, 20(20):5793, 2020. (cited on page 2)

[77] Carl Fridolin Weber, Dieter Spiehl, and Edgar Dörsam. Comparing gloss meters for gloss measurements on metallic embellishments from the printing industry. In *Advances in Printing and Media Technology: Proceedings of the 47th International Research Conference of iarigai. Athens, Greece*, pages 19–23, 2021. (cited on page 28)

[78] Yue Wu, Toshiyuki Tanaka, and Makio Akimoto. Utilization of individual typology angle (ita) and hue angle in the measurement of skin color on images. *bioimages*, 28:1–8, 2020. (cited on page 42)

[79] Charles A Wüthrich. Fundamentals of imaging colour spaces - uni-weimar.de, May 2008. (cited on page 42)

[80] Fuguo Xing, Haibo Yao, Yang Liu, Xiaofeng Dai, Robert L Brown, and Deepak Bhatnagar. Recent developments and applications of hyperspectral imaging for rapid detection of mycotoxins and mycotoxigenic fungi in food products. *Critical reviews in food science and nutrition*, 59(1):173–180, 2019. (cited on page 31)

[81] Ali Zahavi, Andrei Palshin, Dhanushka Chamara Liyanage, and Mart Tamre. Influence of illumination sources on hyperspectral imaging. In *2019 20th International Conference on Research and Education in Mechatronics (REM)*, pages 1–5. IEEE, 2019. (cited on page 34)

[82] Yonghui Zhao. *Image segmentation and pigment mapping of cultural heritage based on spectral imaging*. Rochester Institute of Technology, 2008. (cited on pages 7 and 14)

List of Figures

LIST OF FIGURES

List of Tables